The Effects of Isothermal Aging on the Mechanical Behavior of Underfill Encapsulants

by

Chang Lin

A dissertation submitted to the Graduate Faculty of
Auburn University
in partial fulfillment of the
requirements for the Degree of
Doctor of Philosophy

Auburn, Alabama
August 9, 2010

Keywords: Underfill, Encapsulant, Aging, Evolution
Material Behavior, Creep

Approved by

Jeffrey C. Suhling, Chair, Quina Distinguished Professor, Mechanic Department
Pradeep Lall, Thomas Walter Professor, Mechanic Department
Roy Knight, Assistant Professor, Mechanic Department
Ruel A. Overfelt, Professor, Materials Department

Abstract

Underfill encapsulants are widely used in the microelectronics industry to improve the reliability of electronic components assembled to printed circuit boards. In this work, the effects of isothermal aging on the stress-strain and creep behaviors of underfills have been experimentally characterized. A novel method has been developed to fabricate underfill uniaxial test specimens so that they accurately reflect the encapsulant layer present in flip chip assemblies. Samples were subjected to various aging temperatures and aging times before testing. The measured experimental data demonstrated that large changes (up to 100X) occur in the mechanical properties of the underfill. Empirical and constitutive models have also been developed that describe the aging effects on the mechanical properties of the material.

Furthermore, the effects of underfill cure temperature and JEDEC MSL preconditioning on underfill mechanical and strength properties, as well as flip chip assembly reliability, have been explored. The failure mechanisms in the flip chip assemblies were studied using CSAM, X-ray and SEM analysis. The results clearly indicate the advantages of the higher curing temperature. These included improved mechanical properties, superior thermal cycling fatigue life, and enhanced resistance to detrimental effects from moisture exposure and solder reflow.

Acknowledgments

I would like to express my sincere gratitude to my advisor Dr. Jeffrey C. Suhling for his support and guidance support throughout the course of this research. Sincere gratitude and appreciation are also extended to Dr. Ruel A. Overfelt, Dr. Pradeep Lall and Dr. Roy Knight for serving on my Ph.D. committee as well as providing precious time, valuable instruction and recommendations.

I would like to thank John Marcell for his kindness and help in maintaining all equipment. Special thanks are also extended to all my coworkers and friends, Kaysar Rahim, Jordan Roberts, Hongtao Ma, Yifei Zhang, and Zijie Cai for their encouragement and help.

Finally, I would like to thank my family for their continuous support and encouragement during this time. All of this would be impossible without their understanding and support.

Table of Contents

List of Tables

List of Figures

CHAPTER 1

INTRODUCTION

Electronic packaging technology is the science of establishing interconnections between various levels of electronic devices, components, modules, and system. It dictates the cost, performance and reliability of almost all future commercial and military electronics equipment. The most compact and high density electronic packaging is flip chip technology. Most flip chip assemblies require underfill to improve their reliability to acceptable levels. Otherwise, the small solder joints are subjected to high shear strains due to the thermo-mechanical mismatch between die and substrate. Continuous improvement of packaging and related technologies has provided the impetus for the development of new and improved consumer electronic products.

1.1 Electronic Packaging Technology

Electronic packaging refers to the placement and connection of many electronic and electromechanical components in an enclosure that protects the system from the environment and provides easy access for routine maintenance. The four major functions of an electronic package include signal distribution, power distribution, heat dissipation, and protection of the components and interconnections.

Generally the packaging system can be divided into several interconnect levels. At the first level, the integrated circuit (IC) chip and a substrate or chip carried are connected by one of three methods: wirebonding, tape-automated bonding (TAB), or flip chip technology. At the

second level, the substrate or chip carried is connected to a printed wiring board (PWB). This attachment can be achieved by using plated through hole (PTH) technology or surface mount technology (SMT). At the third level, the PWB is connected to a motherboard. Figure 1.1 illustrates a typical configuration for electronic packaging technology.

1.2 Flip Chip Technology

The goals of electronic packaging engineers are to lower costs, increase packaging density, and improve performance with better circuit reliability. Flip chip technology was introduced by IBM for mainframe computer applications in the early 1960s. Since then, millions of flip chips have been processed by IBM on ceramic substrates, and they claim a reliability test record of 60,000 thermal cycles [1]. Presently, the automotive, computer, and cell phone industries all rely on flip chip technology for their success. A typical flip chip on laminate assembly is shown in Figure 1.2. Flip chip is also gaining popularity in ball grid array (BGA) and other chip carrier technologies, replacing wirebonding.

In flip chip assemblies, the semiconductor chip faces down onto a substrate. Small solder joints are used to both electrically and mechanically connect the silicon chip to the substrate using a high temperature reflow process. Flip chip technology provides the ultimate in size and weight saving, since no extra area is needed to make contacts of components to the substrate. This is extremely important for electronics manufacturers due to increasing demands for miniaturized products and assemblies. In addition, the relatively short electrical connection paths provide faster signal transmissions. Finally, it is possible to have more input/output (I/O) connections for a given chip size. All of these improvements yield superior performance over other interconnection methods.

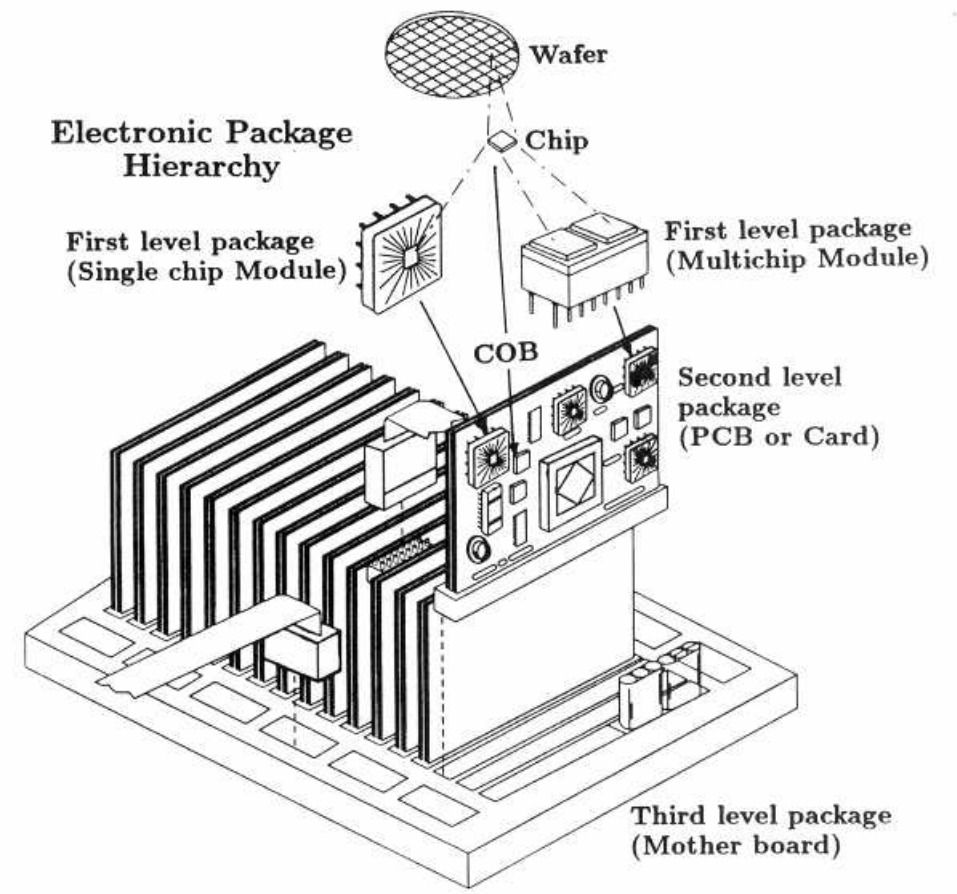

Figure 1.1 - Typical Electronic Packaging Configuration

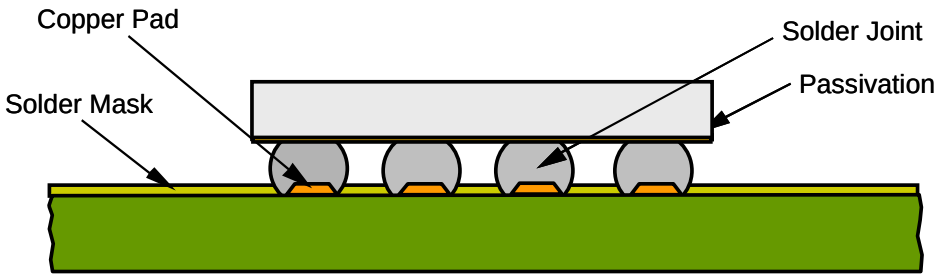

Figure 1.2 - Schematic of a Flip Chip Assembly

In flip chip technology, there is only one level of connection between the chip and the circuit board. Flip chips therefore have an advantage over wirebonding because all connections are formed simultaneously, whereas with wirebonding, the connections are made one at a time. However, in practice the cost of die bumping can be high. Thus, in low volumes, wirebonding can still be more cost effective.

1.3 Solder Bump Connections

As discussed above, the silicon die in flip chip technology are connected to the substrate by small solder joints. Eutectic or near eutectic tin/lead (Sn-Pb) solder has been widely used in the electronics industry due to its outstanding solderability and reliability. Due to harmful effects on the environmental and health concerns, recent legislation has been enacted to require the removal of lead from electronics. Several new lead free solders have been developed as alternatives to Sn-Pb solder, such as Sn-Ag-Cu (SAC) alloys [2]. Flip chip solder joints melt completely during the reflow process, but the surface tension in the molten solder supports the chip so that the extent of the joint collapse is controlled by the wettable area of the pads. A solder joint based flip chip interconnection is also referred to as a controlled collapse chip connection (C4). Solder bumps in flip chip assemblies serve as the structural links, electrical connections, and heat dissipation paths between the chip and the substrate. Thus, failure of any of the solder joints will typically result in failure of the entire product.

Among the failure modes present in flip chip assemblies, the major concern is typically the thermal-mechanical fatigue life of the solder joints. Table 1.1 shows the material properties of the constituents generally used in flip chip packages. During thermal cycling, large shear strains are developed in the solder joints due to the large coefficient of thermal expansion (CTE) mismatch between the silicon die and the substrate, as illustrated in Figure 1.3. Consequently,

Materials	E (GPa)	CTE (ppm/ ^{o}C)	Application
Silicon	131	2.3	Chip or Substrate
Silicon Dioxide	70	0.5	Underfill Fillers
Epoxy	8-12	25-30	Underfill Polymer
Solder	10	15-20	Interconnects
Copper	128	17	Interconnects
Alumina	255	4-6	Ceramic Substrate
FR-4 PCB	22	15-20	Organic Substrate

Table 1.1 - Properties of Materials Used in Flip Chip Packaging

fatigue cracks often initiate at the edges of the joints and then propagate through the interior, resulting in bump failure. The likelihood of solder bump thermal fatigue failure is related to the chosen solder material, substrate and chip metallization, and the development of intermetallic compounds [3].

An analytical estimate of the solder joint shear strain (γ) can be found by using the distance to neutral point approximation (DNP):

$$\Delta\gamma = \frac{(\alpha_{pcb} - \alpha_{sc})\Delta T}{h}[D.N.P] \tag{1.1}$$

where α_{pcb} and α_{sc} are the coefficients of thermal expansion of the PCB and silicon chip, respectively, h is the height of the solder ball joints, ΔT is the temperature change, and D.N.P is the distance to the neutral point. The solder joint fatigue life can be estimated by applying failure criteria such as the Coffin-Manson Equation. For example, for SnPb eutectic solder joints the expression is:

$$N_f = 1.29(\Delta\gamma)^{-1.96} \tag{1.2}$$

where N_f is the estimated number of thermal cycles at which the solder joint will fail and $\Delta\gamma$ is the shear strain change during one cycle. From these equations, it can be clearly seen that the solder joint fatigue life can be increased by using a smaller die, increasing the height of the solder ball joints, reducing the temperature change, and minimizing the CTE mismatch between the die and the substrate.

For most flip chip configurations of interest, the thermal fatigue life is unacceptable and early joint failure occurs. Thus, it is necessary to add an underfill encapsulant between the chip and substrate to assist the solder joints in maintaining the mechanical integrity of the assembly.

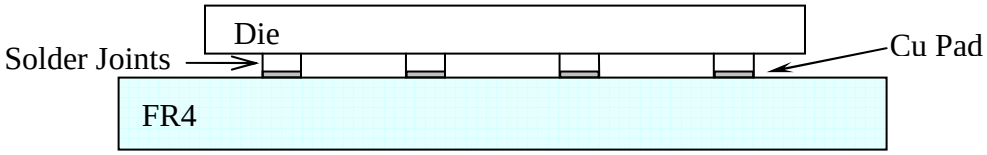

(a) At Room Temperature

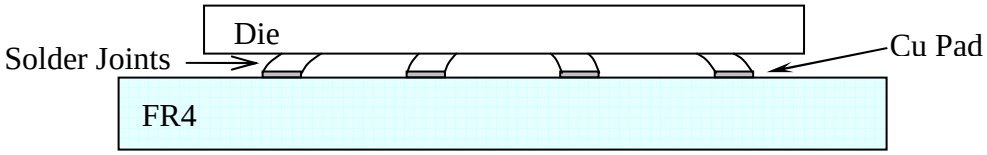

(b) Heating

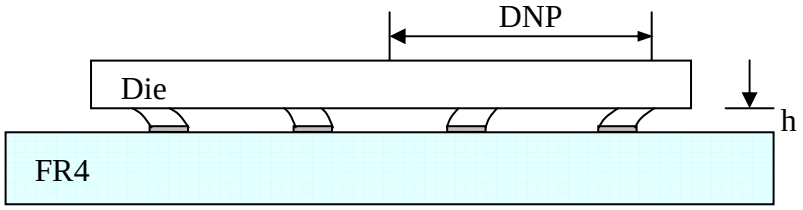

(c) Cooling

Figure 1.3 - Solder Joint Fatigue During Thermal Cycling

1.4 Underfill Technology

Underfill is required by most flip chips to avoid rapid solder joint fatigue failures. Since its first use by IBM in the 1970s, underfill systems have been widely adopted by industry following the movement from ceramic substrates to organic substrates, which are the ultimate goal for flip chip technology [4]. Flip chips with organic substrates are often referred to as second generation flip chip technology.

Underfill encapsulants are either thermosetting or thermoplastic polymers, both of which are widely used in industry. Figure 1.4 shows the volume distribution for use of thermoplastic polymers in the United States in 2001, and the electronic packaging market was the largest [5].

To solve the CTE mismatch problem, an underfill material is used to fill the gap between the integrated circuit die and the substrate in a flip chip package to improve the solder joint fatigue life [6, 7]. Underfill not only connects the chip and the substrate but also provides an additional thermal path from the chip to the substrate. The introduction of underfill gives the solder interconnections more mechanical robustness, and a significant increase in solder fatigue resistance results [8]. Moreover, underfill promotes evenly distributed and reduced solder joint strains during temperature changes, thus improving solder joint fatigue life, often by factor of 10 or more [8]. The underfill encapsulant also protects the chip from moisture, radiation, and other hostile operating environments such as mechanical shock and vibration.

The mechanical properties of underfill materials have a great influence on the reliability of flip chip packages. For example, Figure 1.5 illustrates finite element prediction of the solder joint strains in a flip chip assembly subjected to a temperature change from -40 to 125 °C. The strain levels are much smaller when using an underfill with low CTE and high elastic modulus.

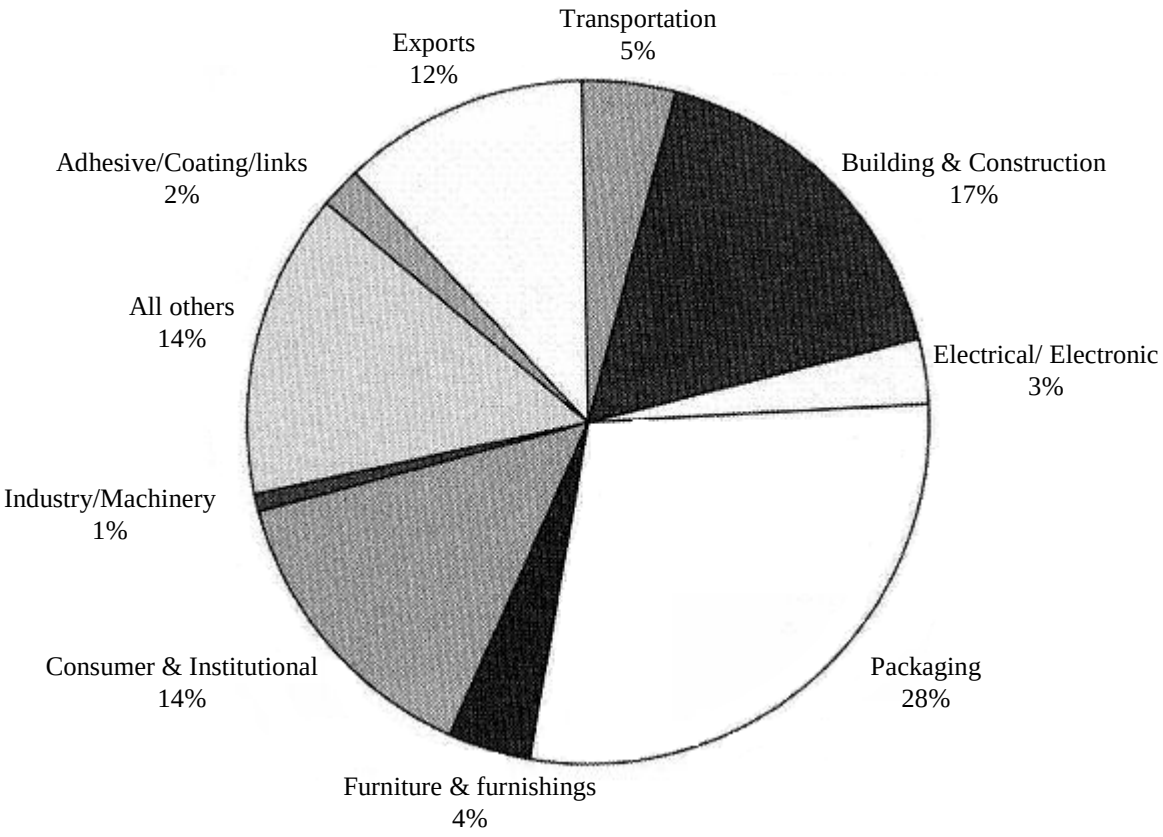

Figure 1.4 - Major Markets for Thermoplastic Resins

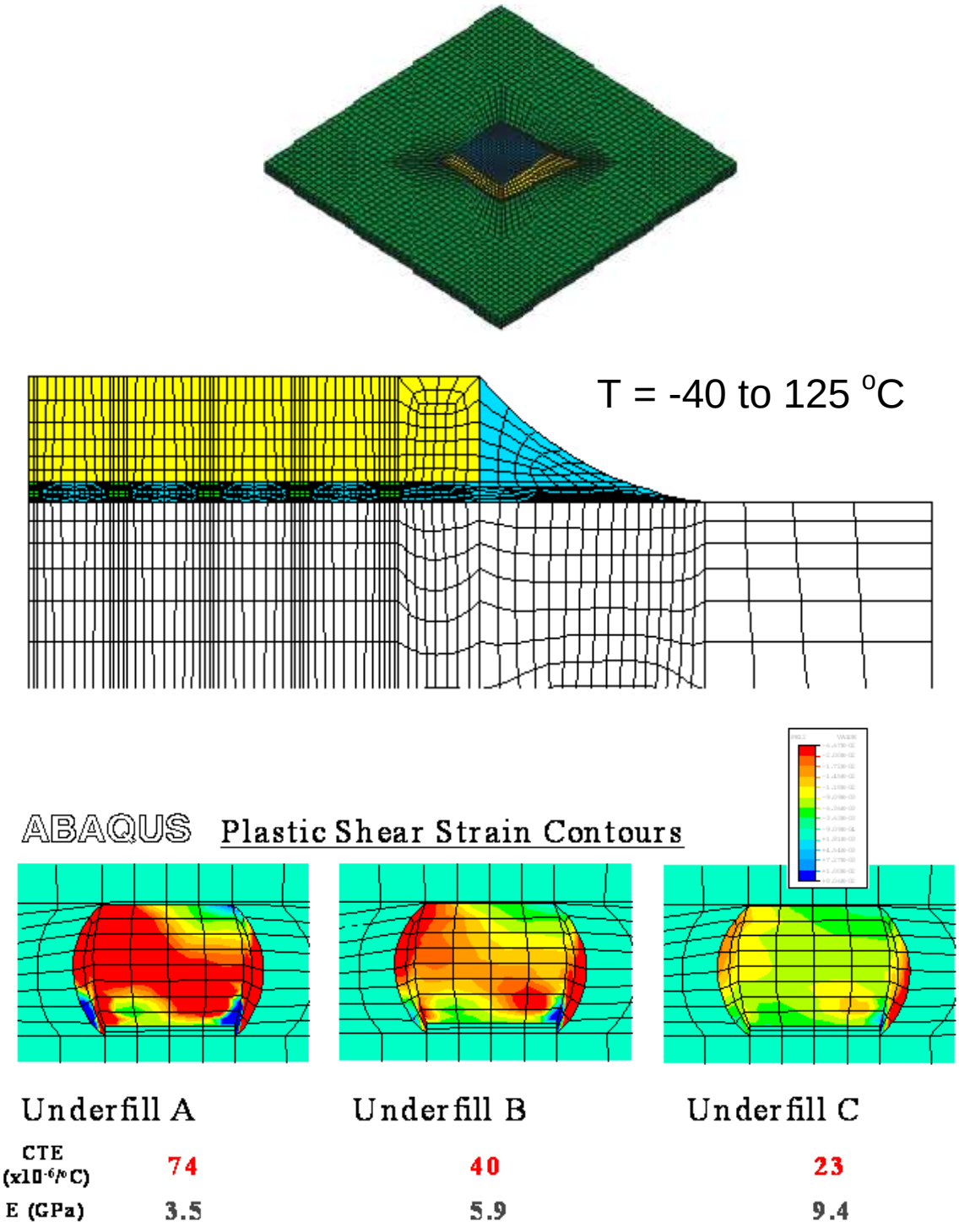

Figure 1.5 - Solder Joint Strain Prediction for Different Underfill Properties

1.5 Underfill Flow Process

A schematic of a flip chip assembly with underfill material is shown in Figure 1.6. Liquid underfills are thermally cured to form a heavily crosslinked molecular chain of solid state material. The flow characteristics of uncured underfill materials are critical to their application performance. These characteristics depend on its viscosity and dispense temperature, as well as the substrate material, chip passivation layer, solder bump pattern, and degree of curing. There are three major processing procedures used in flip chip on board assembly and three corresponding underfill categories: capillary underfill, no-flow underfill, and wafer-level underfill.

1.5.1 Capillary Underfill

Capillary underfills are the most widely used in flip chip packaging. Such materials will flow into the small gap between the chip and substrate via capillary action as shown in Figure 1.7. The encapsulant is dispensed along one side of the die after bump reflow and flows underneath the die and fills the gap between the die and chip carrier. The underfill epoxy is then cured by heating the assembly and holding it at an elevated temperature. This process is time consuming and a relatively expensive part of the manufacturing process. However, it is crucial to reliability improvement.

The filling dynamic process requires the underfill to be in a liquid state during the flow stage. This phenomenon is well understood within the realm of surface chemistry and fluid surface chemistry, and surface tension is the driving force that produces the capillary flow. The capillary underfill flow behavior can be modeled as a quasi-steady, laminar, incompressible, two

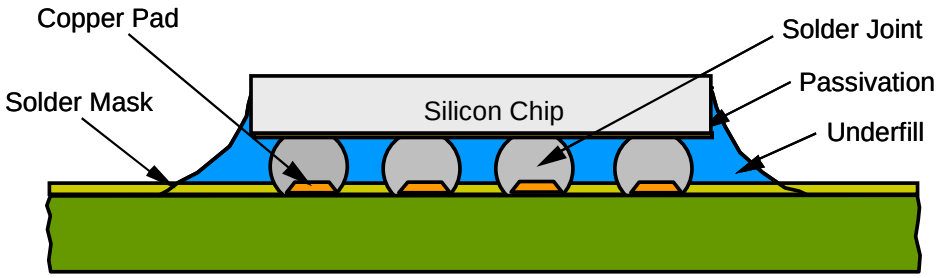

Figure 1.6 - Schematic of a Flip Chip Assembly with Underfill Material

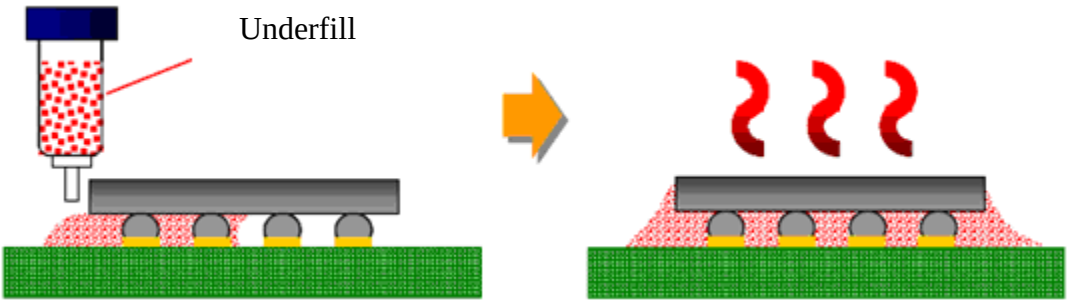

Figure 1.7 - Underfill Capillary Flow Process [9]

dimensional flow through a pair of parallel plates using the Washburn model [10-12]:

$$\frac{\partial p}{\partial x} = -\frac{12\mu}{h^2}\left(\frac{\partial L}{\partial t}\right) \tag{1.3}$$

where p is the pressure in the liquid at the position x, μ is the absolute viscosity, h is the gap height, and L is the flow distance (see Figure 1.8). The driving force for the flow is the pressure difference (Δp) between the underfill and the air, which is a function of surface tension (γ), gap height (h), and contact angle (θ):

$$\Delta p = \frac{2\gamma\cos\theta}{h} \tag{1.4}$$

By solving equations (1.3) and (1.4), the time for the underfill material to fill the gap can be estimated by [10, 12, 13]:

$$t = \frac{3\mu L^2}{h\gamma\cos\theta} = \frac{3\mu L^2}{h\gamma} \qquad (\cos\theta \approx 1) \tag{1.5}$$

From the expression in equation (1.5), it is clearly evident that the fill time is proportional to the viscosity and square of the distance traveled, and inversely proportional to the surface tension of the materials and standoff gap height. Normally, the underfill, board, and components are all preheated to an elevated temperature to decrease the underfill viscosity, and this improves the wetting and flowability. Although earlier capillary underfills experienced “snail paced” flow rates due to higher viscosity resins and poor filler morphology, new underfill materials flow rapidly and “snap” cure in minutes, significantly improving manufacturing throughput. The general performance of underfill flow and curing times are summarized in Table 1.2 [14].

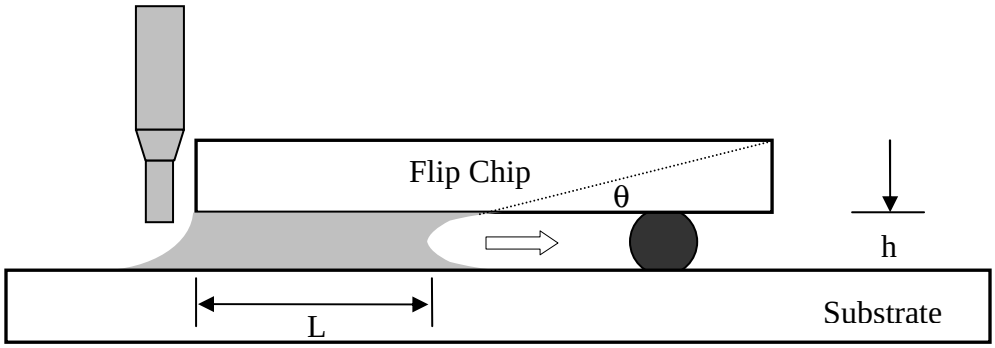

Figure 1.8 - Underfill Capillary Flow Process Parameters

1.5.2 No-Flow Underfill

Further improvements to the traditional capillary underfill process include the use of no-flow underfill, which eliminates the time consuming flow process. A fluxing controlled volume of underfill is dispensed directly onto bond sites before chip placement, as shown in Figure 1.9. The chip is then placed onto the bonding sites, compressing the liquid underfill and causing it to flow outward to the edges of the chip until the solder bumps contact the substrate pads. Compressing the underfill, producing a symmetrical outward flow pattern, helps to displace air and may be an attractive alternative process.

By adding a flux agent to the underfill material, concerns about flux and underfill compatibility can be eliminated. Also, this process does not require a subsequent reflow, dispense and cure process. It therefore provides a significant reduction in process steps and time, improving both productivity and cost competitiveness. Some considerations specific to the no-flow underfill process are listed below:

- Smaller bump size reduces voids
- Larger pitch reduces voids
- Substrate temperature is critical for the underfill material to reduce voids
- Low deposition height increases voids and causes starvation
- High viscosity allows compression flow to dominate and is preferred
- Lower viscosity allows gravity to flow that increase voids

1.5.3 Wafer Level Underfill

Wafer applied underfill is a revolutionary approach whereby underfill is applied to a bumped die at the wafer level. Such underfill materials should be reworkable and retain their characteristics after assembly and any post processing steps. Wafer level underfills can reduce

Year	Flow Rate @ 80 °C	Cure Time
Pre-1995	<1 cm/min	3-6 hrs @ 150 °C
1995	2 cm/min	30 min @ 150 °C
1996	2.5 cm/min	15min @ 150 °C
1997	3 cm/min	5-6 min @ 165 °C
1998	3 to 3.5 cm/min	4-5 min @ 165 °C

Table 1.2 - Historical Underfill General Performance

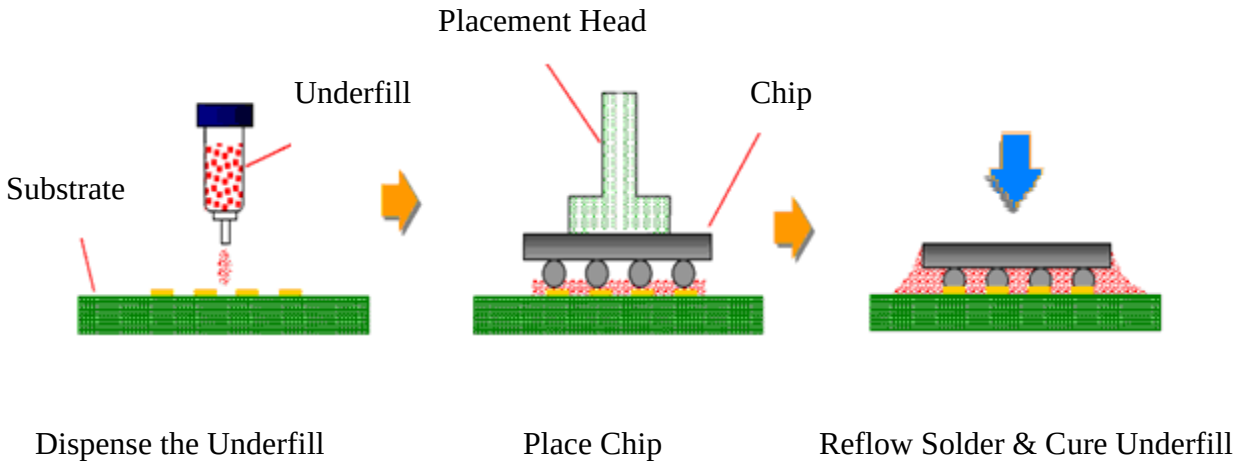

Figure 1.9 - No-Flow Underfill Process [9]

processing time and cost because there is no need for individual underfill dispensing (Figure 1.10).

Generally a specially designed B-stageable underfill is coated onto a bumped wafer. After the coated wafer is diced into individual die, a single chip will be selected and placed onto bonding pads and the solder interconnections and underfill bonding are formed during the reflow process. This approach can provide an efficient surface mount technology (SMT) process for flip chips by eliminating the steps of underfilling and curing each die. However, there are some challenging issues associated with wafer level processes. For example, specialized underfill materials must be developed that are stable at room temperature. They must also be able to re-liquefy during the reflow process, and they must form reliable interconnections after reflow.

1.6 Underfill Materials

After curing, the underfill materials used in flip chip assemblies are typically two phase composites consisting of an epoxy matrix filled with SiO_2 (fused silica) particles. For various applications, other small but necessary amounts of additives are also included in the epoxy formulations including fluxing agents, toughening agents, and adhesion promoters.

Epoxy, which is the term used for compounds containing oxirane groups, is the most common matrix for underfill materials due to its desirable characteristics of good adhesion, corrosion resistance, and physical and electrical properties. However, the CTE of epoxy alone is too high to meet the requirements in most flip chip applications (>80 ppm/°C), so silica fillers are added to reduce the CTE and increase the effective elastic modulus of the underfill material.

Underfill materials are then applied to fill the gap between the chip and the substrate, and also to bond with the solder joints. They also provide environmental protection for the solder

Underfill Applied Wafer and Dicing

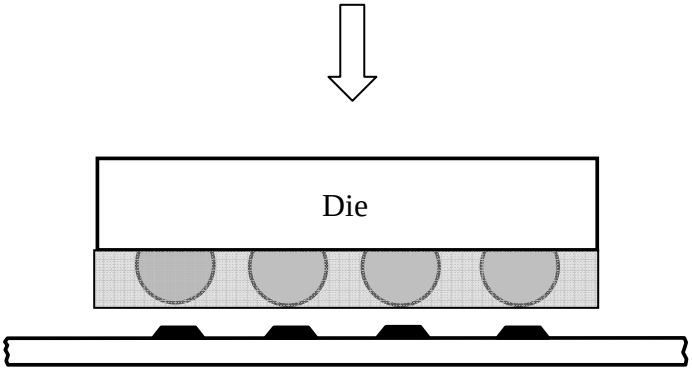

Single Die Flip Chip before Reflow

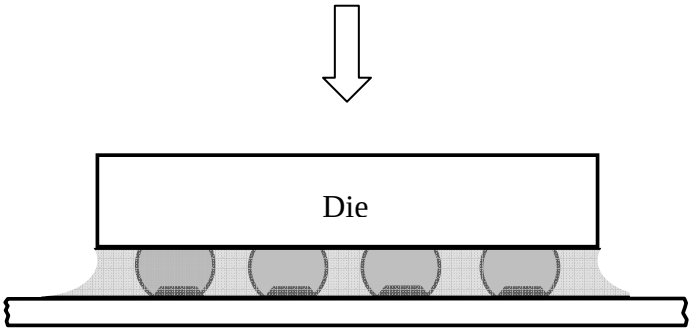

Single Die Flip Chip after Reflow

Figure 1.10 - Wafer Level Underfill Process

joints and improves electronic package reliability, as the stress/stain level in solder joints is redistributed among the underfill, chip, substrate and solder joints. Better underfill materials with desired values of CTE and elastic modulus are a key factor in the development of next generation low-cost, high-reliability flip chip technologies. The desirable characteristics and advantages of an underfill materials are listed in Table 1.3 [15].

Some other critical properties of uncured and cured capillary flow underfills are viscosity, glass transition temperature (T_g), adhesion strength, and adhesion retention. Low viscosity (fast flow) increases manufacturing throughput. The viscosity is affected by both filler content and particle size: the higher the filler content, the higher the viscosity, and the slower the flow rate; while a smaller filler size speeds up the flow rate. Higher temperatures can produce higher kinetic energy, thus particles will diffuse more rapidly at elevated temperature with higher viscosity [16].

Good interfacial adhesion is required for high wettability of the underfill material with both the silicon die passivation layer and the substrate surface (soldermask). Also, good adhesion retention requires that the underfill is not susceptible to environmental exposures such as constant temperature and humidity conditions, or thermal cycling.

Low CTE underfills are able to reduce the thermal expansion mismatches between the underfill and the chip, solder bumps, and PCB. This generally leads to better solder joint reliability. A high glass transition temperature (T_g) is generally desirable because the underfill material becomes soft, adversely affecting its mechanical properties (stiffness and strength) when the temperature is close to or above the T_g. A high elastic modulus helps counteract deformations due to CTE mismatches.

Characteristics	Advantages
High elastic E	Low stress and stain
High UTS	High level for the cracks
Low CTE	Lower CTE mismatch between chip and substrate
Low viscosity	Good flowability
Fine silica filler	To low the CTE and fill the small gap
Fast cure	Reduce the time and cost
Short fill time	Quick fill time and low cost

Table 1.3 - The General Desirable Characteristics and Advantages of an Underfill Material

The fundamental chemical differences between thermosetting and thermoplastic polymers are related the molecular bonding connections. Thermosets are crosslinked and have primary covalent bonding connections between molecular chains, while thermoplastics have only relatively weak secondary bonding connections between chains. Therefore, thermoplastics can be re-melted or re-molded, where thermosets cannot. Thermosetting epoxies are used in applications where high thermal and dimensional stability are required. The mechanical properties of underfills, such as its elastic modulus (E), ultimate tensile strength (UTS), and CTE, are all strongly linked to temperature. The glass transition temperature T_g is particularly important since the material characteristics undergo drastic changes around this temperature. The changes in relaxation modulus behavior with temperature are illustrated in Figure 1.11 for several different polymers [5].

The reliability of flip-chip technology using current underfill materials is generally lower than that of conventional wire-bond connection packaging materials such as epoxy molding compounds. The main reason for this relatively poor performance is the high coefficient of thermal expansion values and moisture absorption ratios of cured underfill materials. This results because underfill materials contain a smaller amount of silica filler than standard epoxy molding compounds to support good flowability during the underfilling process. This problem is likely a major contributor to the relatively poor reliability of flip chip IC assemblies [17].

When using underfill, delaminations at the underfill/die or underfill/substrate interfaces in flip chip assemblies become the primary failure modes. Such delaminations occur when the interfacial stresses are higher than the interfacial adhesion strength of the underfill polymer. Resistance to the initiation and growth of delaminations is therefore another critical issue for flip chip packages. If interfacial cracks develop and propagate to neighboring solder bumps, the

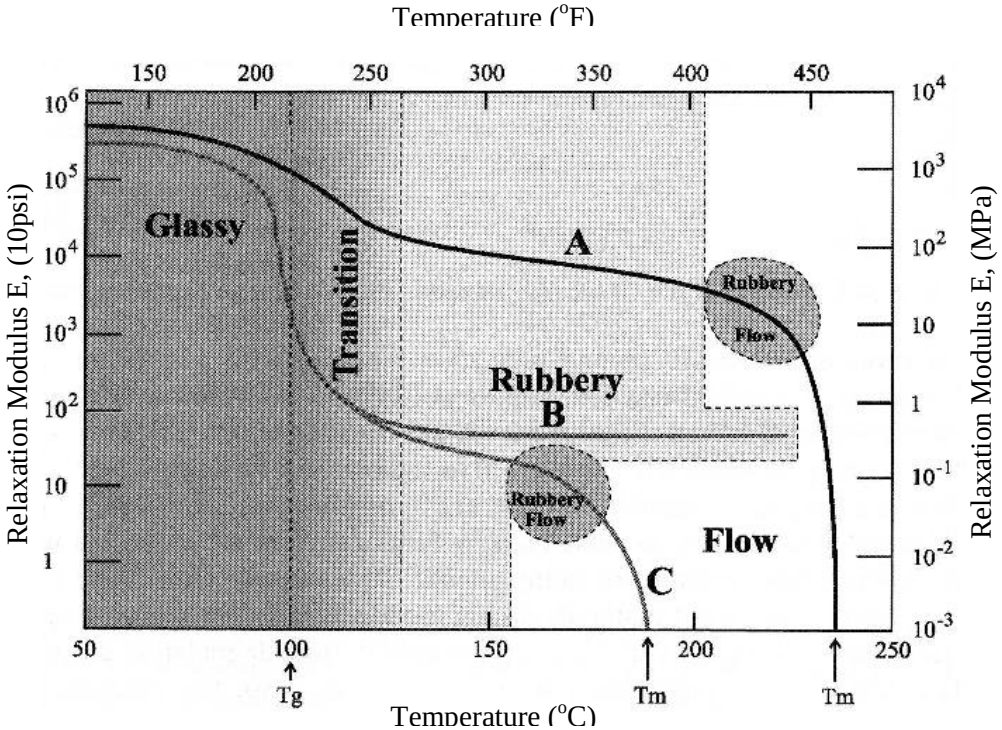

Figure 1.11 - Relaxation Modulus for A: Crystalline Polystyrene; B: Lightly Cross Linked Polystyrene; C: Amorphous Polystyrene [5]

previously described stress relief on the solder joints will be lost and the onset of solder joint fatigue cracking will be hastened.

1.7 Thermal Aging Process

Mechanical properties of a material can evolve as a function of time, temperature, and stress level. Of particular interest here is that the mechanical properties of an underfill can vary with time even when no stress is applied due to molecular structure changes over time. Two phenomena must be taken into account when considering these behaviors: physical aging and chemical aging.

It is well known that amorphous materials are not in thermodynamic equilibrium at temperatures below their glass transition temperature [18, 19]. Along with the evolution of state variables of volume or enthalpy, etc., there are some observable macroscopic property changes such as in the viscoelastic response and yield strength. Such phenomena are referred to as physical aging. The concept of free volume has been proposed to partially explain these behaviors [13-15]. In a closely packed system, the mobility of particles (M) depends on the free volume (V_f). When material is cooled from above T_g to below T_g, the free volume and mobility decrease simultaneously. However, if the free volume is greater than it would be in the equilibrium state, then it will continue to decrease slowly with time, and this is accompanied with a decrease in mobility. Therefore, the mechanical properties of the material also change during the aging process.

Meanwhile, chemical aging takes place when materials are exposed to elevated temperatures, the presence of humidity, and other environmental factors. This leads to permanent changes in the material structure as a result of breaking or forming covalent chemical bonds in the polymer molecular chains. Therefore, chemical aging is an irreversible process,

while physical aging is a reversible process [20]. In actual applications, chemical aging probably plays a decisive role in influencing the final properties of materials exposed to elevated temperature.

Struik [19, 21] investigated the effect of physical aging on many polymeric and non-polymeric materials, and found that momentary creep curves exhibit a universal shape, independent of chemical structure, thermal history, or test temperature. He also listed some basic aspects of the physical aging process in polymers:

- Aging affects properties primarily via changes in the relaxation times.
- Aging is thermo-reversible, and does not affect secondary relaxations.
- The aging range runs from above T_g to below T_g.
- In the aging range, aging time is the most relevant material parameter.
- In the aging range, the shift rate is close to unity for all polymers.
- In the aging range, the small strain behavior of all polymers is almost identical.
- Aging is a general phenomenon, and persists for very long periods of time.
- Aging disappears at low temperature

Due to the aging process, the mechanical properties of a polymer may change over time. However, analytical predictions of polymer strength and stiffness properties during irregular thermal or mechanical loadings are as yet extremely difficult. They can, however, be tested experimentally. For example, a study of one commercial polymer (D, L-lactide-co-glycolide) [22] revealed that tensile strength and shear strength exhibited a controlled decrease with aging time, as shown in Figure 1.12. After nine weeks of isothermal aging, the specimens were no longer strong enough to be tested mechanically.

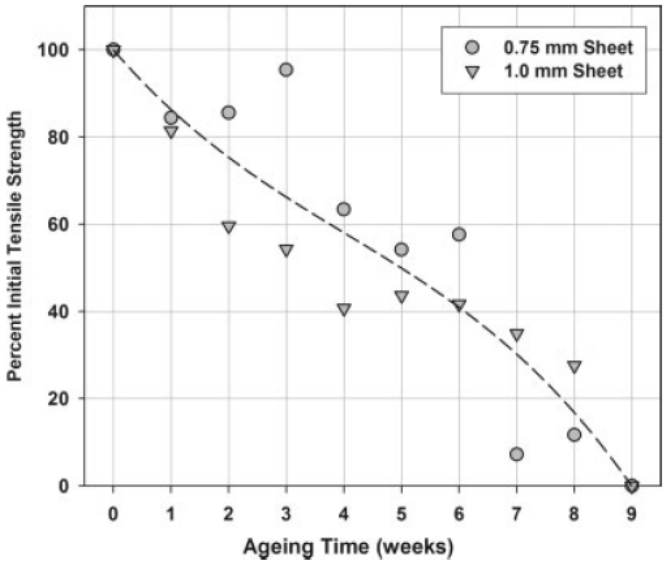

a) Percentage of Tensile Strength

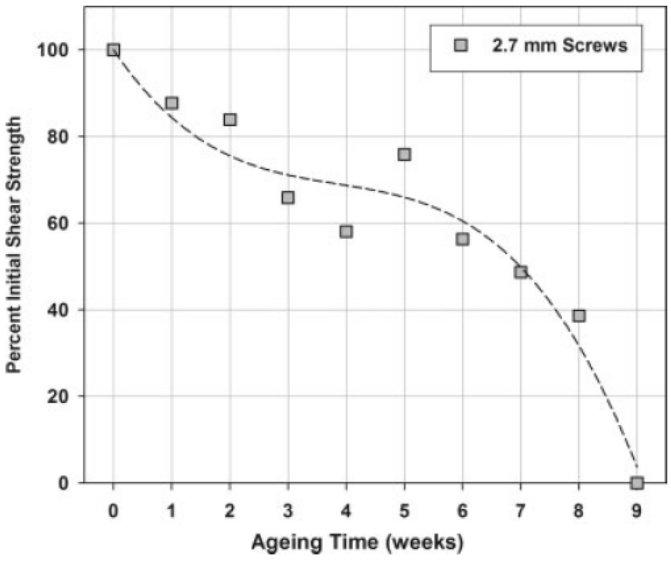

b) Percentage of Shear Strength

Figure 1.12 - Variation of Initial Tensile and Shear Strength for (D, L-lactide-co-glycolide) with Aging Time [22]

Also, during long term thermal aging, polymer materials become stiffer, which means the compliance is decreased (or modulus increased) over time compared to samples that have not experienced the aging process. A great deal of work has been done on evaluation of polymer creep behavior with aging. These studies have indicated that the creep compliance decreases with aging time and a master curve can be constructed, as in the examples shown in Figures 1.13 and 1.14 [23, 24]. For different aging times, the material creep compliance can be determined as in the isochronal plots in Figure 1.15 [13]. The material becomes stiffer as the aging progresses and the compliance value with 100 seconds aging time is reduced to around 60% of its initial value. Similarly, it is possible to incorporate momentary creep curves at different aging times into a single master curve by applying the shifting and superposition method described below.

Two principles, namely time temperature superposition (TTSP) and time stress superposition (TSSP), have been developed in order to estimate a material's mechanical properties by forming a master curve based on the results of multiple experimental tests, as shown in Figure 1.16 [5, 24]. TTSP permits users to substitute temperature for time, and thus perform short tests at various temperatures to predict the modulus as a function of a wide time period; whereas TSSP is able to perform the equivalent substitution of stress for time. TTSP and TSSP can be combined into a master curve by shifting individual curves as a function of temperature or stress, while the relevant shift factors can be evaluated by applying the Williams-Landel-Ferry (WLF) equation:

$$\log_{10} a_T = \log_{10} \frac{\tau(T)}{\tau(T_0)} = \frac{-C_1(T-T_0)}{C_2+(T-T_0)} \tag{1.6}$$

The WLF equation was developed from empirical curve fitting and C_1 and C_2 vary with different polymers. Ferry has proposed the use of the following “universal” constants, where T_0 is taken to be T_g, the glass transition temperature [25]:

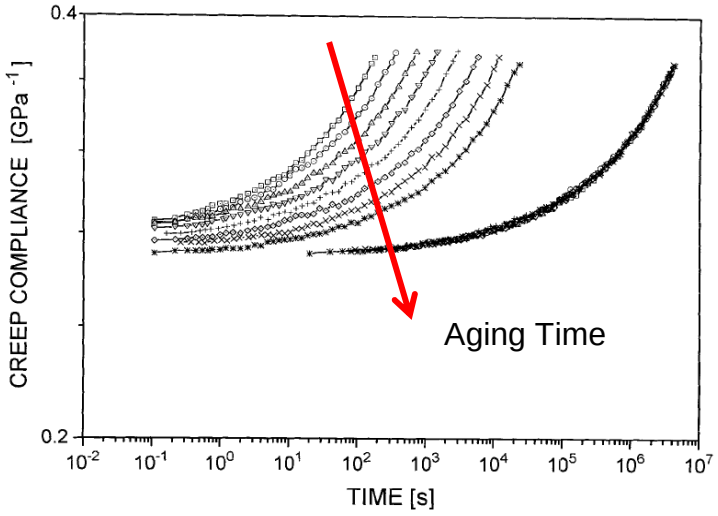

Figure 1.13 - Creep Compliance Curves for Syndiotactic Polystyrene (SPS140A) [24]

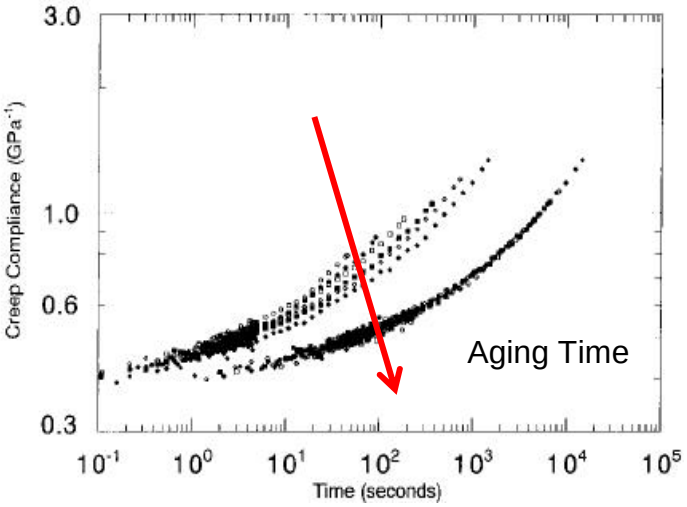

Figure 1.14 - Creep Compliance Curves for DGEBA/400 Diamine Epoxy Glass with 0.05% Mass Fraction CTBN Rubber [23]

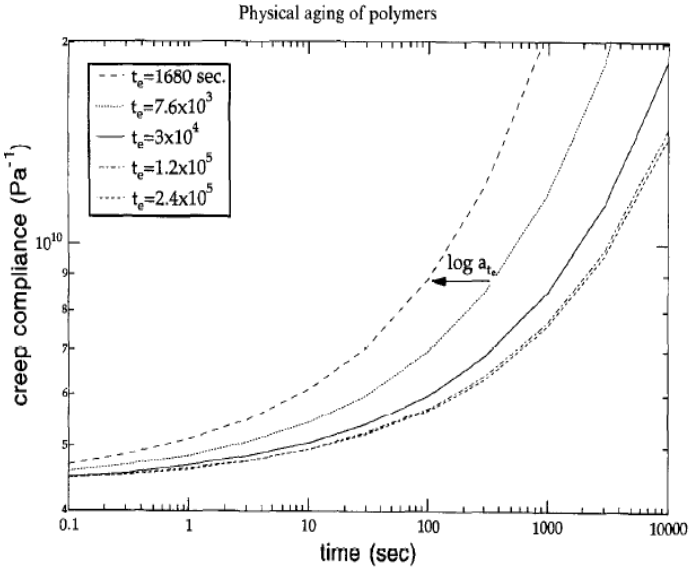

a.) Creep Curves for Different Aging Time

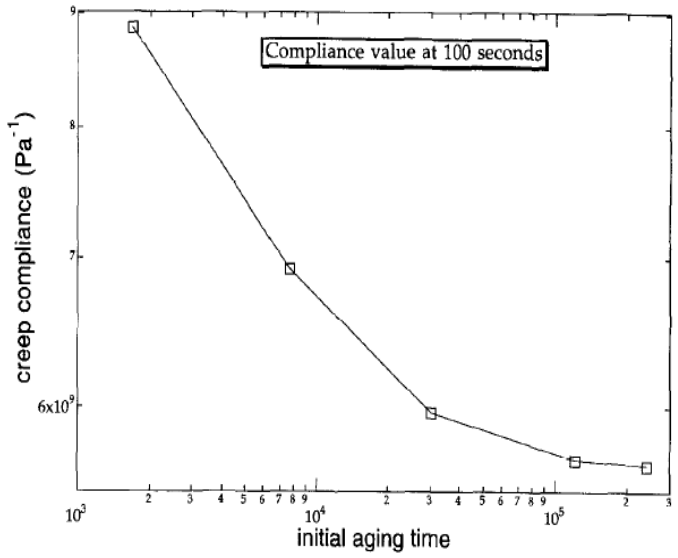

b.) Isochronal Values of Compliance

Figure 1.15 - Variation of the Creep Response of Epoxy with Aging Time [13]

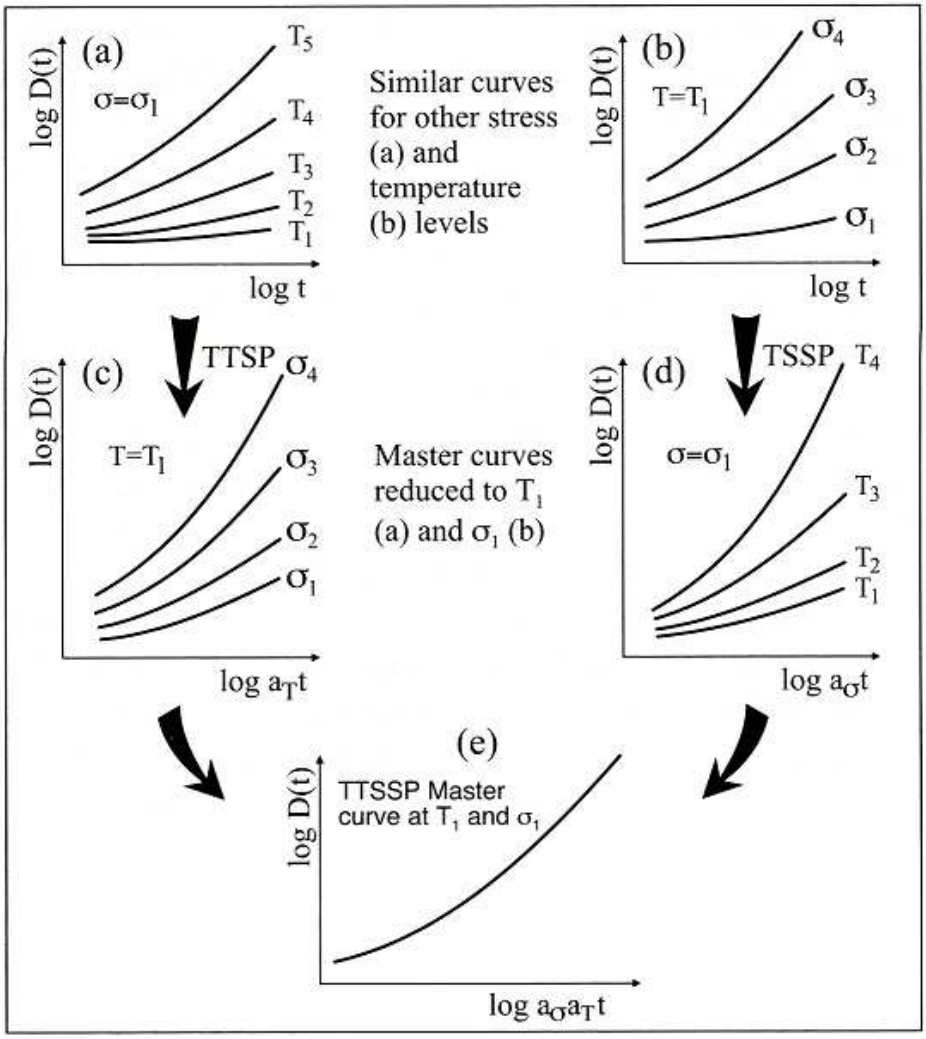

Figure 1.16 - Combination of TTSP and TSSP to Form a Master Curve [5, 24]

$$C_1 = 17.4, C_2 = 51.6 \quad (1.7)$$

It is important to note that the application of the WLF equation is limited to temperatures below the glass transition temperature, where amorphous polymers become sufficiently rigid for use in electronic assemblies.

Finite element analysis (FEA) has been widely used to simulate the reliability of flip chip on laminate assemblies subjected to thermal cycling (e.g. -40 to 125 °C) because of the long time and high costs involved to test the numerous new underfill materials emerging every year. However, the validity of the FEA simulation results depends strongly on the accuracy of the relevant material properties used for the analysis. Underfills exhibit a complicated viscoplastic mechanic response that is highly sensitive to temperature, isothermal aging and thermal cycling effects, among others. However, data on underfill mechanical properties are scarce on vendor datasheets. In order to accurately model the behavior of underfills and other microelectronic encapsulants, detailed information on time and temperature dependent mechanical properties must be available. Therefore, the primary goal of this research is to provide simple but accurate mathematic models that can be applied to predict evolution of the mechanical properties of underfill materials subjected to isothermal aging.

1.8 Research Objectives

Although there are already many studies on the characterization of the mechanical properties (stress-strain and creep) of underfill materials, the understanding of the effects of isothermal aging on the material behaviors remains inadequate. Challenges and fundamental problems still need to be addressed to support successful underfill applications and ensure a long working life. Finite element analysis can be used to improve the reliability of flip chip electronic packaging. However, confidence in the results generated by FEA requires systematic

experimental data, and appropriate models that accurately describe the deformation behavior of the utilized underfills.

The objectives of this research are to investigate the fundamental mechanical behaviors of underfill materials under various strain rates, isothermal aging processes, curing profiles and humidity levels as listed below:

- Characterize the effect of the strain rate on underfill stress-strain behavior.
- Characterize the effect of isothermal aging on underfill stress-strain behavior.
    1) Effect of different aging temperatures.
    2) Effect of different aging times.
    3) Effect of different testing temperatures.
- Develop mathematical models for:
    1) The effect of strain rate on elastic modulus and ultimate tensile strength.
    2) The effect of isothermal aging on elastic modulus and ultimate tensile strength.
- Investigate changes in creep behavior occurring in underfill encapsulants exposed to isothermal aging at elevated temperatures:
    1) Characterize the effect of isothermal aging on creep curves.
    2) Characterize the effect of isothermal aging on secondary creep rate.
- Develop an understanding of the effects of aging temperature, aging time, and testing temperature on underfill creep behavior.
- Develop mathematical models to describe the effects of isothermal aging on the secondary creep rate of underfill. Provide basic underfill mechanical property data for finite element analyses of flip chip on laminate assemblies.

CHAPTER 2

SPECIMEN PREPARATION AND UNIAXIAL TESTING

2.1 Introduction

There are some major challenges involved in building material property databases for underfills using representative uniaxial test samples for mechanical testing. There are several possible approaches to making uniaxial specimens of underfill material, and there are no standards governing the specimen preparation process. Additional problems arise due to the side effects of the chemical agents involved, and the existing mechanical property data are widely scattered. Consequently, for this research a unique and controllable process had to be developed.

In actual flip chip manufactured assemblies, the thickness of the underfill layer is very thin, typically about 75-125 μm (3-5 mils). Thus, the underfill layer cures relatively evenly, with a cure profile that is dependent on the oven temperature profile, the thermal properties of the materials, and configuration of the assembly materials. However, if large bulk strip samples of underfill are prepared for material characterization using a molding procedure, it is likely that they will be subjected to non-uniform curing and thus will not accurately represent the mechanical response of actual flip chip underfill layers [10]. If thin samples are manufactured, great care must be taken to achieve the correct cure profile, constant thickness, and desired shape, all of which are critical. For any size specimen, a method must be developed for

extracting cured test samples from the mold without inflicting damage or chemically changing the material. This can be challenging since underfills are, by their nature, effective adhesives.

Qian and coworkers [26] reported mechanical measurements on small underfill test samples. In their work, 0.5 mm (20-mil) thick samples were prepared in a metal mold exposed to the cure profile recommended by the underfill vendor (Figure 2.1). The samples were then cut by a diamond saw to have four to five times the thickness of true underfill samples. However, the metal mold required the use of a release agent, which chemically altered the surface of the underfill samples.

In the work of Rao, et al. [27], small samples were cast in a dog bone shaped Teflon mold (Figure 2.2). The samples in this study were 0.5 mm thick and the group used a Dynamic Mechanical Analyzer (DMA) to characterize the stress-strain curves, temperature dependent storage, and loss moduli of the underfills.

A method for generating thin (0.1 mm thick) underfill test samples was developed by Shi, et al. [28], who performed comprehensive mechanical testing on a typical underfill material over a range of temperatures and strain rates. A rather complicated molding procedure was utilized to fabricate the specimens. The mold included metal top and bottom plates made of steel and aluminum, respectively; and a thin silicone rubber middle layer (with a thickness of 0.1 mm in its compressed state) with a rectangular 20 x 3 mm cutout to define the in-plane dimensions of the test specimens. The sample preparation procedure involved pouring the underfill into the uncovered heated mold and then placing the steel cover onto the filled silicone rubber middle layer. Surplus underfill was extruded under pressure through an exit trough and the completed mold stack was placed in a box oven for curing. After molding, it was necessary to use fine

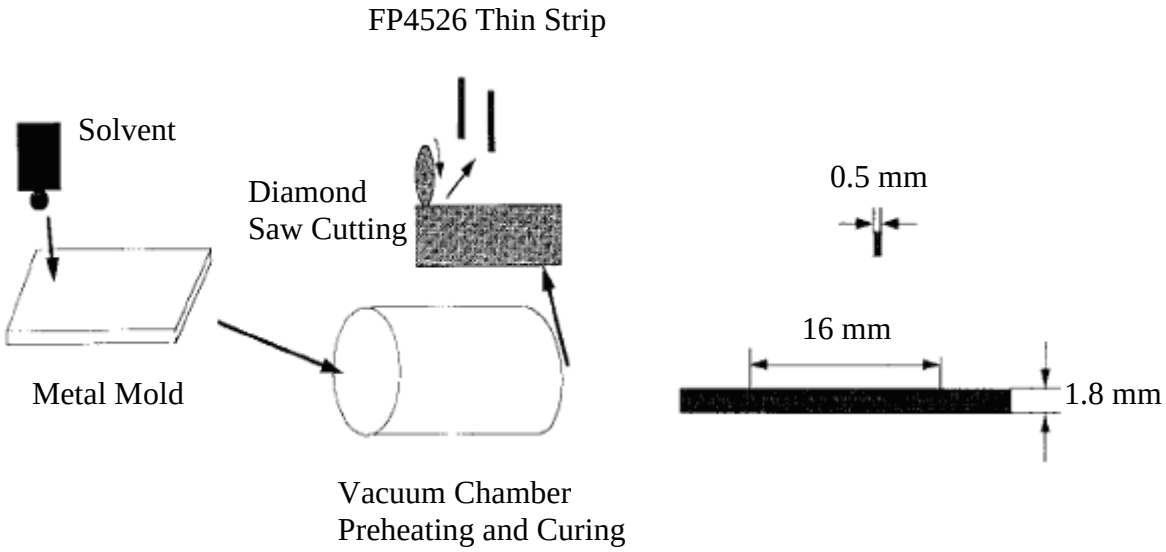

Figure 2.1 - Samples Used by Qian and coworkers [26]

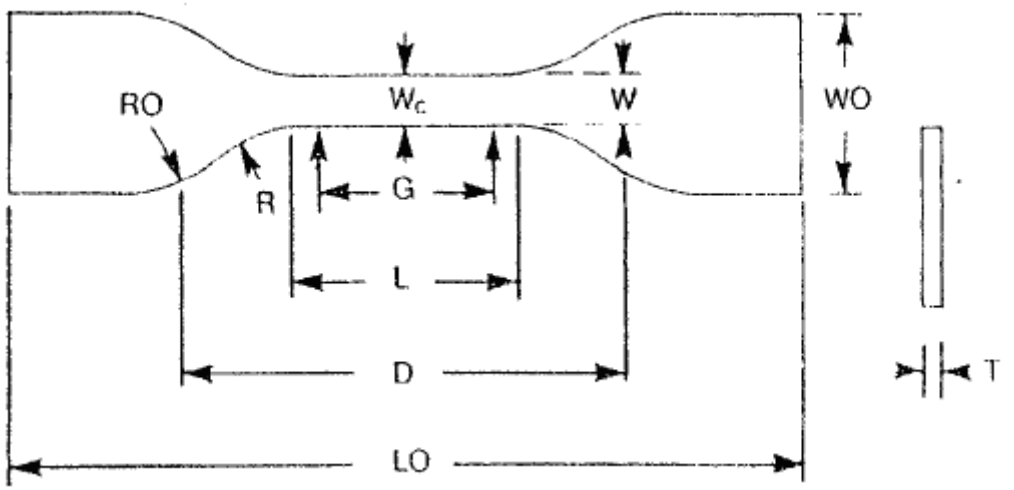

w-width of narrow section	2.5 mm	G-Gage length	7.5 mm
L-length of narrow section	10 mm	D-Distance between grips	25 mm
WO-width of overall	10 mm	R-Radius of fillet	15 mm
Lo-length overall	50 mm	RO-Outer radius	--

Figure 2.2 - Samples Used by Rao, et al. [27]

sandpaper on the samples to remove undesired material and adjust the specimen dimensions. The completed samples had nominal dimensions of 20 x 3 x 0.1 mm. However, 10 mm of the length of the samples were buried in the specimen grips, leaving only a 10 x 3 x 0.1 mm sample of underfill subjected to stress and strain. The length to width aspect ratio of these samples was therefore only 3.33, while at least 10 is typically desired to yield a reasonably pure uniaxial stress state in the specimen (Figure 2.3).

Kuo, et al. [29] developed a similar method to fabricate freestanding thin sheets of underfill material by dispensing and curing the material between Teflon coated sheets (Figure 2.4). They then cut samples with dimensions of 20 x 6 mm between the specimen grips (once again with an aspect ratio of 3.33), and performed investigations on the effects of temperature and strain rate on the tensile stress-strain behavior. This process was found to be an efficient way to remove the solvent and residual moisture on the substrate surface.

Building on prior work by members of the author's research group [30], a new specimen preparation procedure for underfill mechanical testing was developed for this study that yields 90 × 3 mm samples of the desired thickness (i.e., 0.075 - 0.125 mm). During the tests, the active area of the extracted tensile samples (the region between the specimen grips) is 60 x 3 mm, giving a highly desirable aspect ratio of 20. Using these samples, a microscale tension-torsion testing machine was applied to evaluate the uniaxial tensile stress-strain behavior of the underfill materials as a function of temperature and strain rate. The results revealed that a three parameter hyperbolic tangent empirical model provides accurate fits to the observed underfill nonlinear stress-strain behavior over a range of temperatures and strain rates.

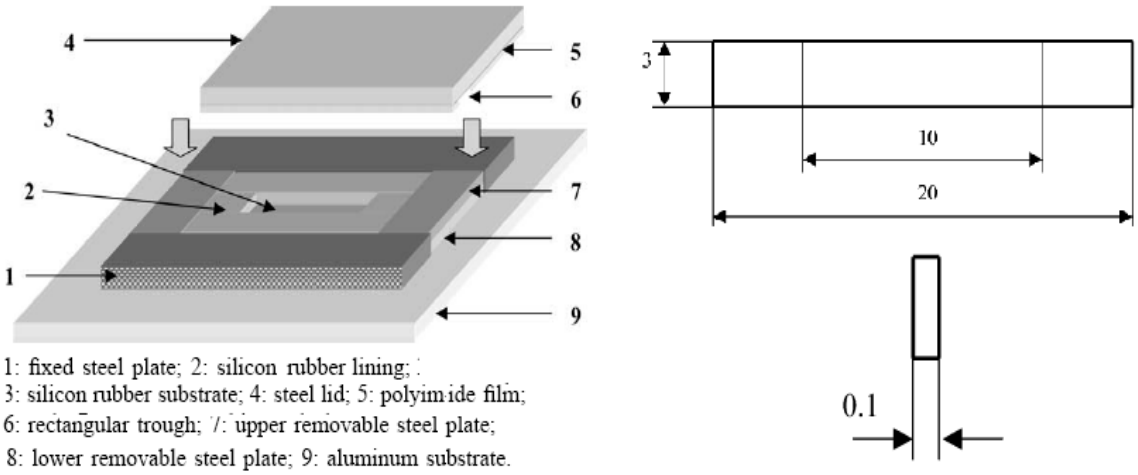

Figure 2.3 - Mold and Samples used by Shi, et al. [28]

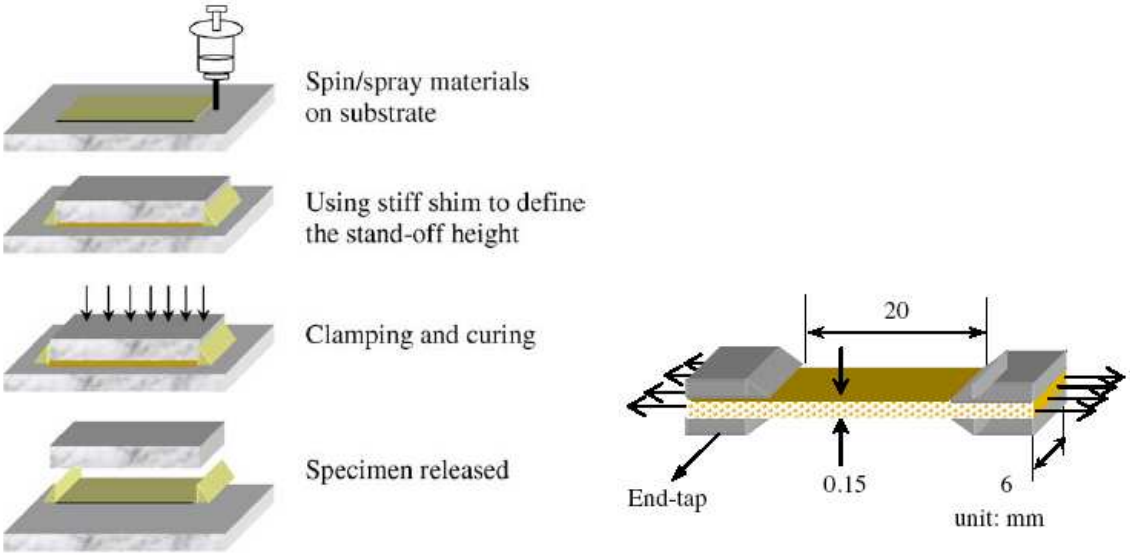

Figure 2.4 - Fabrication Process and Samples used by Kuo, et al. [29]

2.2 Experimental Underfill Material

Underfill material is a special colloidal dispersion epoxy with fillers consisting of silicon dioxide particles incorporated into the organic liquid. The specimen material, supplied by Lord Corporation (Thermoset), is Circuit SAF ME-525 flip chip underfill encapsulant. In this work, the material is referred to as UF1. It is a fast cure semiconductor grade epoxy system that reduces stress and adheres well to a variety of surfaces. Due to its low viscosity, it can flow rapidly under devices with stand-offs as low as 25 μm.

General information for this underfill is listed in Table 2.1. The manufacturer's suggested curing procedure is to cure at 150 °C for 30 minutes. The vendor datasheet values of the glass transition temperature and the coefficient of thermal expansion are shown in Table 2.2. This material has been observed to have good adhesion to laminate, ceramic, solder mask, and metal surfaces.

The underfill material microstructure and spherical silica filler are shown in the SEM image in Figure 2.5, in which the settling of the silica particles due to the higher density of the silica filler over the epoxy matrix is clearly visible. There is a thin layer of pure epoxy on the top surface, with increasing amounts of the large size silica filler accumulating towards the lower surface. The average size of the filler increases with depth, and the maximum diameter of the silica filler is about 10 μm. This epoxy composite has a relatively low coefficient of thermal expansion (CTE) that closely matches that of the solder bumps and thus minimizes the likelihood of crack initiation during thermal shock and thermal cycle testing.

A typical experimental TMA result is shown in Figure 2.6. The glass transition temperature marks the boundary between the two regions, and the CTE is 18.59 x 10^{-6} (1/ °C) and 72.61 x 10^{-6} (1/ °C), respectively, when the temperature is below and above the T_g.

Ingredient	Weight %
Bisphenol F Type Epoxy	12%
Other Epoxy: Multifunctional Epoxy Resins	5%
Anhydride: HHPA or Similar Hexahydrophthalic Anhydride	15%
Filler, Fused Silica	65%
Other Ingredients	3%

Table 2.1 - Underfill Material Composition

Underfill Material	T_g	CTE α ($1/^oC$) (Below T_g)	Recommended Cure Conditions
UF1	137 °C	25×10^{-6}	150 °C / 30 min

Table 2.2 - Underfill Material Characteristics and Cure Procedure

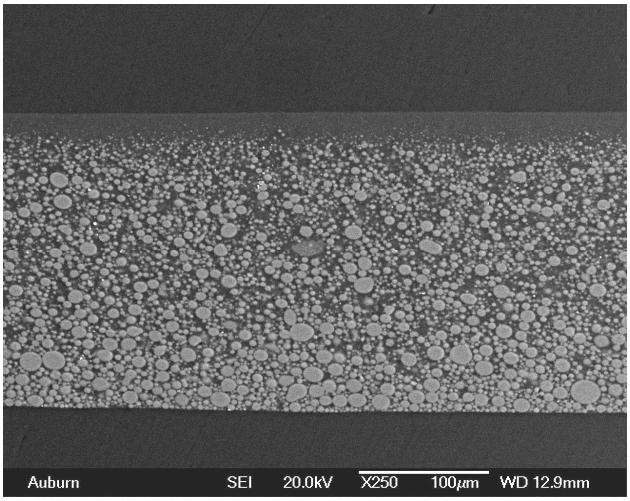

Figure 2.5 - Microstructure of the Underfill Material with Silica Filler

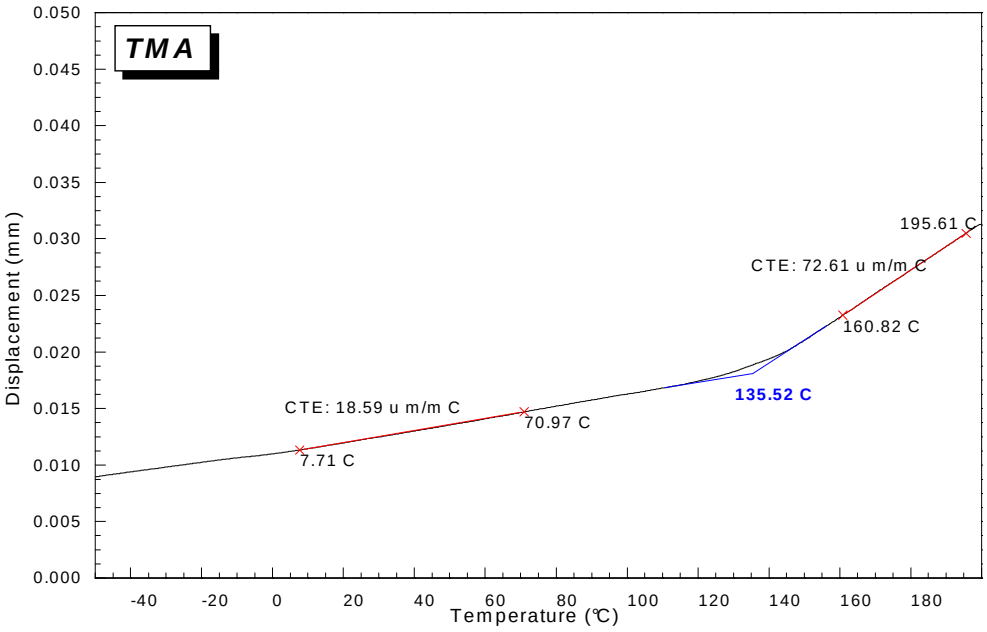

Figure 2.6 - Thermo-Expansion TMA Test Results for the Underfill Material

According to the manufacturer, the combination of a moderate T_g and modulus, along with excellent thermal shock performance, makes this underfill material well suited to demanding, high-end ceramic and automotive applications. In contrast to the older underfill systems, it can be quickly cured in 30 minutes at 150 °C without the need to implement a two-step curing process to minimize stress. Due to its high purity formulation, it also provides the ionic purity level required for high-end microelectronics applications, thus minimizing the chances of ion-induced corrosion in these devices.

In summary, the commercial underfill utilized in this work, UF1 is a silica filled epoxy with Tg = 135 °C (TMA) and 145 °C (DMA). This underfill is widely used in high performance ceramic and automotive applications to lower the stress between the substrate and solder bumps.

2.3 Specimen Preparation Procedure

Frozen underfill syringes stored at -40 °C were allowed to reach room temperature before dispensing. A stacked assembly view of the uniaxial tension specimen mold utilized in this investigation is pictured in Figure 2.7. Various parts of the assembly were clamped together by removable end clips (not shown). The middle layer consisted of precision shims with a thickness of 125 μm (5 mils) that defined the sample thickness. Molds were made from steel and coated with a thin Teflon layer on all surfaces. The top portion of the mold assembly was machined to contain 9 rectangular crossbars (90 x 3 mm) with a constant separation maintained via the remaining steel material at the ends of the crossbars. The shims separating the two plates were located under the front and rear connecting regions of the steel sheet, not under the crossbars themselves. The crossbars define the specimen shape and the final specimen dimensions are shown in Figure 2.8.

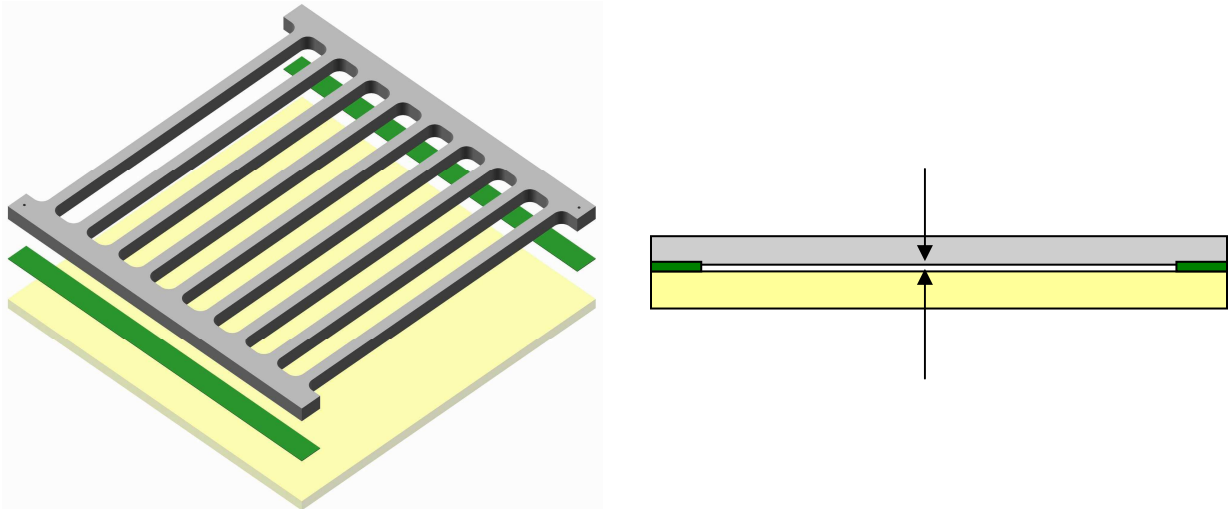

Figure 2.7 - Specimen Mold Assembly

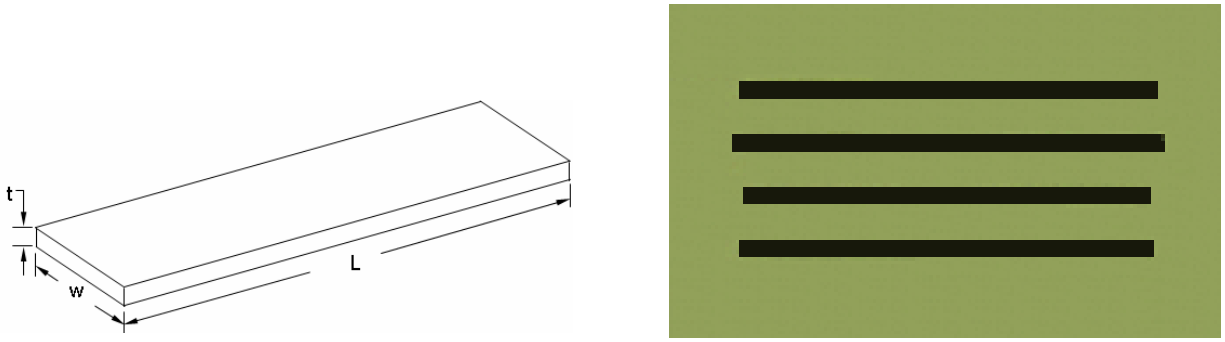

Dimension	Typical Values (mm)
Length	90
Width	3
Thickness	0.125

Figure 2.8 - Underfill Uniaxial Specimens and Final Dimensions

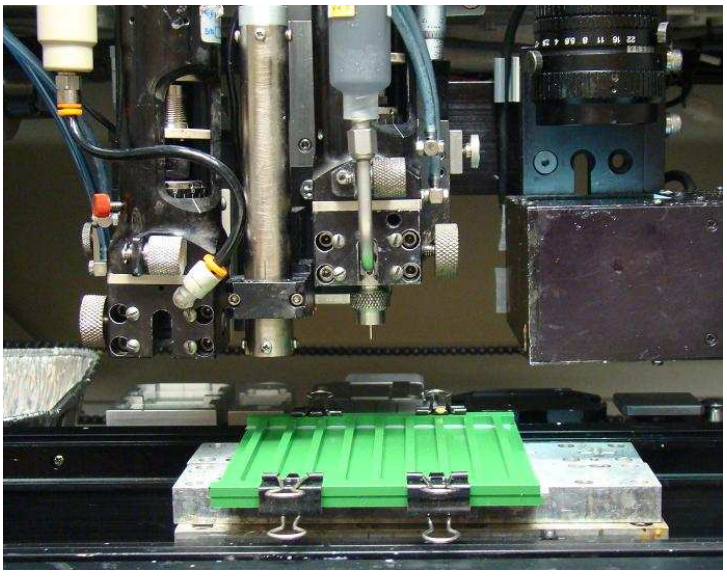

Figure 2.9 - CAM/ALOT System 3700 and Underfill Material Dispensing

A CAM/ALOT System 3700 machine was used to dispense the underfill material to the mold (Figure 2.9). The mold assembly was first heated to 80 °C in a box oven for about 10 minutes to remove all moisture. It was then preheated to 105 °C using a heat source located underneath the work station in the CAM/ALOT 3700, after which underfill encapsulant was dispensed along one side of each steel crossbar via a production line programmable dispensing system. Fiducial markings were included on the top of the steel sheet to aid in the programmability and repeatability of the dispensing procedure. Once dispensed, the underfill encapsulant quickly ran under the 5 mil thick gap under each crossbar via capillary flow. This procedure consistently produced constant thickness underfill regions, which were sandwiched between the Teflon coated top and bottom mold plates.

The uncured mold assemblies were then cured in a reflow oven at 150 °C for 30 min (Figure 2.10), using the vendor recommended underfill cure profile. The temperature profile during the underfill curing process is shown in Figure 2.11. After curing, the material was removed from the oven and cooled down to room temperature. Due to the Teflon coatings, the uniform thickness cured rectangular samples were easily separated from the mold. A razor blade and fine silica paper were used to trim any unevenness from the ends of the samples. Using the method described here produced samples with a controllable, constant thickness that were easily removed from the mold assembly without the need for chemical releasing agents. Therefore, no changes in the underfill mechanical behavior were induced by molding process. The lengths of the final trimmed samples were in the range of 70-90 mm, providing a specimen length to width aspect ratio of more than 20. An added benefit of this method was that the test samples were cured using the same production equipment and processing conditions used in industry. A comparison of the various specimen preparation methods is shown in Table 2.3.

Figure 2.10 - Underfill Material Curing Oven

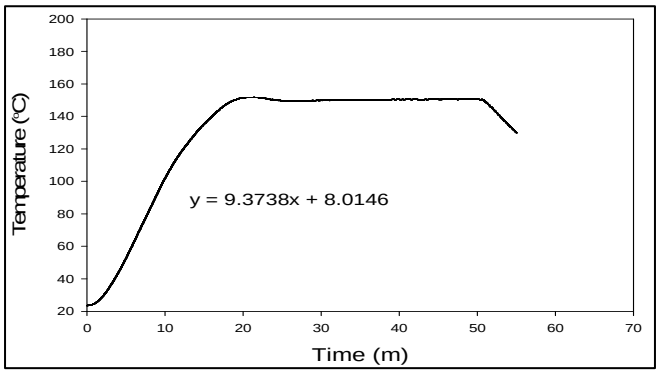

Figure 2.11 - Temperature Profile During the Underfill Material Curing Process

	Release Agent	Length/Width Ratio	Diamond Saw Cutting	After Molding Finishing
Qian [26]	Yes	8	Yes	No
Rao [27]	No	3	Yes	SiC paper
Shi [28]	Yes	3.3	No	SiC paper
Kuo [29]	No	3.3	Yes	SiC paper
Islam [30]	No	20	No	SiC paper

Table 2.3 - Comparison of the Specimen Preparation Methods

The steps involved in the new uniaxial specimen process for underfill materials proposed here are summarized below:

- Thaw the underfill material
- Mold dehydration at 80 °C for about 10 minutes.
- Pre-heat mold ambient temperature to 105 °C
- Align dispense process by fiducial markings
- Determine the height of the needle above the surface (z axis)
- Dispense underfill and post-heating – curing process
- Specimen release

2.4 Mechanical Testing System

In this study, the MT-200 microscale tension/torsion thermo-mechanical test system from Wisdom Technology, Inc. shown in Figure 2.13, along with its associated environmental chambers, was utilized to test the samples. According to the manufacturer's specification, the computer controlled actuators of the system provide an axial displacement resolution of 0.1 micron and a rotation resolution of 0.001°. A universal 6-axis load cell is utilized to enable users to simultaneously monitor three forces and three moments during sample mounting and testing, and then collect the data for further analysis. Testing can be performed in tension, shear, torsion, bending, and combinations of these loadings on small specimens such as those used in this research. In addition, cyclic (fatigue) testing can be performed at frequencies of up to 5 Hz. Hot and cold environmental chambers employ a resistance heater and liquid nitrogen diffuser to allow samples to be tested over temperature ranges of -185 to 25 °C and 25 to 300 °C, respectively. This system was used to fully characterize the underfill material. Uniaxial stress-strain tests were conducted with strain rates of $\dot{\varepsilon}$ = 0.001, 0.0001, 0.00001 sec^{-1}.

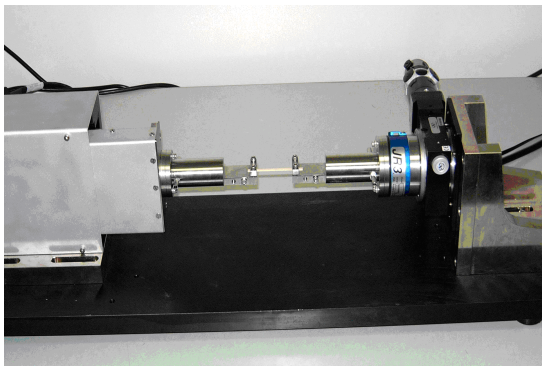

(a) Microscale Test System (MT-200)

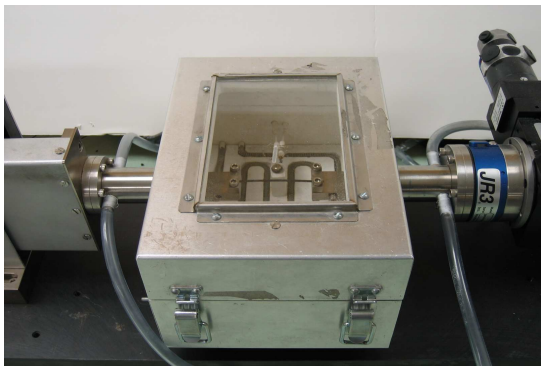

(b) Chamber for Elevated Temperature Testing (+25 to +300 °C)

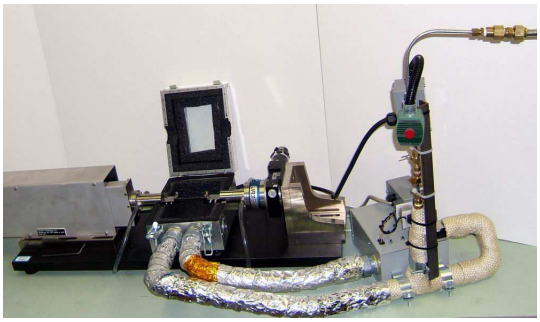

(c) Chamber for Low Temperature Testing (-185 to +25 °C)

Figure 2.12 - Testing System and Environment Chambers

Using the mechanical test system, tensile and creep tests were conducted. Specimen alignment and careful clamping techniques were used to obtain consistent and accurate testing results. Specimen alignment is a critical feature for the microtester because a small bending moment or torque could break thin brittle samples if they are not perfectly aligned. By carefully adjusting the corresponding stages during clamping, the initial forces were adjusted to be close to zero. Tensile tests were performed under displacement (stoke) control, giving the stress-stain relationship at a particular strain rate and testing temperature. The creep tests were performed under constant force mode, giving the strain response versus time under constant applied stress and temperature.

2.5 Experimental Method and Mechanical Properties

Due to the robustness and reliability required in flip chip packaging, the mechanical properties of the underfill material are very important. These were intensively investigated in this research and mathematical models were developed to fit the measured results. Uniaxial tensile stress-strain tests and creep tests were used to characterize the mechanical properties.

2.5.1 Tensile Stress Strain Properties

During uniaxial stress-strain testing, forces and displacements were measured. The axial stress and axial strain were calculated from the applied force and measured cross-head displacement as follows:

$$\sigma = \frac{F}{A} \tag{2.1}$$

$$\varepsilon = \frac{\Delta L}{L} = \frac{\delta}{L} \tag{2.2}$$

where σ is the uniaxial stress, ε is the uniaxial strain, F is the measured uniaxial force, A is the original cross-sectional area, δ is the measured cross-head displacement, and L is the specimen gage length (initial length between the grips). For the tests in this study, stroke (displacement) control was utilized.

Temperature has a major impact on material properties in polymers. The underfill material demonstrates five regions of viscoelastic behavior, namely the glassy, transition, rubbery, rubbery flow and liquid flow regions (Figure 1.11), although the last two are not seen in thermoset polymers. At sufficiently high temperatures, decreases in the material modulus lead to a significant change in properties.

Extensive work has been done on the results of polymer tensile tests, and various equations have been proposed by different authors to describe the mechanical properties of different kinds of underfill epoxy, as shown in Table 2.4. Although the variables in these models include factors such as testing temperature and strain rate, none consider the effect of aging, either in the form of aging time or aging temperature. To address this shortcoming, in this work constitutive models were developed to take into account isothermal aging effects.

2.5.2 Creep Properties

Another fundamental method used to characterize the viscoelastic time-dependent behavior of a polymer is the creep test. Creep deformation is particularly likely at elevated temperatures. In electronic packaging applications, creep failure is a well accepted mechanism; as solder ball joints cracks occur when packages are subjected to thermal or power cycling. In the creep test, a constant force is applied quasi-statically to a uniaxial tensile specimen and the resulting deformation of the material is observed over time. Creep behavior is the time dependent strain deformation at constant uniaxial stress and creep deformation is one of the

Model	Tested Material	Testing Type	Variables	Reference
$E = [f_0 + f_1 \times (1 - e^{f_2 \cdot T})] \cdot E_0$	Dexter Hysol	Tensile	T	Rao [4]
$E = E_1 \times (\log_{10} \dot{\varepsilon}) + E_2$	Lord	Tensile	$\dot{\varepsilon}$	Islam [30]
$E = E_0 + E_1 \ln \dot{\varepsilon} - CT(GPa)$	Hysol FP4526	Tensile	T, $\dot{\varepsilon}$	Qian [26]
$E/\sigma = C\dot{\varepsilon}^m$		Tensile	$\dot{\varepsilon}$	Hertzberg [31]
$E=\ln(a-bT)-ce^{(-d/T)}+E_1\ln\dot{\varepsilon}+E_0$ $T<T_g$ $=\ln(a-bT)-ce^{(-d/T)}+E_1\ln\dot{\varepsilon}+E_0$ $T>T_g$	Hysol FP4549	Tensile	T, $\dot{\varepsilon}$	Kuo [29]

Table 2.4 - Models for the Mechanical Properties of Epoxy Underfills

major failure modes in electronic packages. In this study, tests are carried by different loads at various temperatures for different prepared specimens.

Generally, a creep curve is composed of three stages, as shown in the typical creep curve in Figure 2.13. Once a constant load is applied, the initial instantaneous strain that is formed produces the primary creep, which consists of elastic or time-independent plastic deformation. This is followed by the secondary creep, or steady-state creep, which proceeds at a nearly constant rate. The secondary creep region is very important, as most of the deformation over the lifetime of a product takes place in this period. This is also the dominant deformation mode for underfill materials. In this stage the strain rate is retarded by strain-hardening due to the action of the molecular chains, which repair broken chains to strengthen the network. Finally, during the third stage of tertiary creep, the breakage of covalent bonds in the materials proceeds at an ever increasing rate and eventually the material fails in fracture.

There are several mathematical models capable of representing the creep behaviors of viscoelastic materials with good accuracy. The Boltzmann superposition principle is widely accepted as a linear viscoelastic model and is based on the assumption that the total strain can be determined from the algebraic sum of strains, no matter how the stress is applied. This can be represented in the hereditary integral form [32]:

$$\varepsilon(t) = \int_{-\infty}^{t} J(t-\tau)d\sigma(t) = \int_{-\infty}^{t} J(t-\tau)\frac{d\sigma(\tau)}{d\tau}d\tau \tag{2.3}$$

This equation can be used to determine the total strain for any general loading history.

An empirical power function with good accuracy over a wide span of time for creep response was proposed by Findley and Khosla [33]. This approach uses what may be described as a separable time-independent and time-dependent strain:

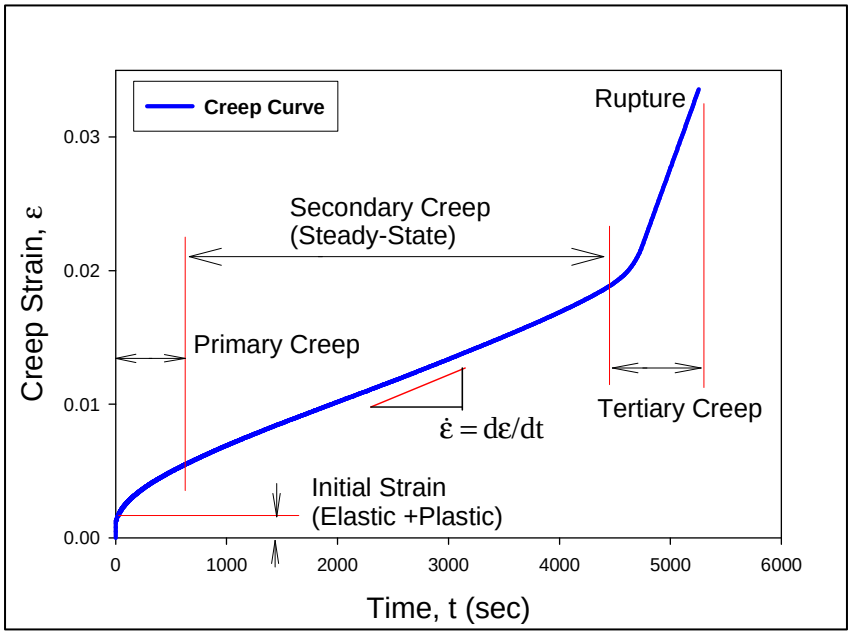

Figure 2.13 - A Typical Creep Curve

$$\varepsilon = \varepsilon_0 + \varepsilon' t^n \tag{2.4}$$

where t is the time, n is a constant independent of stress and is generally less than one, ε_0 is the time-independent strain, and ε' is the coefficient of time dependent term. Both ε_0 and ε' are functions of stress. This power law equation has been widely used for creep in several different polymers in tension, compression, torsion, etc. By rearranging and taking logarithms, equation (2.4) yields:

$$\log(\varepsilon - \varepsilon_0) = \log \varepsilon' + n \log t \tag{2.5}$$

In the resulting log-log plot, the value of n can be determined from the slope of the straight line response and ε' is the vertical axial intercept value. To consider the nonlinear range of stress, the coefficients in the creep law can be taken as stress dependent. For example:

$$\varepsilon = (\sigma / E) + k\sigma^p (a - e^{-ct}) + l\sigma^q t \tag{2.6}$$

Many mechanical models have been proposed to describe the nonlinear behavior of viscoelastic materials. For example, Eyring [34] suggested a hyperbolic sine law as below:

$$\dot{\varepsilon} = D \sinh \frac{\sigma}{\sigma'} \tag{2.7}$$

where D and σ' are constants.

Garofalo's hyperbolic sine law [10, 35, 36], expands on the Eyring relation and takes into account that steady state creep strain rates are strongly stress and temperature dependent:

$$\dot{\varepsilon} = C[\sinh(\alpha\sigma)]^n e^{\left(\frac{-Q}{RT}\right)} \tag{2.8}$$

where σ is the applied stress, T is the temperature, R is the universal gas constant, n is the stress exponent, Q is the activation energy, and α and C are material dependent constants.

Recently, The Anand model has been proposed as a unified model that does not require explicit yield conditions or loading/unloading criteria. The equation is expressed as:

$$\dot{\varepsilon}_P = A\left[\sinh\left(\frac{\xi\sigma}{s}\right)\right]^{\frac{1}{m}} e^{\left(-\frac{Q}{RT}\right)} \tag{2.9}$$

where $\dot{\varepsilon}_p$ is the inelastic strain rate, A is a constant, ξ is the stress multiplier, σ is the stress, R is the gas constant, m is the strain rate sensitivity, Q is the activation energy, and T is the absolute temperature. The flow equation can be easily modified to represent the hyperbolic sine model for secondary creep rate as shown in equation (2.8).

The Anand model also employs a single scalar internal variable *s* to represent the isotropic resistance to inelastic flow of the material. The scalar variable is related to the dynamic process of strain hardening and dynamic recovery:

$$\dot{s} = \left\{\left[h_0\left|1-\frac{s}{s^*}\right|\right]\frac{\left(1-\frac{s}{s^*}\right)}{\left|1-\frac{s}{s^*}\right|}\right\}\dot{\varepsilon}_p \tag{2.10}$$

and

$$s^* = \hat{s}\left[\frac{\dot{\varepsilon}_p}{A}e^{\left(\frac{Q}{RT}\right)}\right]^n \tag{2.11}$$

where s* represents a saturation value at a given temperature and strain rate, $\hat{s}$ is a coefficient and n is the strain rate sensitivity at the saturation condition. The nine constants presented in the above equations are A, Q, m, n, a, h_0, ξ, $\hat{s}$, and s_0, and the initial value of the deformation resistance must also be determined for the viscoplastic Anand model.

When using ANSYS finite element software to model steady state creep, the sinh law is included in the Anand model for the viscoplastic elements. A user defined model can be defined [10]:

$$\dot{\varepsilon} = C_1[\sinh(C_2\sigma)]^{C_3} e^{\left(-\frac{C_4}{T}\right)} \tag{2.12}$$

where C_1 to C_4 correspond with A, 1/m, ξ/s, and Q/k, respectively. However, viscoplastic element models only apply to elasticity and steady state creep, not plasticity, because they lead to increasing error when the deformation is low or the strain rate is high. In an attempt to address this shortcoming, a double power law model has been proposed to overcome the absence of plastic behavior in the Anand model [10]:

$$\dot{\varepsilon} = C_1 \sigma^{C_2} e^{(-\frac{C_3}{T})} + C_4 \sigma^{C_5} e^{(-\frac{C_6}{T})} \tag{2.13}$$

This is made up of two power law terms that need to be separately implemented for primary and secondary creep models, and the units for the parameters are listed below in Table 2.5.

Currently, most researchers use multiple variable fitting methods to determine the constants based on experimental data. The Anand model has been widely used in ANSYS software to solve the viscoelastic and plastic-elastic material problems.

Table 2.6 summarizes the constitutive models used for epoxy material creep curves and the secondary creep rate. The variables in these models include testing temperature, strain rate and stress level. However, but no aging parameters (e.g. aging time or aging temperature) have been taken into account in prior work.

Parameter	C_1	C_2	C_3	C_4	C_5	C_6	σ	T	$\dot{\varepsilon}$
Unit	s^{-1}	-	K	s^{-1}	-	K	MPa	K	s^{-1}

Table 2.5 - Table of Constant Values for the Parameters

Creep Curve	Power Law	
		$\varepsilon = \varepsilon_0 + \varepsilon' \times t^n$
		$\varepsilon = \varepsilon_0 + A_0(1-e^{-ct}) + Bt$
	Nutting Equation	$\varepsilon = k\sigma^p t^n$
	Hyperbolic Sine	$\varepsilon = \varepsilon_0 \sinh(\sigma/\sigma^0) + \varepsilon^+ t^n \sinh(\sigma/\sigma^+)$
Creep Stain Rate	Norton's Power Law	$\dot{\varepsilon} = A_1 \sigma^n e^{-\frac{Q}{RT}}$
	Arrhenius Power Law	$\dot{\varepsilon} = A_2 \frac{E}{T}(\frac{\sigma}{E})^n e^{-\frac{Q}{RT}}$
	Hyperbolic Sine Law	$\dot{\varepsilon} = D\sinh\frac{\sigma}{\sigma'}$
	Garofalo Hyperbolic Sine Law	$\dot{\varepsilon} = C[\sinh(\alpha\sigma)]^n e^{\left(\frac{-Q}{RT}\right)}$
	Anand Model Flow Rule	$\dot{\varepsilon}_P = A\left[\sinh\left(\frac{\xi\sigma}{s}\right)\right]^{\frac{1}{m}} e^{\left(-\frac{Q}{RT}\right)}$

Table 2.6 - Constitutive Models for Epoxy Creep Behavior

CHAPTER 3

EFFECTS OF TEMPERATURE AND STRAIN RATE ON THE PROPERTIES OF UNDERFILL

3.1 Introduction

The reliability of an electronic package is strongly dependent on the thermo-mechanical properties of its constituent materials. The thermo-mechanical behavior of an underfill is highly sensitive to temperature and strain rate because of its morphology of filled particles and polymer resin [26]. The detailed characterization of underfill materials is one of the major factors involved in the development of a new flip carrier product and largely determines its cycle and cost. One of the major challenges in flip chip package development is package cracking, particularly die cracking and underfill cracking [27].

Uniaxial tensile tests are usually performed on the underfill specimen to study its mechanical behavior. Underfill is often modeled using very simple elastic material concepts. Zhang and Shi [37] reviewed several modulus concepts for viscoelastic materials, and pointed out that constant strain rate tests were better able to characterize the stress-strain behavior and the elastic modulus. They also suggested that the tangent modulus, or the derivative of the stress-strain curve at a constant strain rate, corresponded exactly with the relaxation modulus from the stress relaxation test. It has also been shown that viscoelastic models for a polymeric encapsulant perform much better than elastic models, which induce significant errors due to a

lack of information concerning the time and temperature dependant properties of the polymer. Generally, two types of modeling approaches are used: linear elasticity and linear viscoelasticity [10]. The behavior of viscoelastic materials must be expressed by a constitutive equation which includes time as a variable. Viscoelastic material behavior is normally studied by three types of experiments: stress-strain tests under constant strain rate, creep test and stress relaxation tests [32].

Rao and coworkers [4] investigated three underfill materials, and used a dynamic mechanical analyzer DMA to obtain the stress-strain relationship under controlled force mode, the storage and loss moduli with multi-frequency vibration, and the stress relaxation behavior. They modeled the dependence of the elastic modulus on temperature using:

$$E = [f_0 + f_1(1 - e^{f_2 T})]E_0 \tag{3.1}$$

The strain rate effect was not taken into consideration.

Over the range of strain rates considered by Islam, the elastic modulus shows a linear dependence on the logarithmic strain rate at each temperature [38]:

$$E = E_1(\log_{10}\dot{\varepsilon}) + E_2 \tag{3.2}$$

where E_1 and E_2 are temperature dependent material constants. Similar results were reported by Shi. etc [39].

Qian, et al. [26, 40] studied the viscoelastic-plastic properties of the HYSOL FP4526 underfill, and proposed a constitutive model for underfill material behavior. In their work, which was well below the glass transition temperature, the elastic modulus was expressed as:

$$E = 17.3145 + (0.1871)\ln\dot{\varepsilon} - (0.02795)T \ \text{(GPa)} \tag{3.3}$$

where T is the absolute temperature and

$$\dot{\varepsilon} = \sqrt{\frac{2}{3}\dot{\varepsilon}_{ij}\,\dot{\varepsilon}_{ij}} \tag{3.4}$$

is the von Mises strain rate. Furthermore, the same group used a set of three dimensional constitutive equations to fit and predict the stress-strain experimental curves. They suggested that this framework also shows potential for the study and design of flip chips and packages.

Kuo and coworkers [29] suggested a way to model the dependence of the elastic modulus on temperature and strain rate by using separate equations above and below the glass transition temperature of the underfill material. They also predicted the creep behavior at different test temperatures and stress levels by using a hyperbolic-sine power law equation. Ernst and coworkers [41] studied changes in the viscoelastic properties during the curing process by applying the constitutive curing theory. In their work, the mechanical properties, time dependent stiffness function, and initial strain evolution were established by means of specially designed DMA measurements.

In conclusion, there have been limited prior studies on underfill that have included the effects of viscoelasticity on their properties and behavior.

3.2 Objectives and Testing Program

In this chapter, the mechanical behavior of a particular underfill (UF1) was explored using stress-strain tests at different temperatures and strain rates. The uniaxial tensile specimens for mechanical testing were prepared using the method described previously in Section 2.3. The uniform specimens produced had a gage length of 60 mm, and were 3mm wide. The tests were carried out under six different testing temperatures (25, 50, 75, 100, 125, and 150 °C) with three different strain rates (0.001, 0.0001, and 0.00001 sec^{-1}). The test matrix is shown in Table 3.1. Each specimen was kept in the environmental chamber with the desired stable ambient

temperature for 5 minutes before the load was applied, and at least five specimens were tested for any given set of conditions. The testing temperatures covered the entire range from below the T_g to well above T_g.

3.3 Tensile Testing Data and Empirical Model

Figure 3.1 shows a typical stress-strain curve for the underfill UF1 at a temperature T = 100 °C, and a strain rate of $\dot{\varepsilon} = 1 \times 10^{-3}$ sec^{-1}. The effective elastic modulus E is defined as the slope of the initial linear portion of the stress-strain curve. Since the underfill material is viscoelastic, this effective modulus is rate dependent and will approach the true elastic modulus as the testing strain rate approaches infinity. The ultimate tensile strength σ_f (UTS) is the stress level at failure (fracture). The ultimate failure strain ε_f (elongation) is the maximum strain realized in the stress-strain test data, at which point the specimen fractures.

Since a minimum of five specimens were tested for any given condition, an empirical three-parameter hyperbolic tangent model was used to model the observed nonlinear underfill stress-strain data. The general representation of the hyperbolic tangent empirical relation is

$$\sigma(\varepsilon) = C_1 \tanh(C_2\varepsilon) + C_3\varepsilon \tag{3.5}$$

where C_1, C_2, and C_3 are material constants. Differentiation of equation (3.4) gives an expression for the initial (zero strain) elastic modulus:

$$E = C_1C_2 + C_3 \tag{3.6}$$

Constant C_3 represents the limiting slope of the stress-strain curve at high strains. The constants C_1, C_2 and C_3 can be determined by performing a nonlinear regression analysis of equation (3.5)to a given set of experimental data.

Strain Rate (1/s)	Testing Temperature					
	25° C	50° C	75° C	100° C	125° C	150° C
0.001	*	*	*	*	*	*
0.0001	*	*	*	*	*	*
0.00001	*	*	*	*	*	*

Table 3.1 - Table of Sample Test Temperatures and Strain Rates

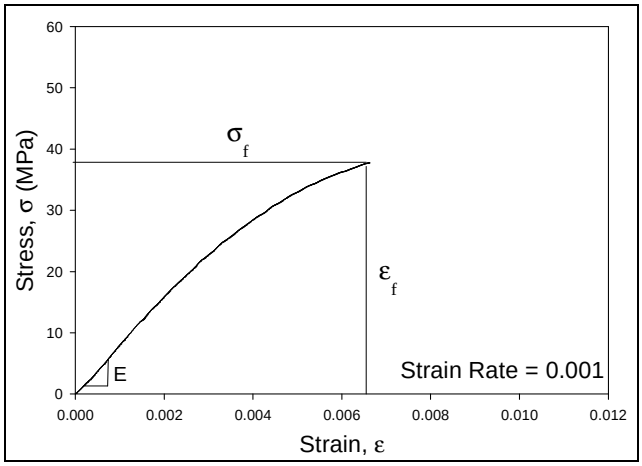

Figure 3.1 - A Typical Temperature Dependent Underfill Stress-Strain Curve
(T = 100 °C, and $\dot{\varepsilon}$ = 1 x 10^{-3} sec^{-1})

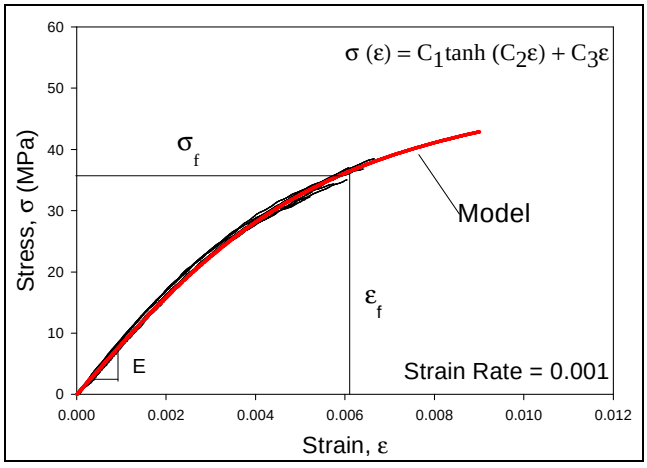

Figure 3.2 - Hyperbolic Tangent Model Fit to Underfill Stress-Strain Curves
(T = 100 °C, and $\dot{\varepsilon}$ = 1 x 10^{-3} sec^{-1})

Applying this empirical approach, Figure 3.2 shows the associated hyperbolic tangent model fit for all of the raw stress-strain data for non-aged specimens that were tested at T = 100 °C. At least 5 tests were performed for each set of conditions in this work. The observed variation in the data between different tests under the same condition is typical for cured polymeric materials. The hyperbolic tangent model fit (red curve) provides an excellent representation of the data that lies in the middle of all of the experimental curves.

Similar results were recorded for the different temperatures and strain rates considered. In each case, the hyperbolic tangent empirical model was used to produce a mathematical description of the "average" stress-strain curve for a set of experimental curves measured under a fixed set of test conditions. All of the data presented in this dissertation were processed in this manner. In each case, from 6-10 experimental stress-strain curves were initially measured, and then fit by an "average" stress-strain curve that mathematically represented the entire data set. From this point on, for clarity and simplification, only the hyperbolic tangent empirical fitting curves are presented.

3.4 Experimental Results and Discussions

3.4.1 Stress-Strain Curves

The underfill encapsulant material exhibits significant viscoelastic behavior. Therefore, its stress-strain relationship greatly depends on the testing temperature and displacement strain rates. In order to compare and investigate the temperature effects on the tensile mechanical properties of the underfill, all of the stress-strain curves at a given strain rate were combined into a single graph as shown in Figure 3.3. At each strain rate, the underfill material became soft, with markedly reduced strength, as the testing temperature increased.

The curves in Figure 3.3 were re-organized into constant temperature plots as shown in Figure 3.4. At each temperature, the stress-strain curves shifted lower and to the right as the testing strain rate went down. Obviously, testing temperature and strain rate have a great influence on important underfill mechanical properties, such as elastic modulus, ultimate tensile strength, and elongation.

3.4.2 Elastic Modulus

The purpose of underfill material is to reduce stress between the die and substrate, so a relatively low elastic modulus is preferred in order to relieve the inelastic stress sustained by the solder joints. On the other hand, the material must be stiff and strong enough to maintain the shape and co-planarity of the package. From Figures 3.3 and 3.4, the elastic modulus decreases monotonically with increasing temperature and a slower strain rate. This variation is shown graphically in Figure 3.5.

The modulus decreases linearly with temperature when the temperature is below 100 °C, which is far below the published glass transition temperature (T_g = 137 °C), and the underfill remains in the glassy state. When the temperature rises from 100 °C to 150 °C, the elastic modulus drops dramatically indicating the glass transition region where rubbery behavior dominates. The temperature has a strong effect on the elastic modulus during the transition period from glassy state to rubbery state. The elastic modulus is very low at 150 °C (above T_g) due to the weak network bonding in the rubbery state. Note that at 125 °C the elastic modulus value at a strain rate of 0.001/s is much higher than for slower strain rates, which can be attributed to the fact that the strain rate of 0.001 sec^{-1} is much faster than the intrinsic regrouping speed of the molecular network in the rubbery state. The molecular chains have enough time to

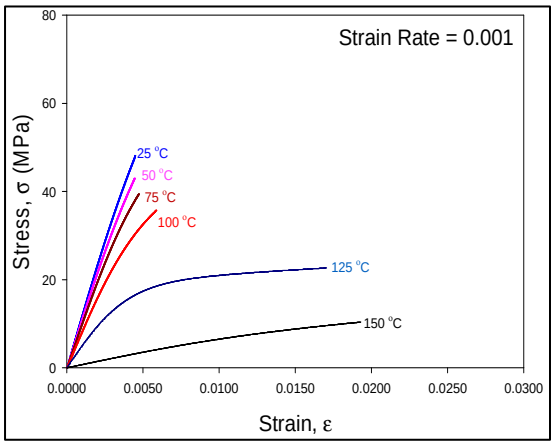

(a)

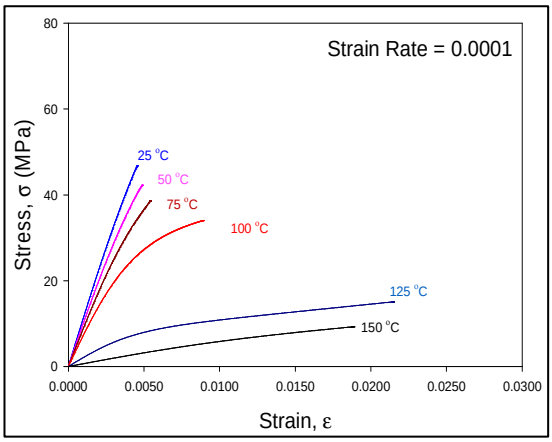

(b)

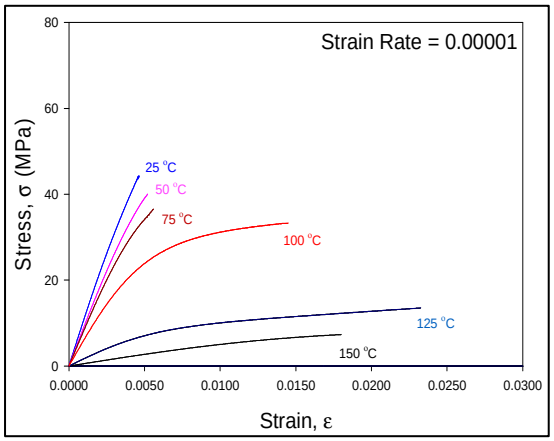

(c)

Figure 3.3 - Stress-Strain Curves for Different Temperatures at a Constant Strain Rate: (a) 0.001 (1/sec), (b) 0.0001 (1/sec), (c) 0.00001 (1/sec)

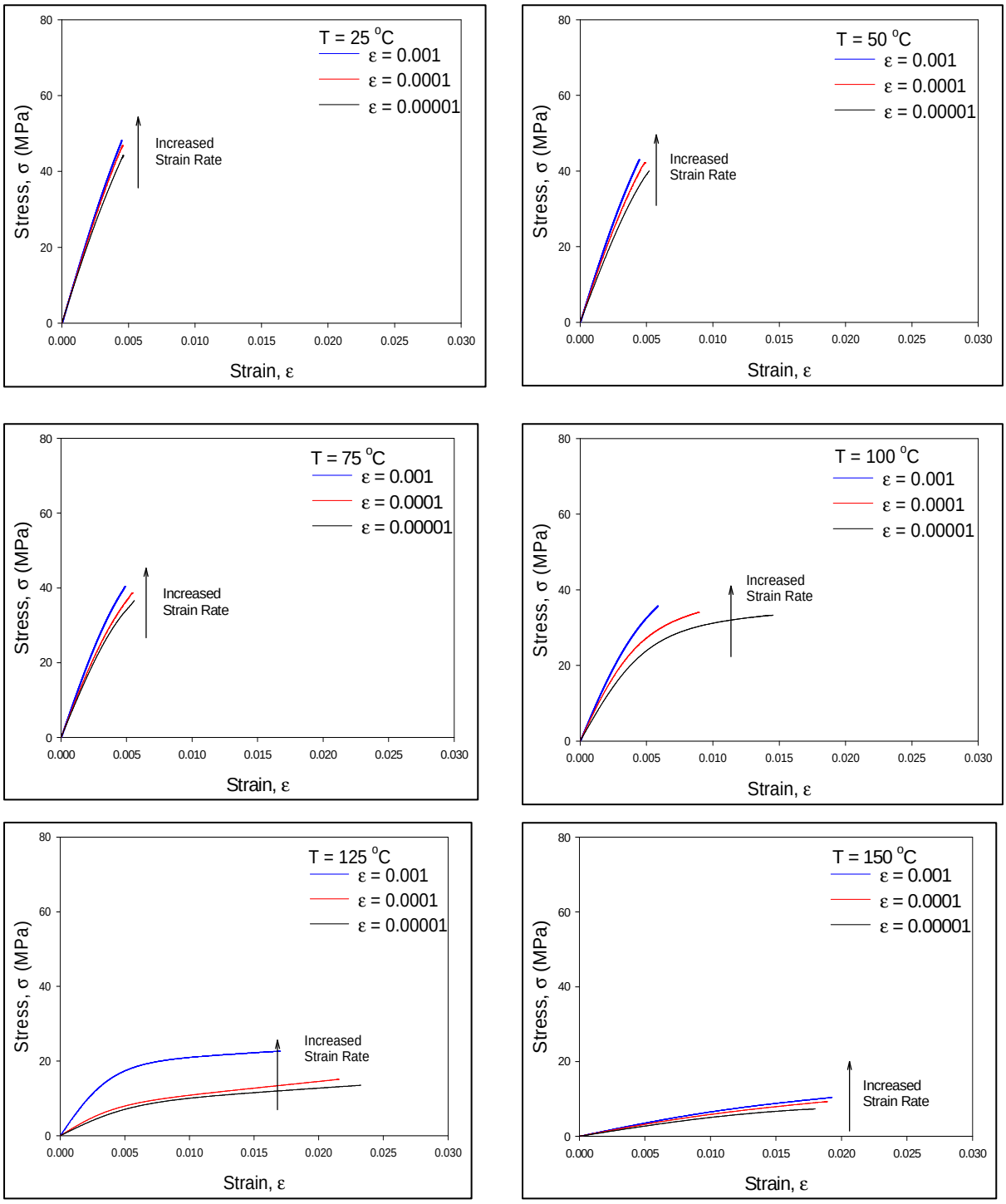

Figure 3.4 - Comparison of Stress-Strain Curves Tested at the Same Testing Temperature for Different Strain Rates

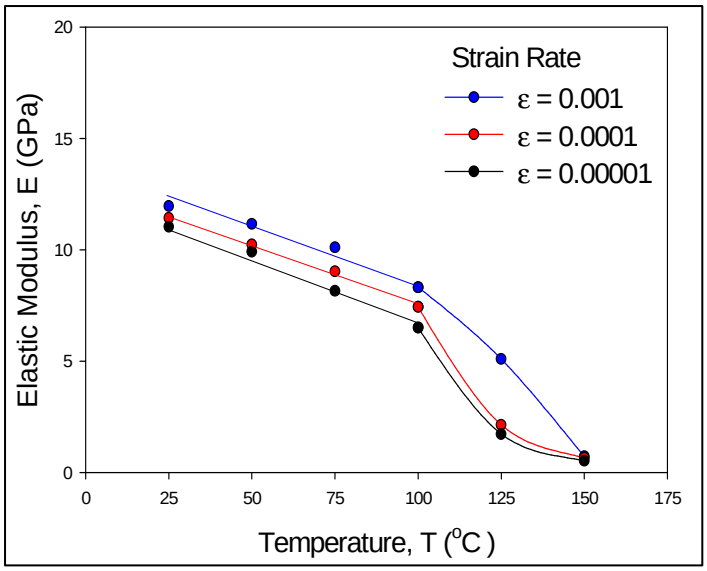

Figure 3.5 - Temperature Effects on the Underfill Elastic Modulus

slip, break and reconnect to each other under much slower strain rates, thus producing a much lower values of the elastic modulus.

The underfill material shows interesting behaviors during the transition from the glassy state to the rubbery state as the temperature increases through the T_g. For slow strain rates, the polymer molecules can break the existing cross-linked network and form a new structure when outside force is applied, and the local stress/strain can be released by the new orientated chain segment structure. However, if the strain rate is too high, the material has insufficient time for the segment to regroup and faults in the structure propagate, ultimately causing a fracture to occur.

3.4.3 Ultimate Tensile Strength

The effects of temperature on the ultimate tensile strength (UTS) of the underfill material are presented in Figure 3.6. The UTS decreases linearly with temperature relatively gently from 25 °C to 100 °C, but then sharply decreases in the temperature range from 100 °C to 150 °C. It is interesting to see that the temperature has similar effects on the elastic modulus and ultimate tensile strength. As it moves from the glassy to the rubbery state, the UTS decreases markedly because of the weaker molecular bonding forces. The discrepancy in the curve shape at 125 °C can be explained by the strain rate effect, as previously described.

3.4.4 Elongation

The effects of temperature and strain rate on the underfill elongation are shown in Figure 3.7. The specimen elongation (strain at failure) is calculated using:

$$e = \frac{L_f - L_0}{L_0} \times 100\% \tag{3.7}$$

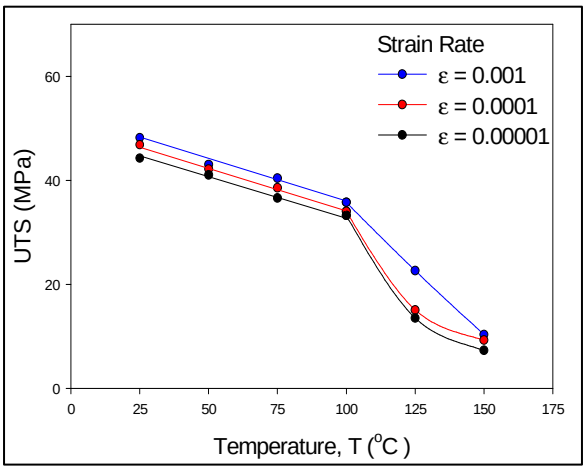

Figure 3.6 - Temperature Effects on the Underfill Ultimate Tensile Strength

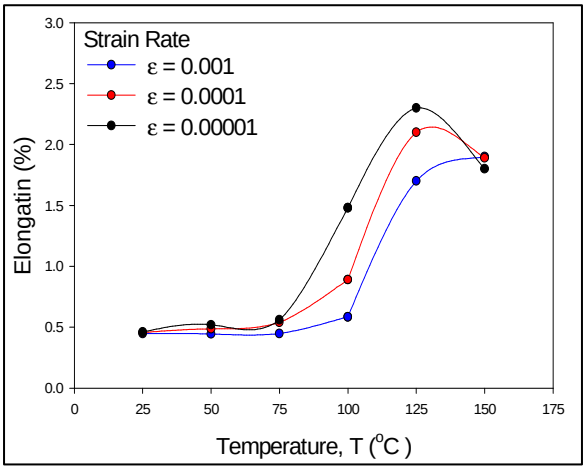

Figure 3.7 - Strain Rate Effects on the Underfill Elongation

where L_f is the final specimen gauge length at fracture, and L_0 is the original specimen length. The underfill elongation has a nonlinear relationship with temperature as shown in Figure 3.7. The elongation remains relatively constant or increases slightly below 75 °C for all strain rates. The underfill then becomes much softer as the temperature increases from 75 °C to 150 °C during the state phase transition, thus exhibiting greater extension ability. The strain rate also exhibits its strongest effect in this region, as at lower strain rates the material has enough time for the molecule-chain to slip and reform to achieve a longer extension before fracture.

The underfill material tested showed its largest elongation at 125 °C (close to the T_g), because at this point it is still strong enough for the cross-linked network structure to elongate without early fracture. This may explain the shorter extension of the specimen at 150 °C due to its much lower ultimate tensile strength in the rubbery state. Once the testing temperature exceeds the glass transition temperature, the strain rate has a weaker effect on the elongation because the material extends to its fullest extent in the rubbery state. Therefore, the curves for all three of the different strain rates shown in Figure 3.7 merge together at 150 °C.

3.5 Effects of Temperature and Strain Rate on Tensile Properties

The experimental values for the mechanical properties of the underfill material are summarized in Table 3.2. From the results, the properties are strongly strain rate dependent. Some authors [26, 30] have pointed out that the mechanical properties are linear with the logarithmic strain rate:

$$\sigma = \sigma_0 + c_1 \log \dot{\varepsilon} \tag{3.8}$$

Figure 3.8 illustrates the linear dependence of the elastic modulus on the logarithmic strain rate. The corresponding fitting constants are listed in Table 3.3. Only a weak strain rate effect was observed for the elastic modulus lower temperatures, but a significant effect was

observed at higher temperature levels near the T_g. The slope of the curve at 150 °C is smaller because the elastic modulus values are much smaller in the rubbery state. Similarly, the ultimate tensile strength shows a linear relationship to the logarithmic strain rate as shown in Figure 3.9. In both cases, the linear fits are poorest at T = 125 °C, which is very near the T_g.

Hertzberg [31] suggested a power law relation for material strength with strain rate:

$$UTS = C\dot{\varepsilon}^m \tag{3.9}$$

where m is the strain-rate sensitivity factor, or strain hardening exponent. An analogous relation can also be used for the elastic modulus. Table 3.4 contains the fitting constants for power law models used to fit the elastic modulus and UTS data in Figure 3.8 and 3.9. From the calculated R^2 values, it is clear that the power law also gives a good fit for all of the experiment data.

3.6 Simultaneous Modeling of the Effects of Strain Rate and Temperature

A number of researchers have provided constitutive models with both temperature and strain rate variables. For example, Qian [40] proposed the unified relation in equation (3.3) that included these two factors as independent variables, but the testing temperature range was far below the T_g. Although mechanical properties were easily fitted by this simple equation, it cannot be used for test temperatures that are near to or above T_g.

Pang, et al. [42] suggested empirical models for solder properties that took into account both factors:

$$E(T,\dot{\varepsilon}) = k_0 + (k_1 T + k_2)\log(\dot{\varepsilon}) + (k_3 T + k_4) \tag{3.10}$$

where k_0-k_4 are fitting constants, and

$$\sigma_{UTS}(T,\dot{\varepsilon}) = (C_0 + C_1 T)[\dot{\varepsilon}]^{(C_2 T + C_3)} \tag{3.11}$$

Testing Temperature (°C)	Strain Rate = 0.001			Strain Rate = 0.0001			Strain Rate = 0.00001		
	E (GPa)	UTS (MPa)	e	E (GPa)	UTS (MPa)	e	E (GPa)	UTS (MPa)	e
25	11.96	48.19	0.0045	11.43	46.84	0.0045	11.04	44.26	0.0046
50	11.17	43.03	0.0044	10.24	42.15	0.0048	9.92	41.02	0.0052
75	10.11	40.42	0.0045	9.03	38.56	0.0054	8.16	36.59	0.0056
100	8.32	35.77	0.0059	7.44	34.04	0.0089	6.51	33.26	0.0148
125	5.10	22.65	0.0170	2.14	15.08	0.0210	1.73	13.51	0.0230
150	0.73	10.35	0.0190	0.66	9.27	0.0189	0.53	7.31	0.0180

Table 3.2 - Mechanical Properties of Underfill Material at Different Strain Rates

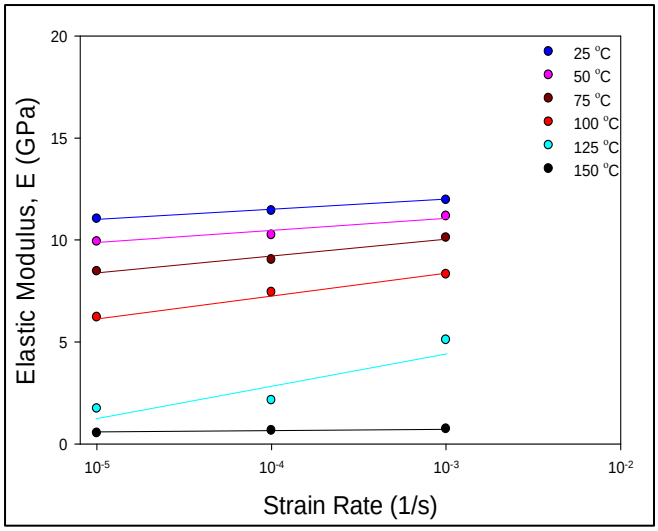

Figure 3.8 - Linear Dependence of the Elastic Modulus on the Logarithmic Strain Rate

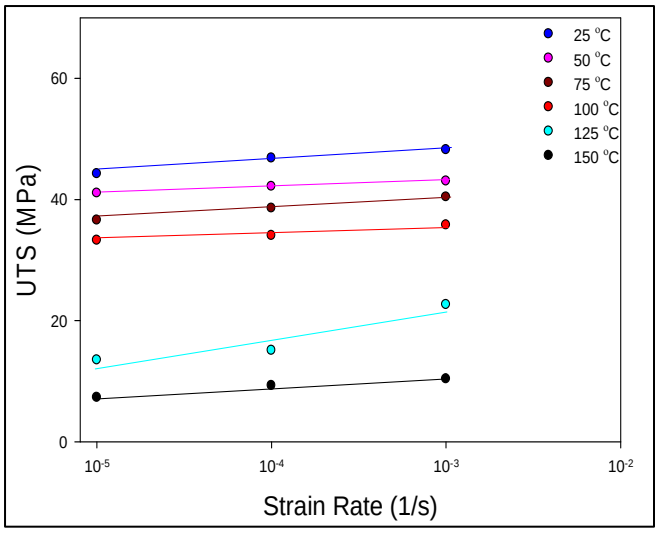

Figure 3.9 - Linear Dependence of the UTS on the Logarithmic Strain Rate

Temperature (°C)	Elastic Modulus		Strength	
	E (GPa)	R^2	UTS (MPa)	R^2
25 °C	$13.3 + 0.46\log(\dot{\varepsilon})$	0.992	$54.3+1.96\log(\dot{\varepsilon})$	0.968
50 °C	$12.94 + 0.63\log(\dot{\varepsilon})$	0.926	$46.19+1.0\log(\dot{\varepsilon})$	0.995
75 °C	$13.0 + 0.97\log(\dot{\varepsilon})$	0.996	$46.18+1.92\log(\dot{\varepsilon})$	0.999
100 °C	$11.0 + 0.91\log(\dot{\varepsilon})$	0.999	$39.38+1.26\log(\dot{\varepsilon})$	0.954
125 °C	$9.73 + 168\log(\dot{\varepsilon})$	0.839	$35.36+4.57\log(\dot{\varepsilon})$	0.874
150 °C	$1.04 + 0.1\log(\dot{\varepsilon})$	0.971	$15.1+1.52\log(\dot{\varepsilon})$	0.972

Table 3.3 - Logarithmic Model Fitting Constants

Temperature (°C)	Elastic Modulus		Strength	
	E (GPa)	R^2	UTS (MPa)	R^2
25 °C	$13.80(\dot{\varepsilon})^{0.0175}$	0.994	$54.95(\dot{\varepsilon})^{0.0185}$	0.964
50 °C	$13.71(\dot{\varepsilon})^{0.0258}$	0.993	$47.86(\dot{\varepsilon})^{0.0100}$	0.994
75 °C	$13.27(\dot{\varepsilon})^{0.0465}$	0.999	$46.99(\dot{\varepsilon})^{0.0216}$	0.999
100 °C	$12.07(\dot{\varepsilon})^{0.0533}$	0.997	$39.81(\dot{\varepsilon})^{0.0158}$	0.958
125 °C	$23.12(\dot{\varepsilon})^{0.235}$	0.901	$46.77(\dot{\varepsilon})^{0.112}$	0.905
150 °C	$1.21(\dot{\varepsilon})^{0.0695}$	0.957	$17.78(\dot{\varepsilon})^{0.075}$	0.975

Table 3.4 - Power Law Model Fitting Constants

where C_1-C_3 are fitting constants. Both of these models consider the effects of temperature and strain rate in a coupled manner. For underfill materials, however, the elastic modulus and ultimate tensile strength cannot be easily determined considering only a linear temperature dependence. Therefore, two modified empirical models are proposed for use with underfill materials:

$$E = K_1 + K_2 T + K_3 T^2 + (K_4 T + K_5)\log(\dot{\varepsilon}) \tag{3.12}$$

$$UTS = (C_1 + C_2 T + C_3 T^2)\dot{\varepsilon}^{(C_4 T + C_5)} \tag{3.13}$$

where K_1 through K_5 and C_1 through C_5 are fitting constants. Figures 3.10-3.11 illustrate the regression fits of equation 3.12 and 3.13 to the elastic modulus and UTS data collected in the present study. Very good representatives were obtained. The fitting parameters are listed in Table 3.5.

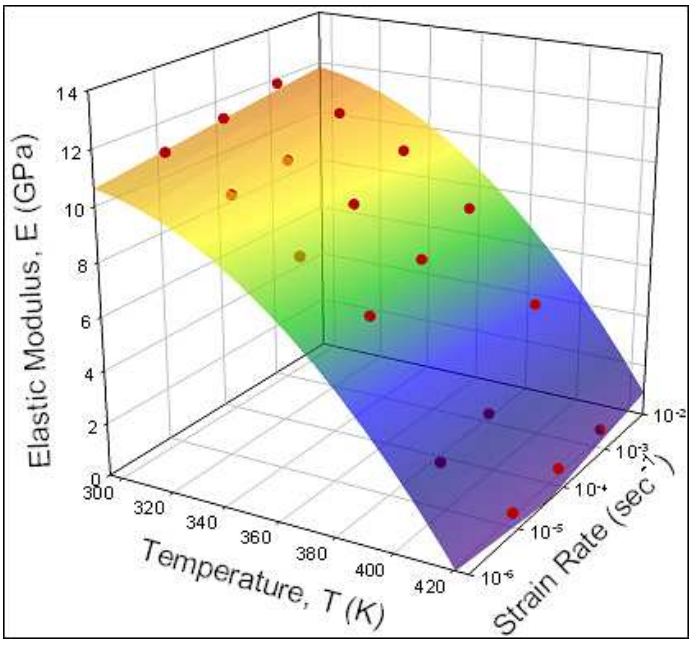

Figure 3.10 - Strain Rate and Temperature Effects on the Elastic Modulus

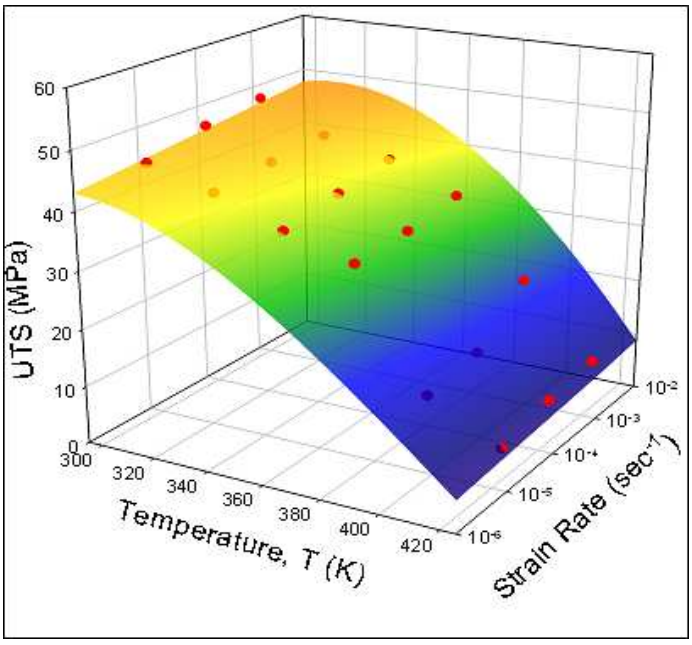

Figure 3.11 - Strain Rate and Temperature Effects on the UTS

K_1	K_2	K_3	K_4	K_5
-310	0.31	-0.00054	0.00065	0.11
C_1	C_2	C_3	C_4	C_5
-316.5	2.32	-0.0036	0.00028	0.07

* Note That E is in GPa, UTS in MPa, T in K, and $\dot{\varepsilon}$ in sec^{-1}

Table 3.5 - Fitting Constants for Empirical Models in Equations 3.12 and 3.13.

CHAPTER 4

EFFECTS OF AGING ON STRESS-STRAIN BEHAVIOR AND MECHANICAL PROPERTIES

4.1 Introduction

Microelectronic encapsulants exhibit evolving properties that change significantly with environmental exposures such as isothermal aging and thermal cycling. Such aging effects are exacerbated by the higher temperatures typical of thermal cycling qualification tests for harsh environment electronic packaging. The underfill material is normally based on epoxy resin, which displays the intermediate range of properties between an elastic solid and a viscous liquid depending on the temperature and the chosen time scale. The phenomenon of viscoelasticity is most obvious for amorphous polymers at temperatures near their T_g. In many applications, such as in automobile components, the normal operating range is from -40 to 125 °C. Aging effects are particularly important for components used in harsh environments such as ground and aerospace vehicles, where safety issues become paramount due to the need to ensure long term reliability.

Shi, et al. [28] and Kuo, et al. [29] have studied the effects of strain and temperature on the mechanical properties of typical epoxy underfills. In both investigations, the tests were conducted immediately following sample preparation, and did not consider possible aging effects.

There is significant literature available on the effects of isothermal aging on the mechanical behavior of polymers. Research in this area has been summarized in detail in the work of Struik [19, 21]. The main body of these studies covers glass-forming materials (polymers, inorganic glasses, etc.) that are briefly annealed at a temperature above their T_g and then rapidly cooled (quenched) to a temperature significantly below the T_g. After quenching, the material remains in a non-equilibrium thermodynamic state, from which its physical properties (mechanical, thermodynamic, etc.) shift slowly towards equilibrium. This process is often called physical aging, and the effects on the small strain (linear viscoelasticity) creep response of polymers have been extensively documented. Physical aging processes are thermo-reversible at high temperature.

In general, polymers subjected to thermal aging after quenching become stiffer and more brittle. Additionally their creep rate or compliance gradually decreases as the aging progresses. Recent studies on physical aging effects in epoxy without fillers have been performed by Lee and McKenna [23] and Miyano, et al. [43].

Most studies examining the physical aging of polymers involve brief exposures of test samples to temperatures above the T_g, with the observed aging then occurring at temperatures significantly below the T_g. The minimal exposures above the T_g are solely for the purpose of annealing or de-aging the samples. In many harsh environment applications of electronic packaging, the assemblies are subjected to temperatures at or above the T_g for extended periods, but there have been few studies on the effects of aging at such high temperatures on the mechanical behavior of polymers. Those that have been performed, on polystyrene [24] and PEEK [44] have noted new and unexpected types of behaviors after cooling. In addition,

elevated temperature aging leads to detrimental effects on the adhesion and interfacial failure properties of underfills, as well as to the drop test reliability of assemblies containing underfills.

4.2 Objectives and Testing Program

In this work, the changes occurring in the stress-strain behavior of flip chip underfill encapsulants were characterized for isothermal aging at four different temperatures: far below, below, near, and above its T_g. Samples were prepared and isothermally aged for up to 10 months at 80, 100, 125, and 150 °C as shown in Table 4.1. For this study, a group of non-aged samples were prepared, along with twenty groups of aged specimens consisting of combinations of five different aging times (10, 30, 100, 200 and 300 days) and four different aging temperatures (80, 100, 125 and 150 °C). Stress-strain tests were then performed on both the non-aged and aged samples at six different temperatures, from room temperature up to 150 °C (25, 50, 75, 100, 125, and 150 °C). For all tests, a 60 mm gage length was utilized between the specimen grips, and a strain rate of $\dot{\varepsilon}$ = .001 sec^{-1} was applied during the load application. The material properties were extracted from the measured stress-strain cruves and the effects of aging were determined and modeled.

4.3 Experimental Results and Discussion

4.3.1 Changes in Microstructure and Cure Properties

The material microstructure is often a the fundamental factor determining mechanical properties. The first step was therefore to look for any changes in the material microstructure after the isothermal aging exposure. Figure 4.1 shows SEM images of the material microstructure for a sample with no aging and for a sample that was aged at 150 °C for 300 days

Aging Temperature.	0 Day	10 Days	30 Days	100 Days	200 Days	300 Days
80 °C	*	*	*	*	*	*
100 °C		*	*	*	*	*
125 °C		*	*	*	*	*
150 °C		*	*	*	*	*

Table 4.1 - Test Matrix for Tensile Test Sample Aging Exposures

(the highest curing temperature and the longest curing time). These images reveal that the effect of aging on the microstructure is not profound for this underfill material, with very little difference visible between the two samples. The same non-uniform structure is clearly present in each specimen, with the larger silica particles settling to the bottom and a thin layer of pure epoxy on the top surface.

Epoxy is a thermosetting resin and is subject to cure kinetics, so that both temperature and time influence the completion of the thermosetting resin cure. The material decomposition temperature for the underfill in this study was determined to be 330 °C using thermogravimetric analysis (TGA). Differential scanning calorimetry (DSC) tests were then performed from 0 °C to 250 °C at a rate of 10 °C/m on samples with various amounts of aging. Example heat flow plots are shown in Figure 4.2 for samples aged at 80 °C for 10 days (light aging) and at 150 °C for 300 days (heavy aging). From the plots, the glass transition temperature was 133.9 °C for the lightly aged specimen and 136.1 °C for the heavily aged specimen. Thus the T_g has increased over 2 °C due to the additional aging. In addition, the residual cure energy of the first sample was 1.436 J/g, which was almost double the value of 0.785 J/g for the more heavily aged sample. Clearly, aging has a noticeable effect on the glass transition behavior (temperature dependent mechanical properties) and degree of curing for the underfill material.

4.3.2 Stress-Strain Data for Non-Aged Samples

Figure 4.3 illustrates typical stress-strain curves for non-aged tested underfill samples at temperatures from T = -175 °C to T = +150 °C. The effective elastic modulus E is defined as the slope of the initial linear portion of the stress-strain curves. The plot of elastic modulus vs. temperature (with each data point representing the average of 5 to 10 tests) is shown in Figure

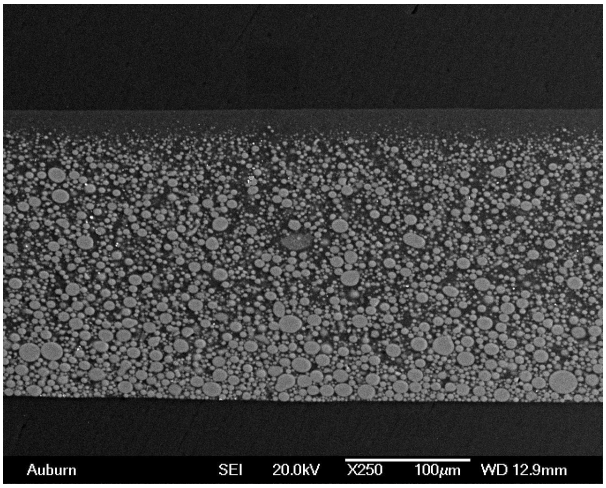

(a) Non-Aged Specimen

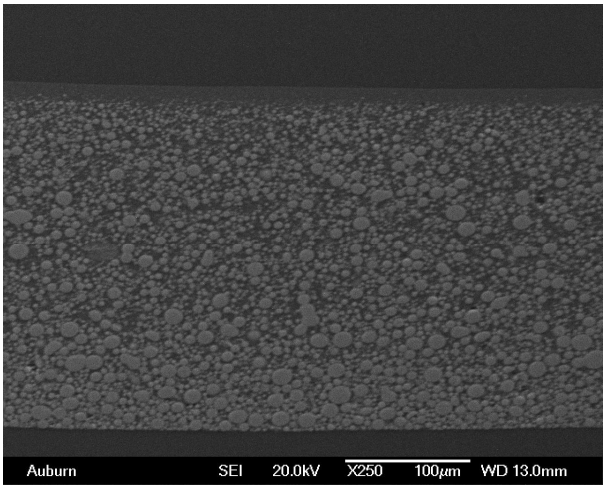

(b) Specimen Aged at 150 °C for 300 Days

Figure 4.1 - Aging Effects on Underfill Microstructure

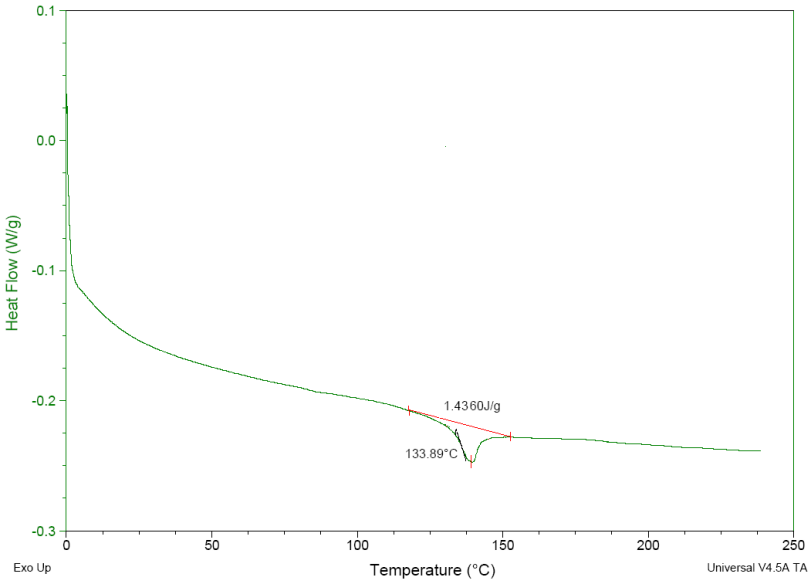

(a) Aged at 80 °C for 10 Days

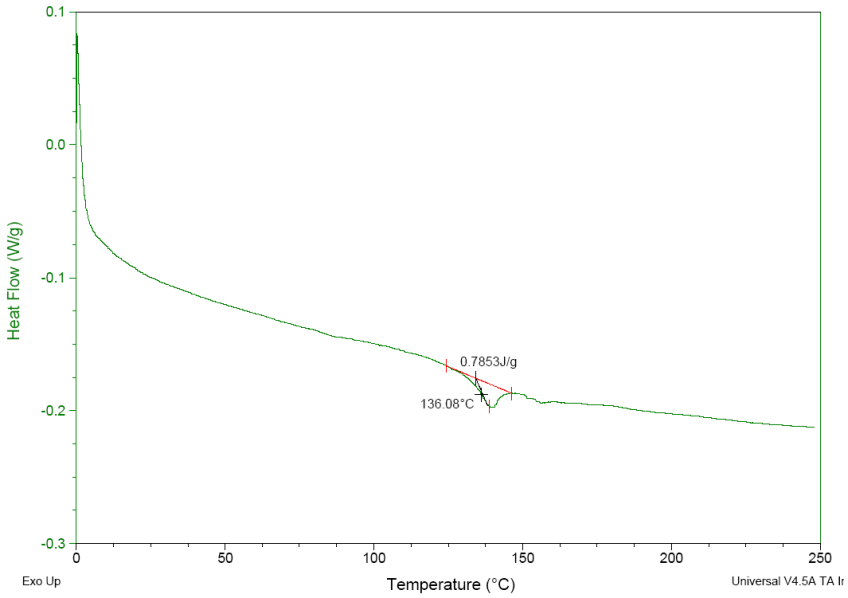

(b) Aged at 150 °C for 300 Days

Figure 4.2 - Aging Effects on Underfill Thermal Properties

4.4. The glass transition region for T > +100 °C is clearly evident in the plot, while the vendor datasheet value is 137 °C.

At this point, the effects of isothermal aging on the stress-strain curves from 25 °C (room temperature) up to 150 °C (the curing temperature of the underfill) will be explored by using the test matrix in Table 4.1. Figure 4.5 shows the average stress-strain curves (empirical model fits) for non-aged samples tested at T = 25, 50, 75, 100, 125, and 150 °C. As discussed previously, each of these curves are a fit of equation (3.5) to the 5-10 experimental stress-strain curves recorded for a given set of conditions. These curves for non-aged samples will provide the baselines for evaluating the changes occurring due to aging.

4.3.3 Stress-Strain Data for Aged Samples

The effects of elevated temperature isothermal aging at 80, 100, 125 and 150 °C on the underfill stress-strain curves and mechanical properties were explored in this study. These particular aging temperatures were chosen since they conform to temperatures below the T_g (80 and 100 °C), near the T_g (125 °C), and above the T_g (150 °C) of the underfill material.

For each set of aging conditions in Table 4.1, at least 60 samples were subjected to tensile testing. On removal from the oven, these samples were allow to cool to room temperature (T = 25 °C) over a period of 24 hours. This cooling period was kept short to avoid introducing additional physical aging effects as described by Struik [21]. After cooling, ten specimens were tested at each of six different temperatures (T = 25, 50, 75, 100, 125 and 150 °C). The raw data from each set of aging conditions and testing temperature were fit with the hyperbolic tangent empirical model to generate an average stress-strain curve representation for each set of aging and temperature conditions. For example, the average temperature dependent stress-strain curves for 10, 30, 100, 200, 300 days of aging at 100 °C are shown in Figure 4.6.

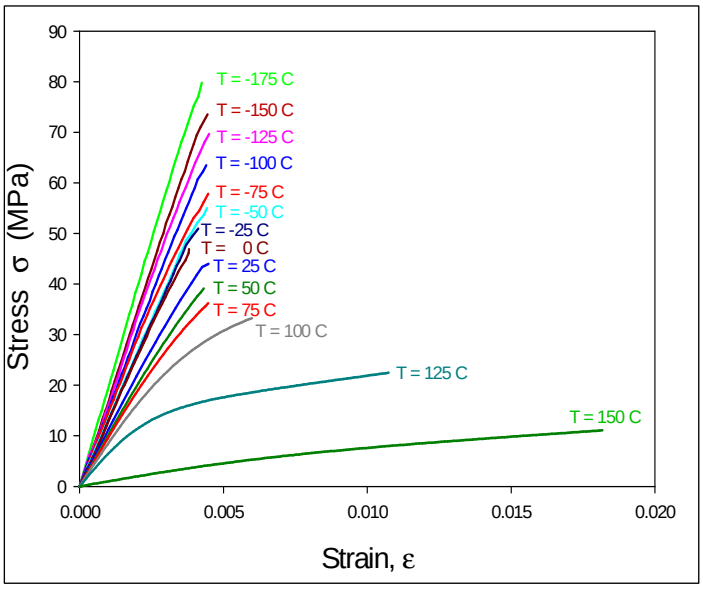

Figure 4.3 - Typical Temperature Dependent Underfill Stress-Strain Curves (No Aging)

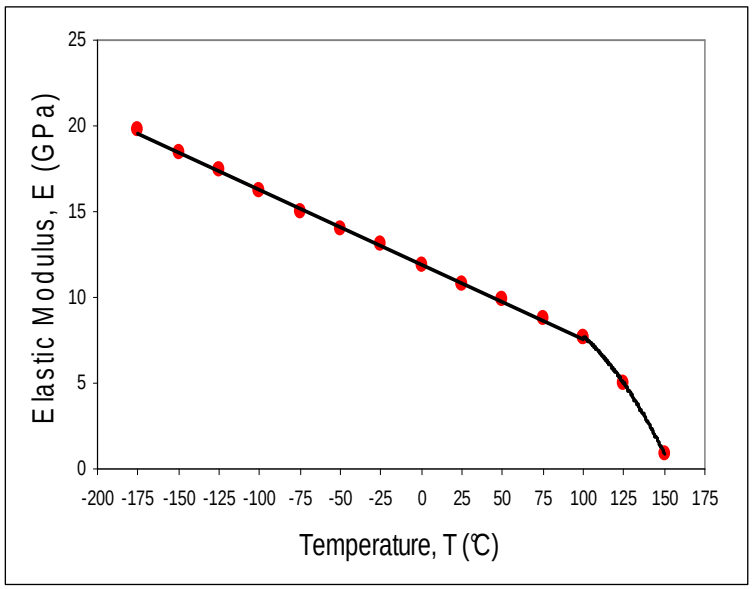

Figure 4.4 - Underfill Effective Elastic Modulus vs. Temperature

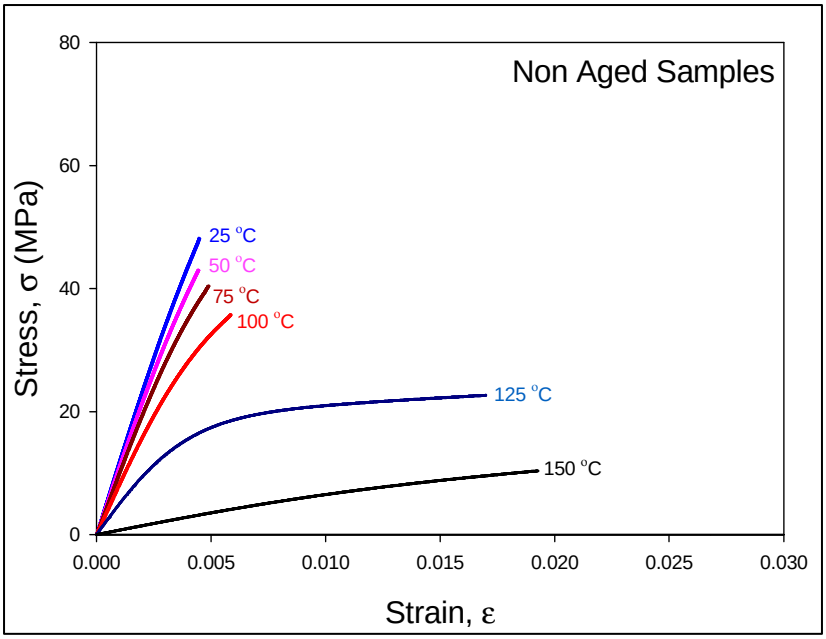

Figure 4.5 - Average Stress-Strain Curves (No Aging)

4.3.4 Aging Time Effects and Comparisons

The effects of isothermal aging are not immediately visible from a casual comparison of the curves in Figures 4.5 for the non-aged specimens with the curves in Figures 4.6 for the aged specimens. Consequently, direct comparisons of the curves at each temperature for aged and non-aged samples are given in Figure 4.7. The results in Figures 4.6 and 4.7 are for samples aged at 100 °C. Analogous measurements have been made for samples aged at the three other temperatures. Results for aging at 80 °C are shown in Figures 4.8 and 4.9. Results for aging at 100 °C are shown in Figure 4.10 and 4.11. Finally, results for aging at 150 °C are shown in Figures 4.12 and 4.13.

The effects of aging can be easily determined from the plots in Figures 4.7, 4.9, 4.11, and 4.13. The increase in modulus (initial slope) and ultimate tensile strength (failure stress) with aging are easily visualized in these figures. To investigate in more detail, the curves in Figure 4.7 for aging at 100 °C will be discussed. Although the initial linear behavior of the average stress-strain curves appears to be only slightly affected at each temperature, the ultimate tensile strength undergoes some notable changes with aging time. This effect is especially noticeable at T = 100 °C and T = 125 °C. The material properties have been extracted from the average stress-strain curves. Plots of the variation of the effective modulus E and UTS with temperature for various aging times are shown in Figure 4.14. The variation with temperature has been modeled as linearly decreasing up to 100 °C, and as a polynomial for higher temperatures. In general, the changes (increases) in E and UTS with aging were typically in the range of 10-50% of the non-aged values. For example, with 300 days aging, the effective modulus at 125 °C increased by 31%, from 5.1 GPa to 6.7 GPa, and the ultimate tensile strength at 125 °C increased 45%, from 22.65 MPa to 32.95 MPa.

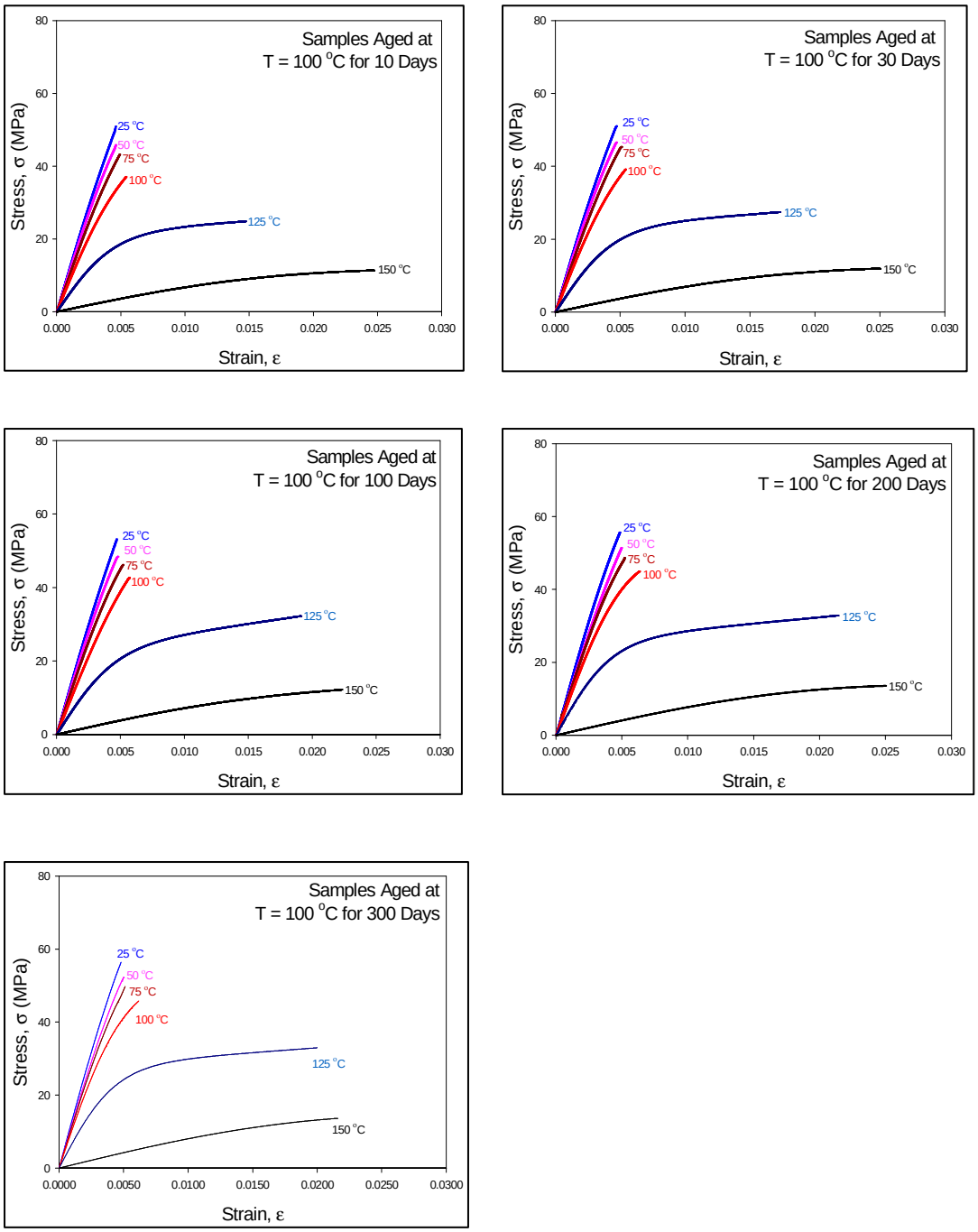

Figure 4.6 - Stress-Strain Curves for Specimens Aged at 100 °C for 10, 30 100, 200 and 300 Days

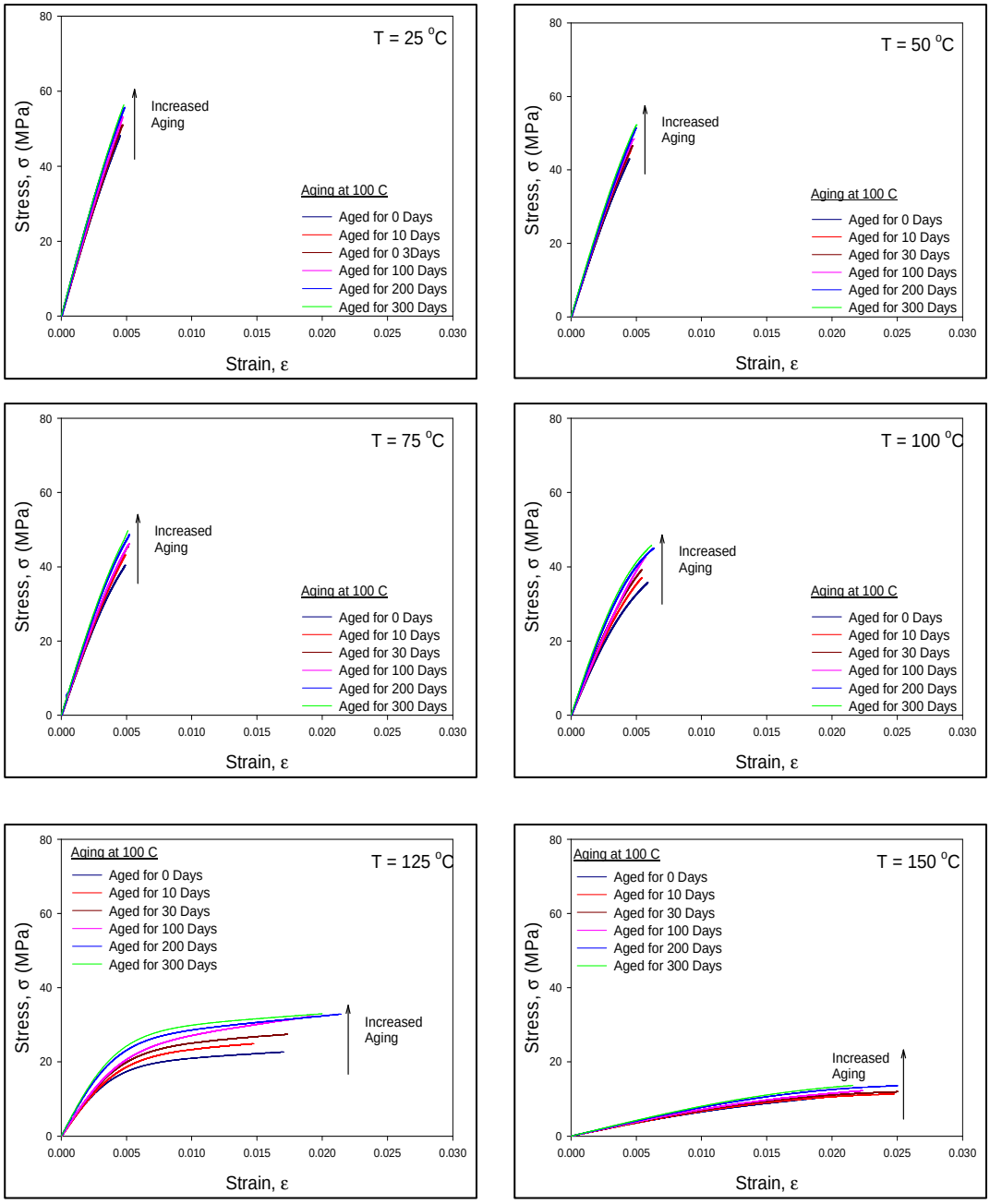

Figure 4.7 - Stress-Strain Curves for Specimens Aged at 100 °C
(T = 25, 50, 75, 100, 125 and 150 °C)

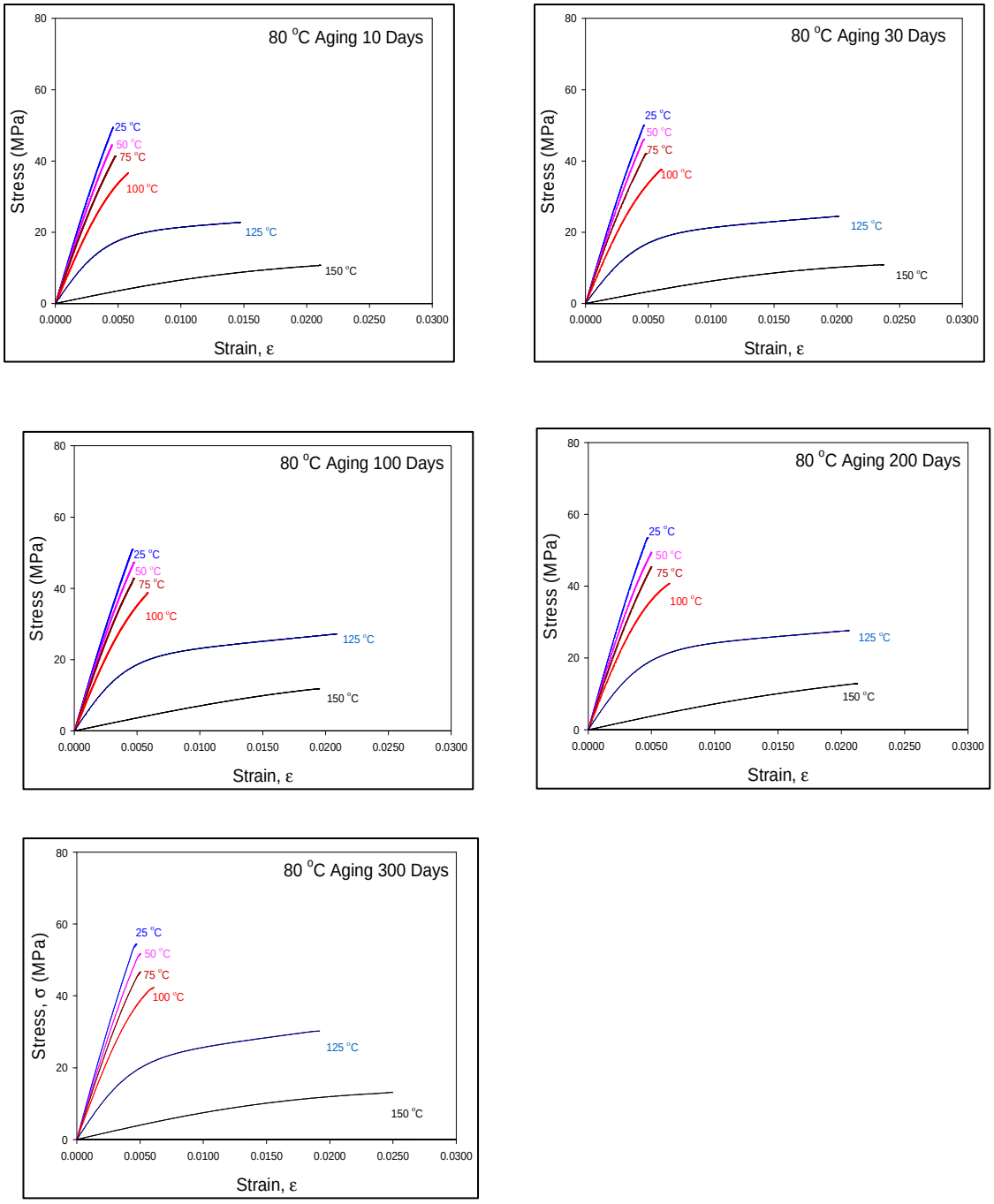

Figure 4.8 - Stress-Strain Curves for Specimens Aged at 80 °C for 10, 30 100, 200 and 300 Days

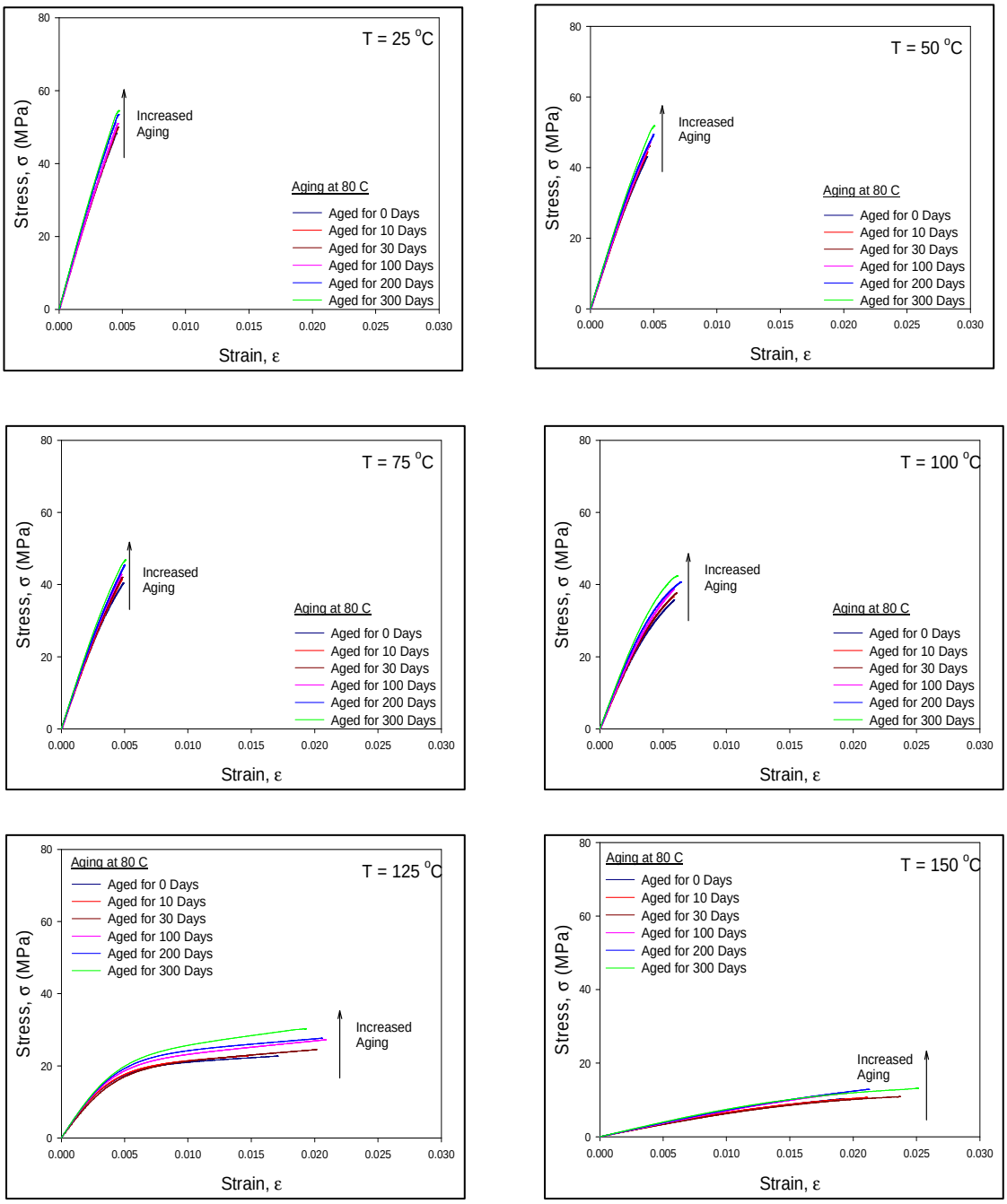

Figure 4.9 - Stress-Strain Curves for Specimens Aged at 80 °C
(T = 25, 50, 75, 100, 125 and 150 °C)

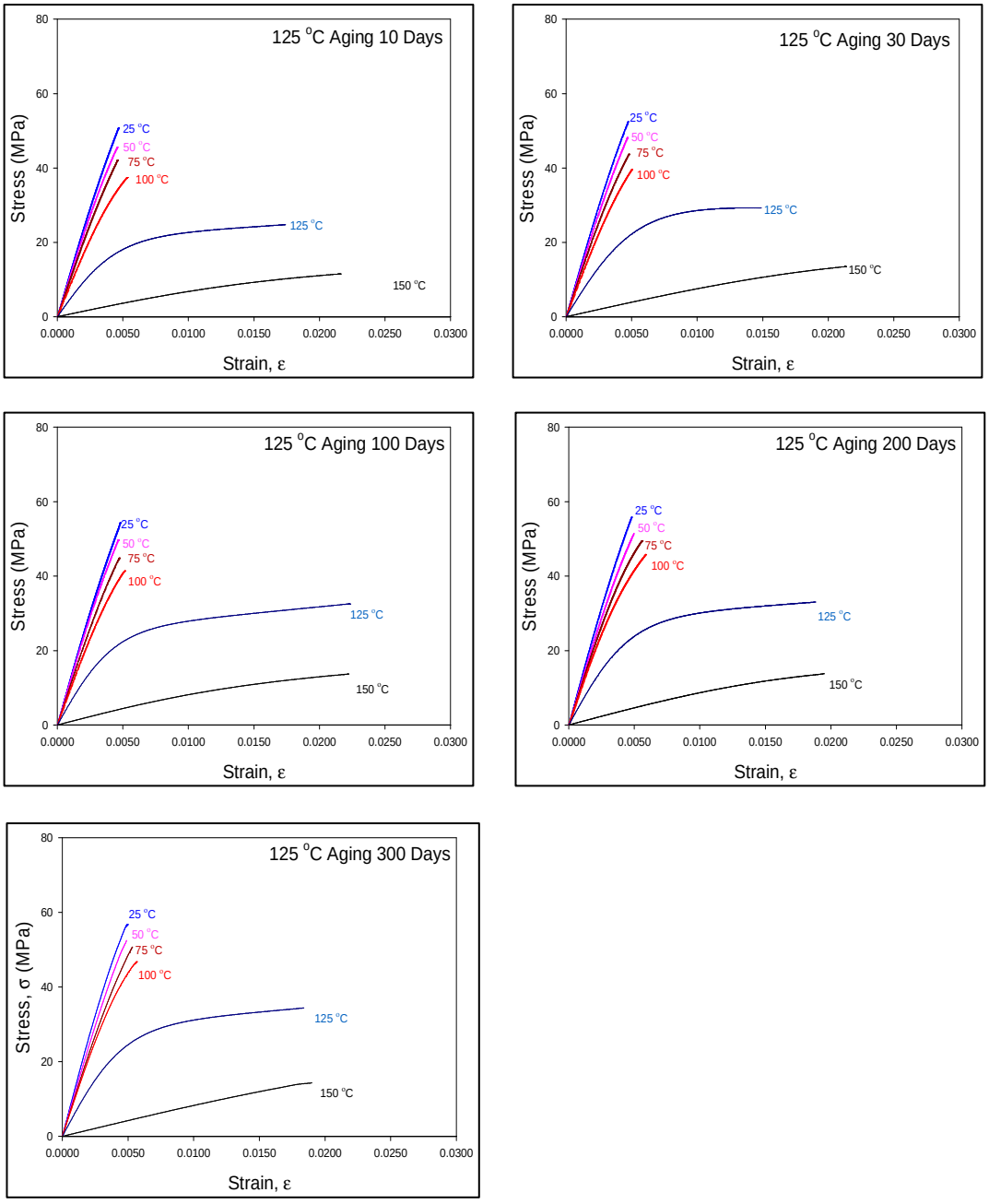

Figure 4.10 - Stress-Strain Curves for Specimens Aged at 125 °C for 10, 30 100, 200 and 300 Days

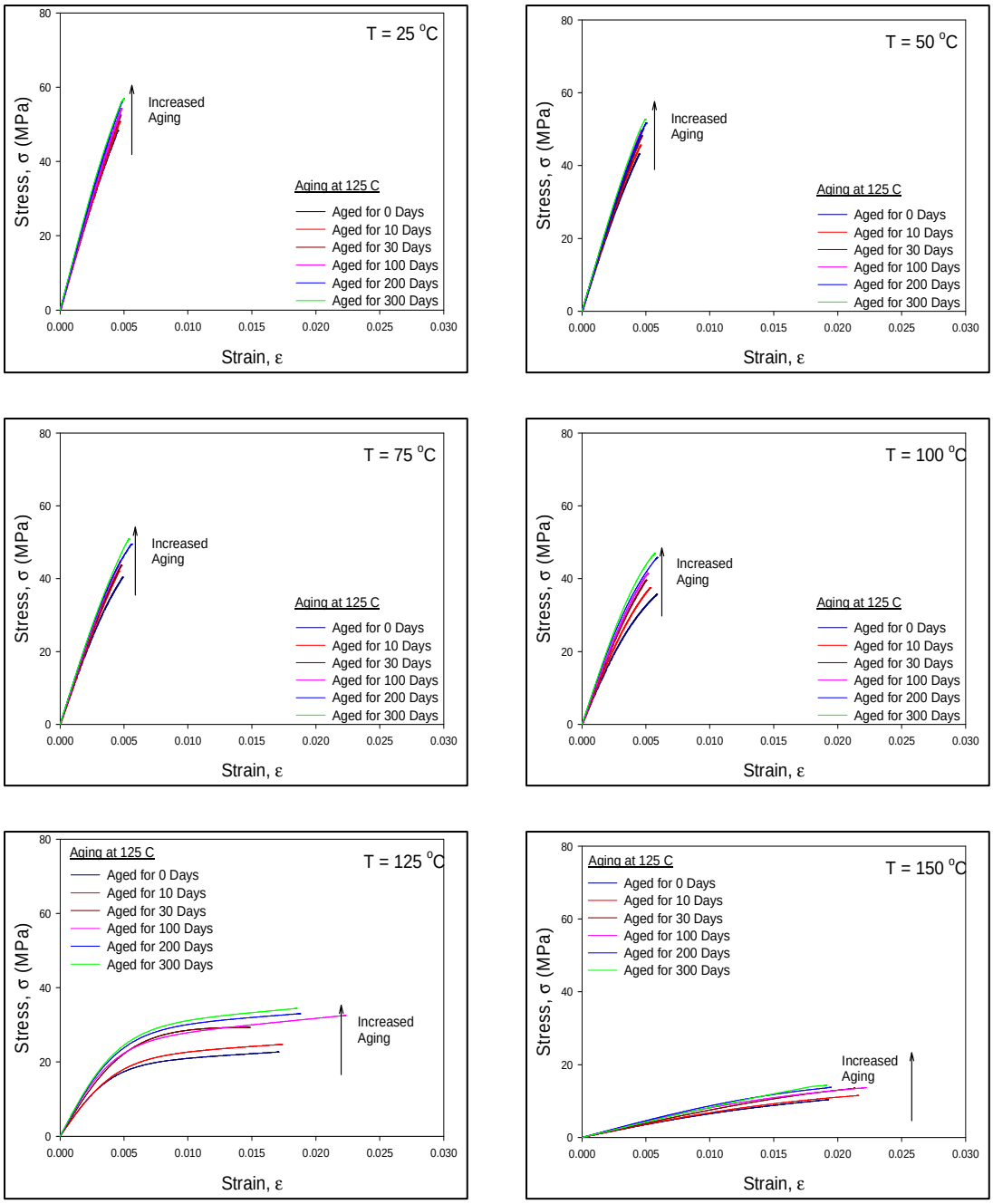

Figure 4.11 - Stress-Strain Curves for Specimens Aged at 125 °C
(T = 25, 50, 75, 100, 125 and 150 °C)

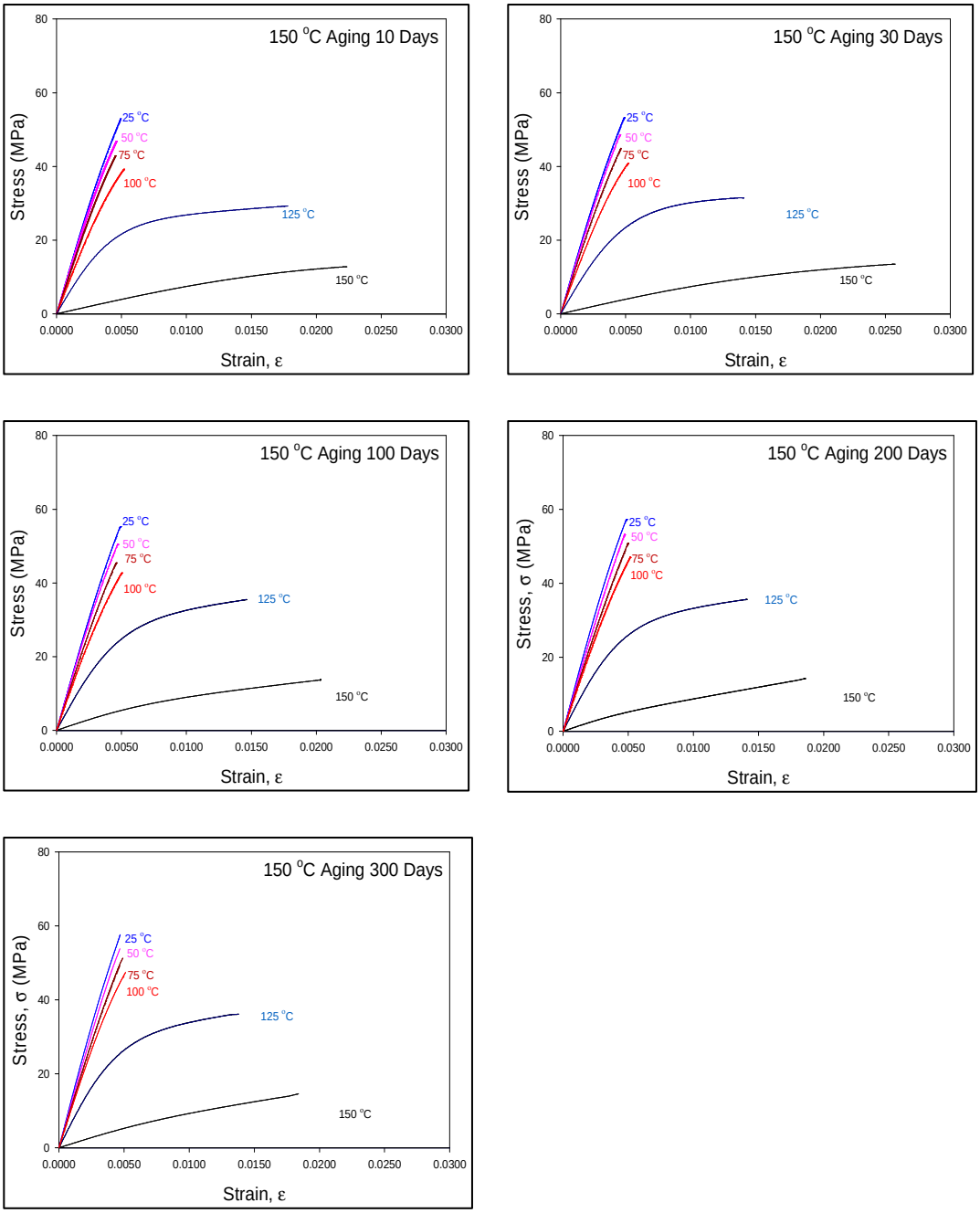

Figure 4.12 - Stress-Strain Curves for Specimens Aged at 150 °C for 10, 30 100, 200 and 300 Days

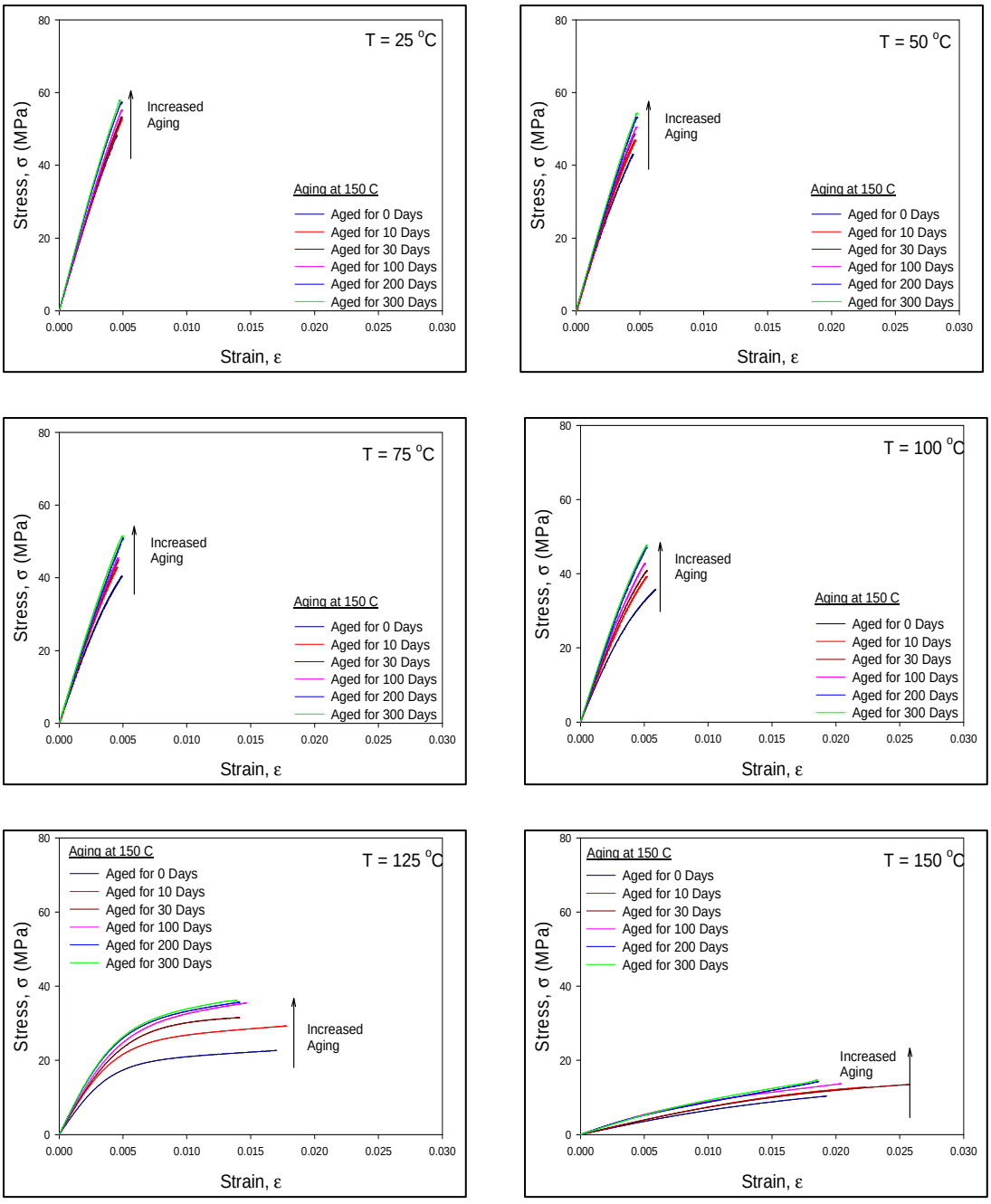

Figure 4.13 - Stress-Strain Curves for Specimens Aged at 150 °C
(T = 25, 50, 75, 100, 125 and 150 °C)

Similar data were obtained for all combinations of aging temperature and test temperature. These trends are illustrated in the plots of effective modulus E and ultimate tensile strength (UTS) versus temperature in Figures 4.14 to 4.17 for the four different aging temperatures. In general, the changes (increases) were typically in the range of 10-30% for E and 10-50% for UTS relative to the non-aged values. However, these were only slight variations in the shape of the stress-strain curves due to the aging effect. Detailed values for the mechanical properties of the underfill material with different aging temperatures/times and testing temperatures are provided in Tables 4.2 to 4.5.

4.3.5 Aging Temperature Effects and Comparisons

The underfill material samples were aged at four different isothermal aging temperatures. By regrouping the data in Figure 4.14-4.17, it was possible to examine the effect of different aging temperatures on the elastic modulus and ultimate tensile strength. Figures 4.18-4.22 illustrate the variation of the mechanical properties with temperature for different aging temperatures. In these figures, all plots on each graph have the same aging time. The largest relative changes occur in Figure 4.22 (300 days aging).

4.3.6 Property Evolution with Aging Time

In order to examine the mechanical property evolution with aging time more closely, the data were plotted again with aging time on the horizontal axis. For example, Figure 4.23 shows the variation of the UTS data with aging time for specimens aged at 100 °C. In this plot, each curve represents a different testing temperature. These variations can be modeled well using a four parameter empirical models with linear and exponential terms:

$$UTS = C_0 + C_1 t_{ag} + C_2 \left(1 - e^{-C_3 t_{ag}}\right) \tag{4.1}$$

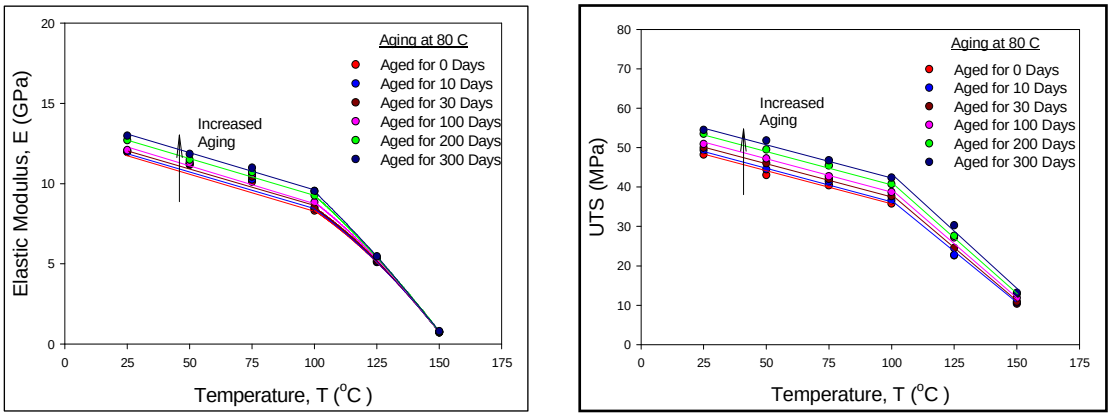

Figure 4.14 - Effective Elastic Modulus and UTS vs. Temperature for Aging at 80 °C

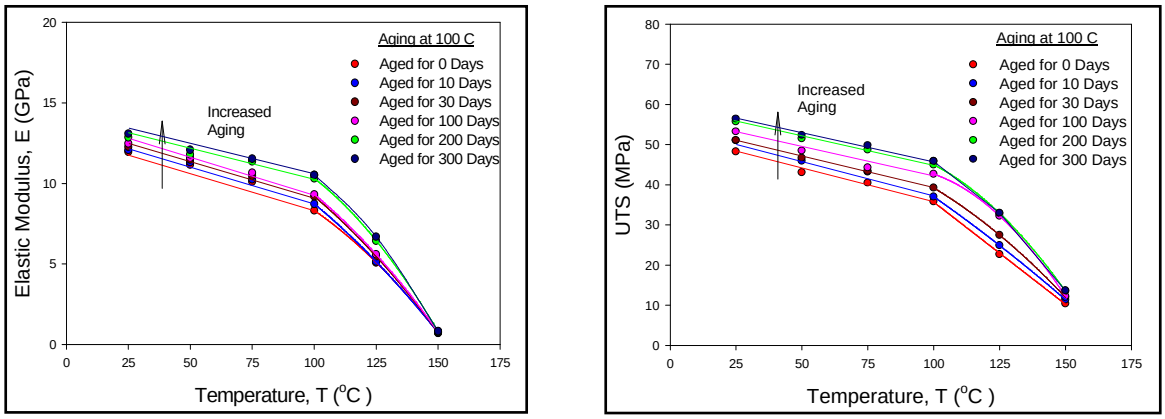

Figure 4.15 - Effective Elastic Modulus and UTS vs. Temperature for Aging at 100 °C

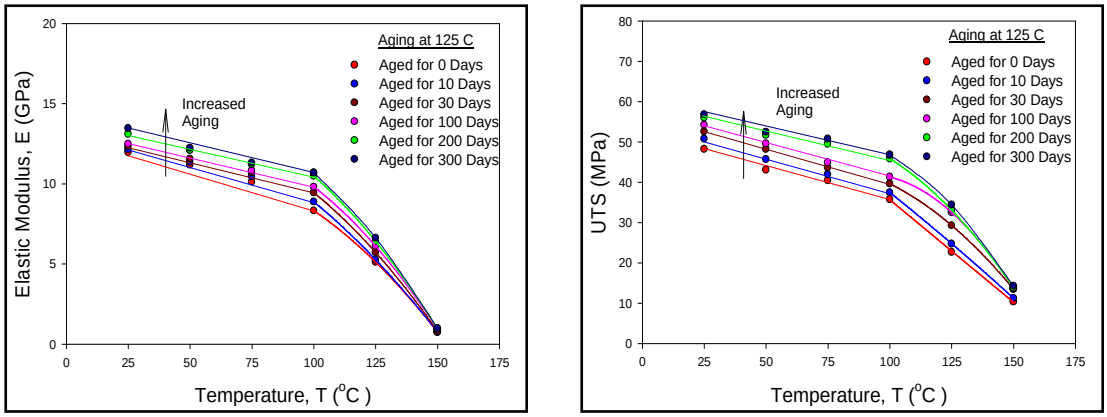

Figure 4.16 - Effective Elastic Modulus and UTS vs. Temperature for Aging at 125 °C

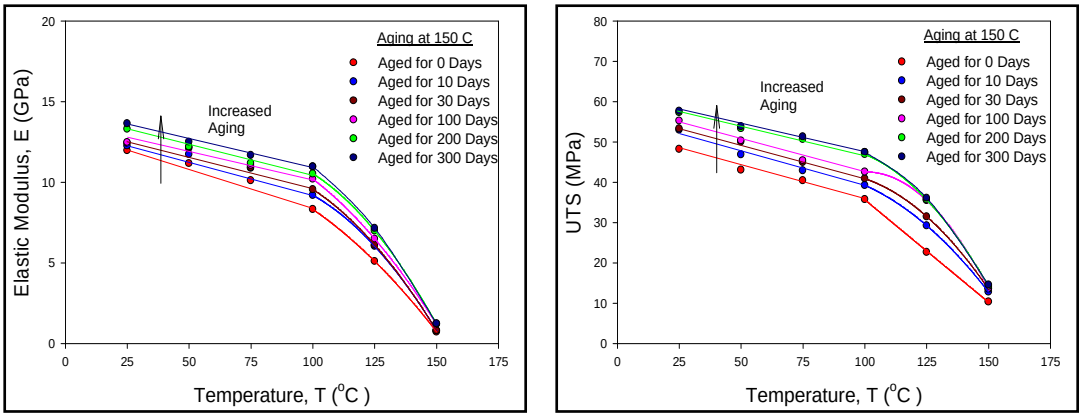

Figure 4.17 - Effective Elastic Modulus and UTS vs. Temperature for Aging at 150 °C

Test Temp. (°C)	No Aging		80 °C, 10 days		80 °C, 30 days		80 °C, 100 days		80 °C, 200 days		80 °C, 300 days	
	E (GPa)	UTS (MPa)	E (GPa)	UTS (MPa)	E (GPa)	UTS (MPa)	E (GPa)	UTS (MPa)	E (GPa)	UTS (MPa)	E (GPa)	UTS (MPa)
25	11.96	48.19	11.99	49.30	12.05	49.91	12.08	50.87	12.70	53.45	12.98	54.44
50	11.17	43.03	11.2	44.49	11.24	46.03	11.32	47.18	11.48	49.47	11.84	51.78
75	10.11	40.42	10.25	41.39	10.44	42.02	10.59	42.71	10.71	45.44	10.98	46.70
100	8.32	35.77	8.44	36.58	8.51	37.62	8.84	38.69	9.26	40.72	9.53	42.35
125	5.10	22.65	5.13	22.73	5.20	24.47	5.30	27.2	5.40	27.60	5.46	30.22
150	0.73	10.35	0.73	10.65	0.74	10.88	0.74	11.84	0.77	12.87	0.798	13.15

Table 4.2 - Elastic Modulus and Ultimate Strength vs. Temperature for Samples Aged at 80 °C

Test Temp. (°C)	No Aging		100 °C, 10 days		100 °C, 30 days		100 °C, 100 days		100 °C, 200 days		100 °C, 300 days	
	E (GPa)	UTS (MPa)	E (GPa)	UTS (MPa)	E (GPa)	UTS (MPa)	E (GPa)	UTS (MPa)	E (GPa)	UTS (MPa)	E (GPa)	UTS (MPa)
25	11.96	48.19	12.07	50.97	12.27	51.05	12.48	53.2	12.86	55.69	13.09	56.37
50	11.17	43.03	11.33	45.89	11.48	46.59	11.58	48.42	11.79	51.46	12.08	52.30
75	10.11	40.42	10.26	43.20	10.47	43.34	10.66	44.21	11.37	48.70	11.53	49.78
100	8.32	35.77	8.73	36.99	9.19	39.19	9.32	41.65	10.31	44.96	10.52	45.81
125	5.10	22.65	5.14	24.85	5.47	27.44	5.70	32.21	6.45	32.86	6.70	32.95
150	0.73	10.35	0.73	11.35	0.76	11.94	0.79	12.2	0.81	13.50	0.83	13.63

Table 4.3 - Elastic Modulus and Ultimate Strength vs. Temperature for Samples Aged at 100 °C

Test Temp. (°C)	No Aging		125 °C, 10 days		125 °C, 30 days		125 °C, 100 days		125 °C, 200 days		125 °C, 300 days	
	E (GPa)	UTS (MPa)	E (GPa)	UTS (MPa)	E (GPa)	UTS (MPa)	E (GPa)	UTS (MPa)	E (GPa)	UTS (MPa)	E (GPa)	UTS (MPa)
25	11.96	48.19	12.14	50.76	12.34	52.54	12.48	54.20	13.10	55.97	13.46	56.82
50	11.17	43.03	11.35	45.66	11.55	48.19	12.10	49.56	12.10	51.64	12.23	52.46
75	10.11	40.42	10.44	41.94	10.69	43.57	10.82	44.89	11.20	49.50	11.30	50.74
100	8.32	35.77	8.87	37.45	9.44	39.62	9.80	41.30	10.48	45.85	10.68	46.80
125	5.10	22.65	5.25	24.75	5.71	28.28	6.10	31.50	6.55	33.04	6.62	34.40
150	0.73	10.35	0.74	11.52	0.78	13.46	0.91	13.65	0.94	13.79	0.98	14.28

Table 4.4 - Elastic Modulus and Ultimate Strength vs. Temperature for Samples Aged at 125 °C

Test Temp. (°C)	No Aging		150 °C, 10 days		150 °C, 30 days		150 °C, 100 days		150 °C, 200 days		150 °C, 300 days	
	E (GPa)	UTS (MPa)	E (GPa)	UTS (MPa)	E (GPa)	UTS (MPa)	E (GPa)	UTS (MPa)	E (GPa)	UTS (MPa)	E (GPa)	UTS (MPa)
25	11.96	48.19	12.26	52.98	12.42	53.29	12.62	55.23	13.30	57.30	13.64	57.65
50	11.17	43.03	11.73	46.86	12.00	47.99	12.17	50.32	12.20	53.31	12.5	53.85
75	10.11	40.42	10.87	42.91	10.92	44.94	11.05	45.41	11.18	50.69	11.68	51.30
100	8.32	35.77	9.19	39.25	9.56	40.89	10.20	42.60	10.53	46.93	10.97	47.44
125	5.10	22.65	6.03	29.25	6.12	31.02	6.49	33.48	6.99	35.65	7.16	36.10
150	0.73	10.35	0.80	12.78	0.81	13.50	1.19	13.68	1.21	14.20	1.24	14.58

Table 4.5 - Elastic Modulus and Ultimate Strength vs. Temperature for Samples Aged at 150 °C

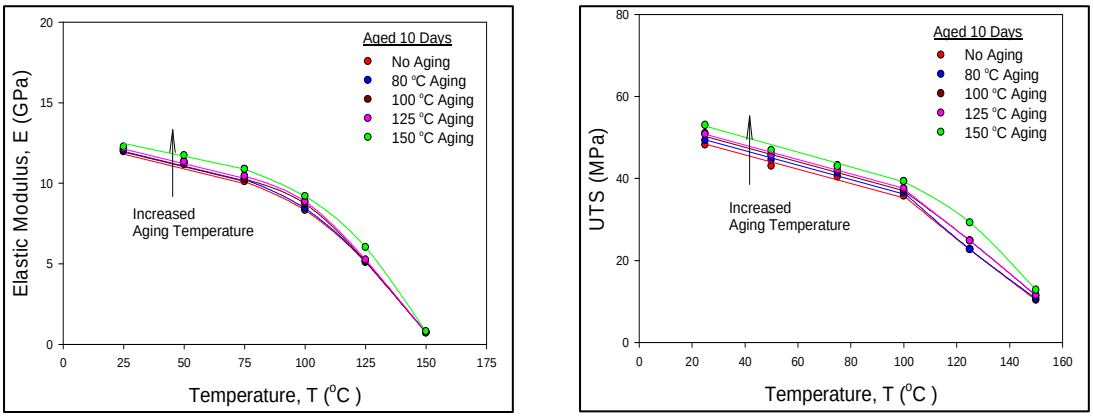

Figure 4.18 - Aging Temperature Effects on Elastic Modulus and UTS (Aged for 10 Days)

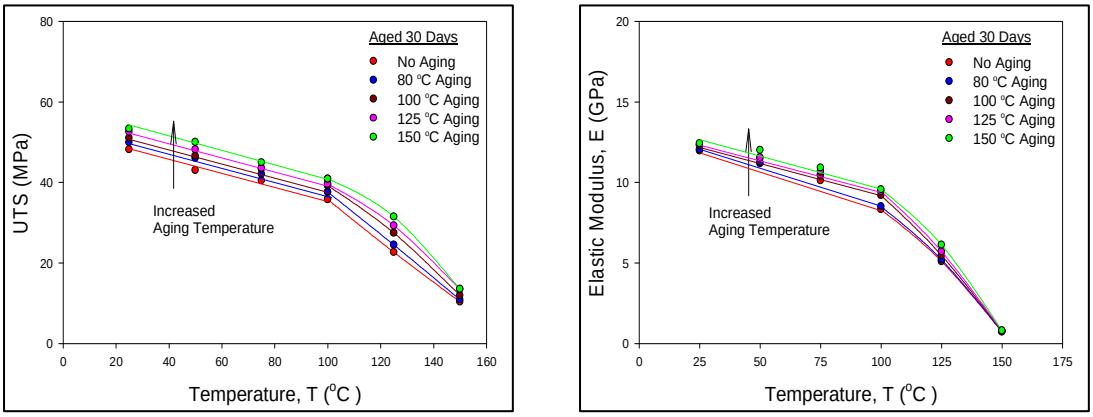

Figure 4.19 - Aging Temperature Effects on Elastic Modulus and UTS (Aged for 30 Days)

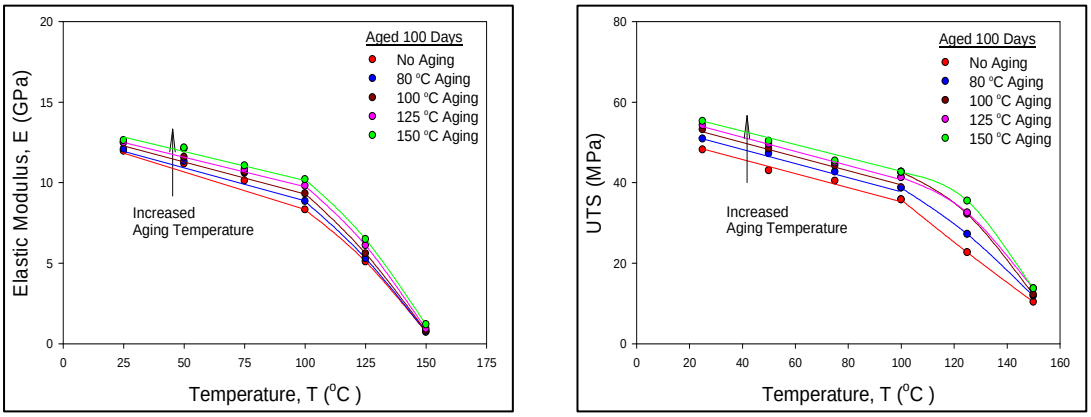

Figure 4.20 - Aging Temperature Effects on Elastic Modulus and UTS (Aged for 100 Days)

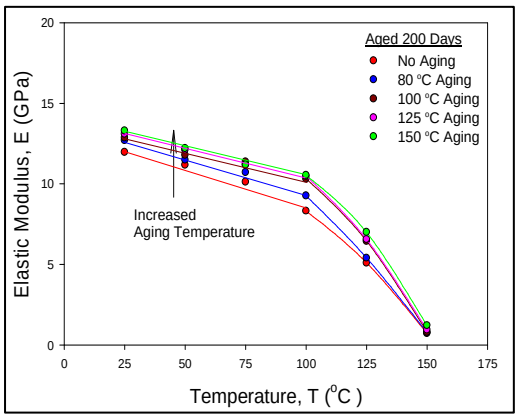

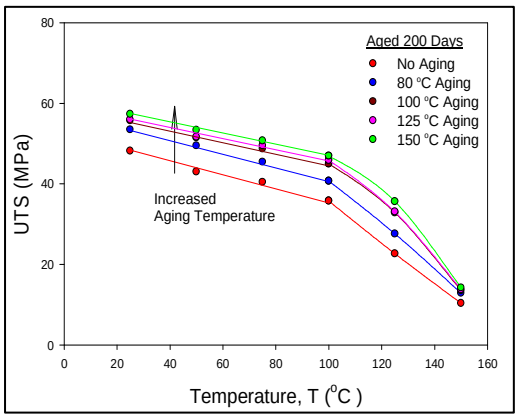

Figure 4.21 - Aging Temperature Effects on Elastic Modulus and UTS (Aged for 200 Days)

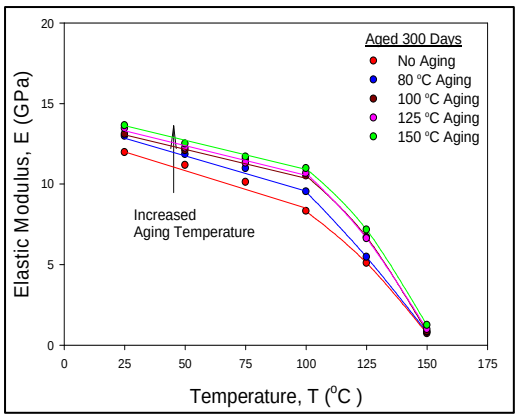

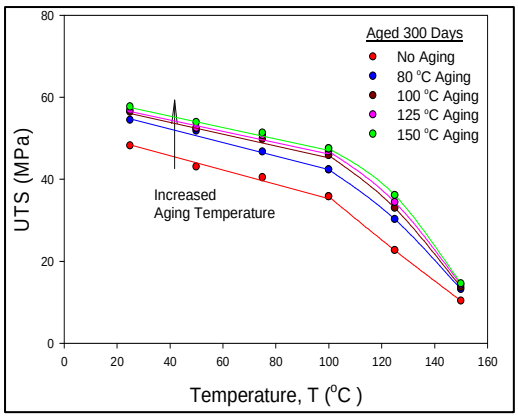

Figure 4.22 - Aging Temperature Effects on Elastic Modulus and UTS (Aged for 300 Days)

where t_{ag} is the aging time. In this expression, constant C_0 is the initial strength for the non-aged specimen, C_1 is the constant rate of change for long term isothermal aging, and C_2 and C_3 are parameters that control the shape of the nonlinear transition region for short aging times. The role of the various empirical model constants are illustrated in Figure 4.24. In practice, the constants were found by using a nonlinear regression analysis to fit equation 4.1 to the data for a given set of aging and testing temperatures. The evolution of the elastic modulus with aging time can be modeled using a similar empirical expression with different fitting constants:

$$E = K_0 + K_1 t_{ag} + K_2\left(1 - e^{-K_3 t_{ag}}\right) \tag{4.2}$$

The evolutions of the modulus and UTS with aging time are shown in Figures 4.25-4.28 for the four different aging temperatures. In all cases, the data for the different testing temperature have been fit using the empirical models in equations (4.1) and (4.3). All of the fitting curves are nonlinear for short aging times. After approximately 100 days of aging, the variations become quite linear. This suggests that the properties can be estimated for longer aging times over 300 days with a linear extrapolation.

4.4 Combined Models for the Effects of Aging Temperature, Aging Time, and Testing Temperature

As the data in this chapter clearly show, the mechanical properties of underfill are a function of the aging temperature, aging temperature, and testing temperature. As stated earlier, prior studies have addressed the effects of the testing temperature, but few have considered aging effects, let alone proposed models to describe these behaviors. In this section, the goal was to provide a single empirical expression to describe the evolution of a particular mechanical property with aging. In particular, it was desired to cast the material properties as functions of

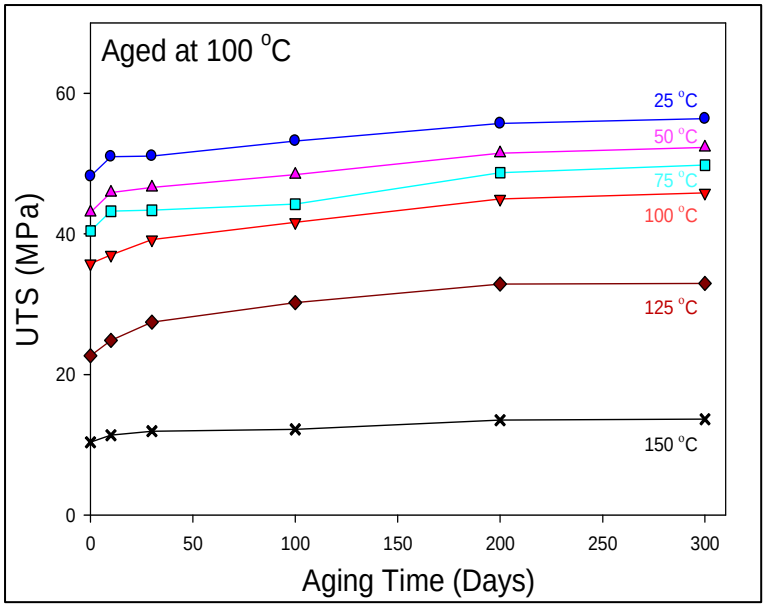

Figure 4.23 - Strength Evolution with Aging Time

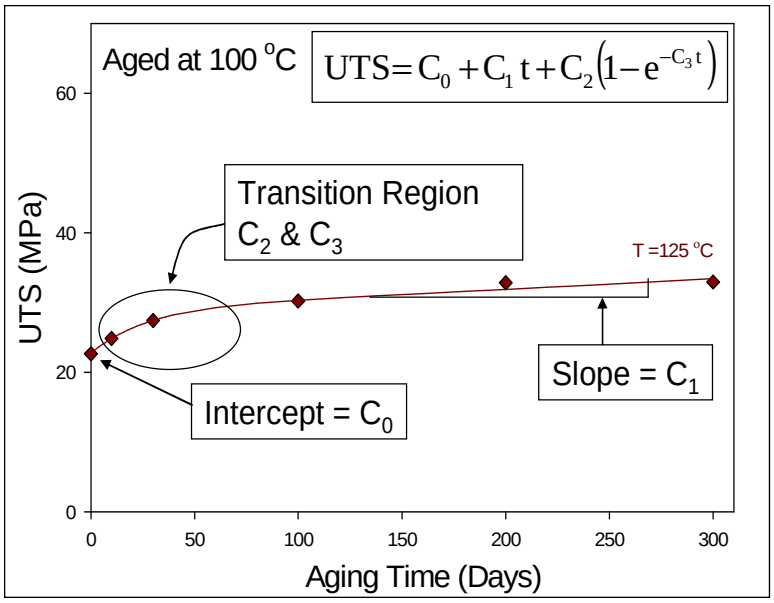

Figure 4.24 - Empirical Fit to Material Property Evolution Data

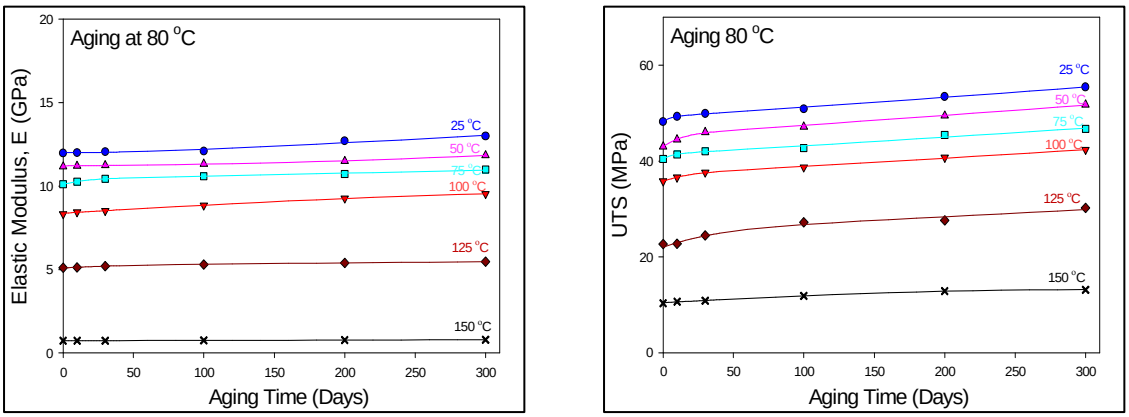

Figure 4.25 - Effective Elastic Modulus and UTS vs. Aging Time for Aging at 80 °C

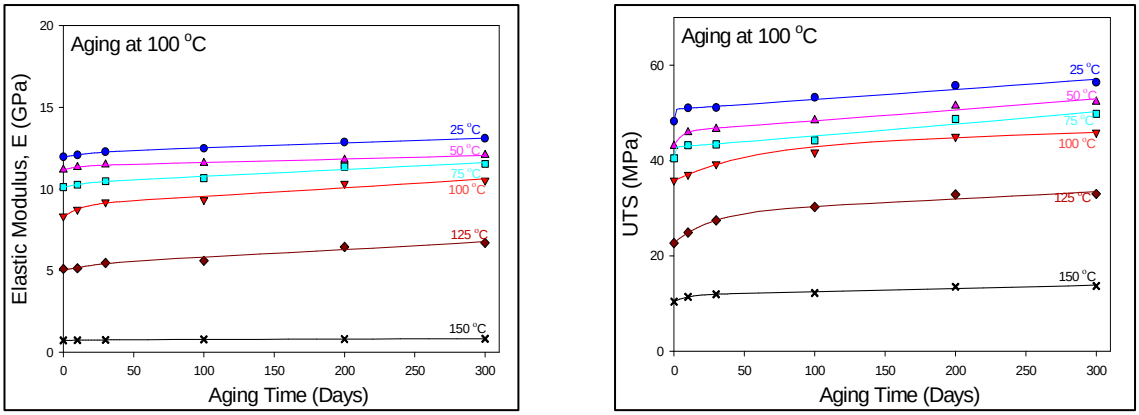

Figure 4.26 - Effective Elastic Modulus and UTS vs. Aging Time for Aging at 100 °C

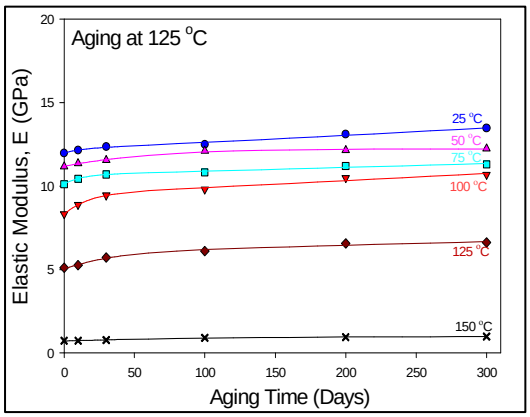

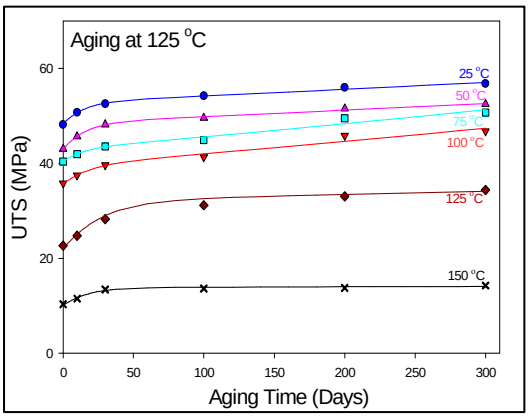

Figure 4.27 - Effective Elastic Modulus and UTS vs. Aging Time for Aging at 125 °C

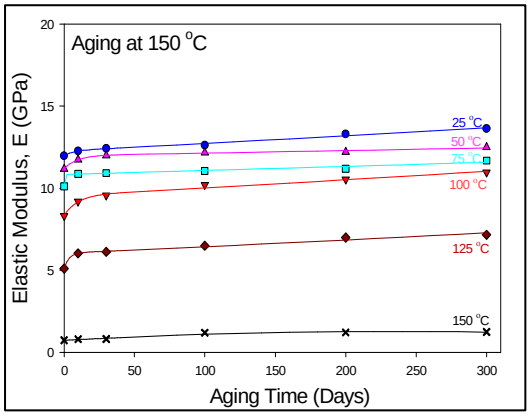

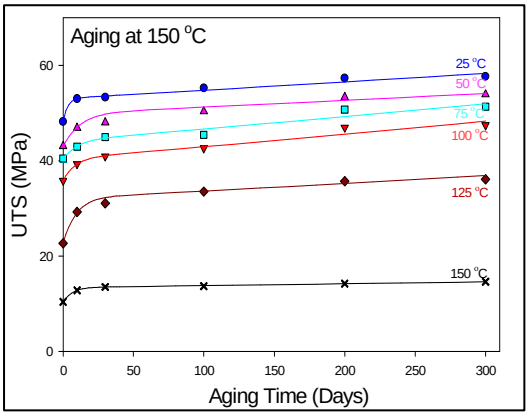

Figure 4.28 - Effective Elastic Modulus and UTS vs. Aging Time for Aging at 150 °C

the three independent variables:

$$E = E(T_{ag}, t_{ag}, T)$$

$$UTS = UTS(T_{ag}, t_{ag}, T) \tag{4.3}$$

where T_{ag} is the aging temperature, t_{ag} is the aging time, and T is the testing temperature.

The best way to simplify the modeling problem is to separate the independent variables. The variables aging temperature and aging time are related to micro-structural changes that occur in the material during the isothermal aging process, while the testing temperature is set independently after the aging has occurred. It is therefore reasonable to consider the aging temperature and aging time effects first, followed by the testing temperature effects.

Many studies have examined thermal phenomena in materials, and an Arrhenius relationship is often used for the temperature dependence. To explore the effects of aging temperature and aging time, the experimental data must be plotted for readings taken at the same testing temperature. For example, Figure 4.29 illustrates the elastic modulus dependence for attesting temperature of 100 °C and various aging conditions prior to testing. These same data are plotted with a 3D viewpoint in Figure 4.30, with aging temperature and aging time on the two in-plane coordinate axes. In an effort to produce a unified model, the empirical model in equation (4.2) can be generalized to include the aging temperature. In this work, it is proposed to add an Arrhenius term for the aging temperature in the form:

$$E = C_0 + (C_1 + C_2 t_{ag} e^{-\frac{Q}{RT_{ag}}})^{C_3} \tag{4.7}$$

where C_0 C_1 C_2 and C_3 are functions of the testing temperature (T), and Q is an activation energy for aging, which is a constant regardless of the testing temperature.

Figure 4.29-4.30 illustrate the fit of equation (4.7) to the experimental data points for a testing temperature of 100 °C. In Figure 4.31, the surface predicted by the model for other aging conditions is illustrated. The same approach can also be applied to the other testing temperatures. In each case, the regression analysis yields a set of values for C_0, C_1, C_2, C_3 and Q. Comparing these parameters for all six of the testing temperatures revealed that the values for C_3 and Q were almost the same for each condition. Consequently, equation 4.7 was simplified by substituting the average values for C_3 and Q:

$$E = C_0 + (C_1 + C_2 te^{-\frac{15970}{RT_{ag}}})^{0.45} \tag{4.8}$$

where E is in GPa, t_{ag} is in days, and T_{ag} is in °C. Equation (4.8) was then simultaneously fit to all of the elastic modulus data (all testing temperature) yielding the corrections shown in Figure 4.32. The calculated parameters are summarized in Table 4.6 and plotted curves temperature in Figure 4.33.

The results in Figure 4.32 illustrate that the model in equation (4.8) is able to accurately represent the evolution of the elastic modulus with aging. However, the plots in Figure 4.33 show that parameters C_0, C_1, and C_2 have a strong dependence on temperature. These dependences can be expressed using the following expression:

$$C_0 = -0.043T + 13.1 \quad C_1 = 0.0003e^{0.044T} \quad C_2 = 0.21e^{0.028T} \quad \text{T} \leq 100\ ^\circ\text{C} \tag{4.9}$$

$$C_0 = -0.17T + 25.6 \quad C_1 = 0.0023T - 0.21 \quad C_2 = -0.058T + 8.9 \quad \text{T} \geq 100\ ^\circ\text{C} \tag{4.10}$$

Substituting these expressions into equation (4.8) yields a complicated but unified model for the evolution of the elastic modulus with aging:

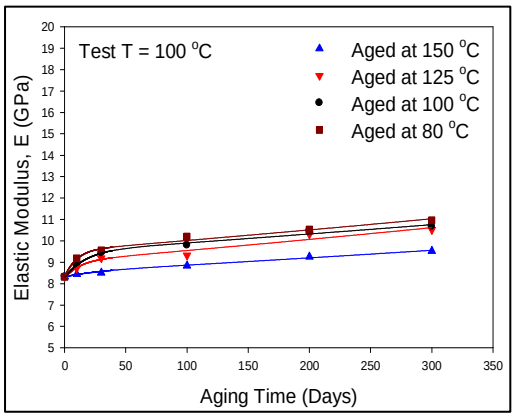

Figure 4.29 - Elastic Modulus vs. Aging Effects for Testing at T = 100 °C

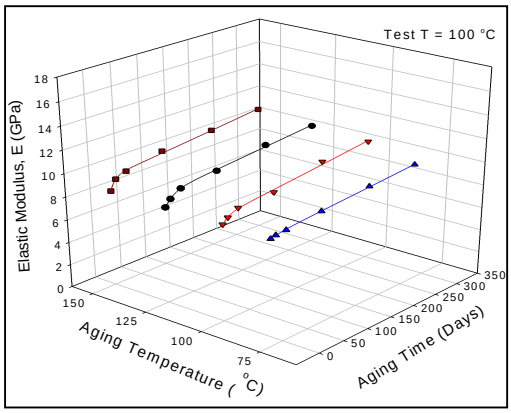

Figure 4.30 - 3D Visualization of Elastic Modulus vs. Aging Effects for Testing at T = 100 °C

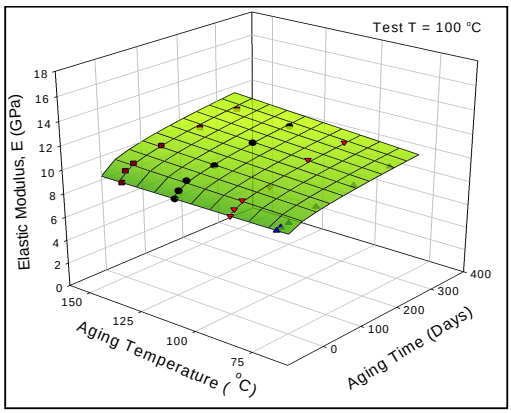

Figure 4.31 - Empirical Model Fit for Elastic Modulus vs. Aging Effects for Testing at T = 100 °C

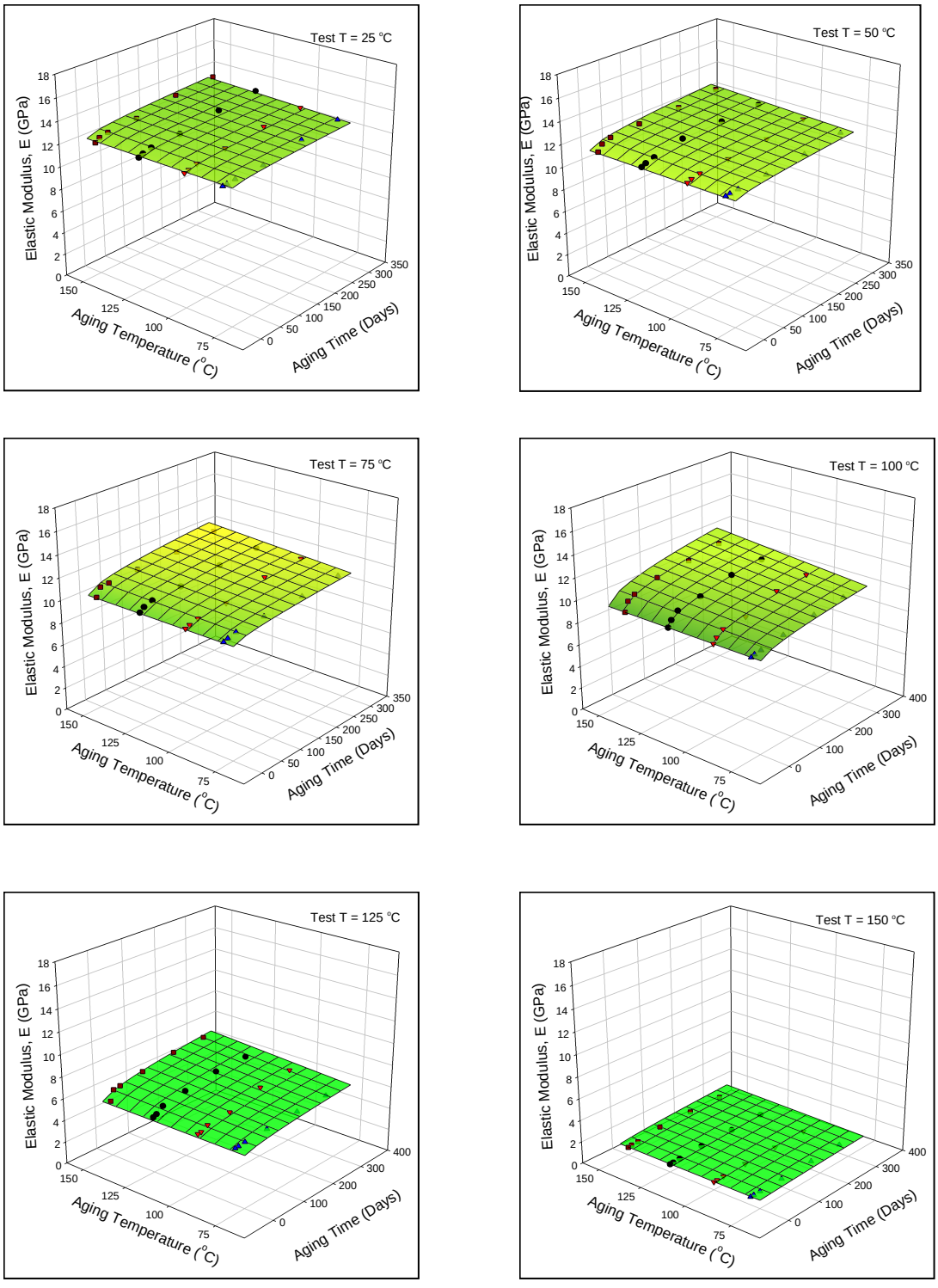

Figure 4.32 - Model Fitting for E vs. Aging Effects at All Test Temperatures

Testing Temperature	25 °C	50 °C	75 °C	100 °C	125 °C	150 °C
C_0	11.91	11.10	9.990	8.24	4.75	0.320
C_1	0.0008	0.004	0.009	0.023	0.088	0.140
C_2	0.372	0.986	2.017	3.037	1.951	0.157

Table 4.6 - Parameter Values for the Elastic Modulus Empirical Model

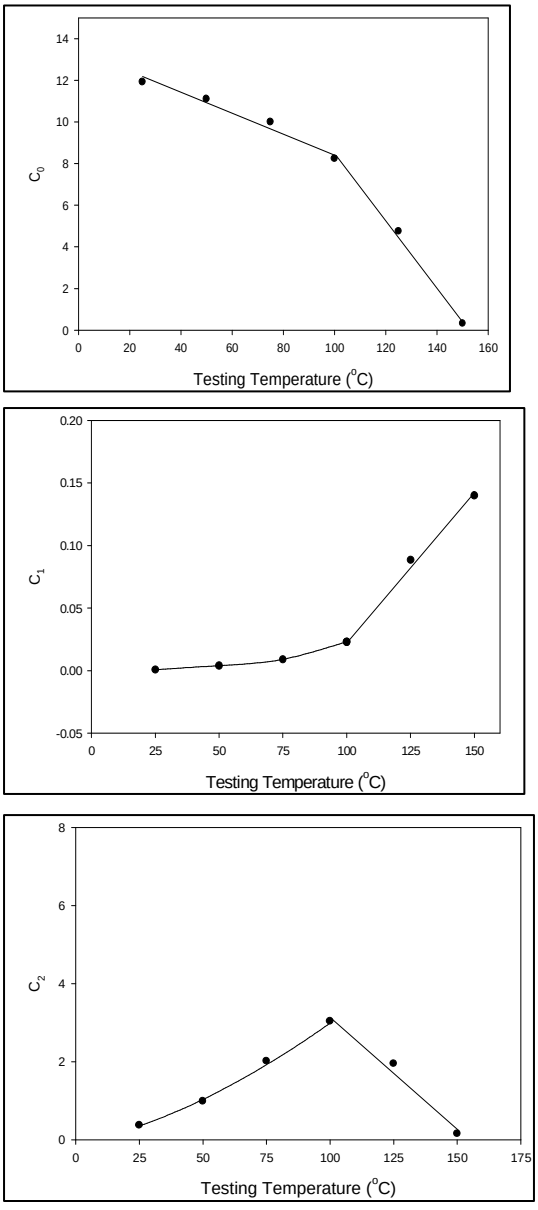

Figure 4.33 - Elastic Modulus Empirical Model Parameters vs. Testing Temperature

$$E = 13.1 - 0.043T + (0.0003e^{0.044T} + 0.21e^{0.028T} t_{ag} e^{-\frac{15970}{RT_{ag}}})^{0.45} \qquad T \leq 100\ °C \qquad (4.11)$$

$$E = 25.6 - 0.17T + ((0.0023T - 0.21) + (-0.58T + 8.9) t_{ag} e^{-\frac{15970}{RT_{ag}}})^{0.45} \qquad T \geq 100\ °C \qquad (4.12)$$

where E is in GPa, T and T_{ag} are in °C, and t_{ag} is in days.

A similar empirical model can be proposed to model the evolution of the UTS with aging:

$$UTS = C'_0 + (C'_1 + C'_2\, te^{-\frac{Q'}{RT_{ag}}})^{C'_3} \qquad (4.13)$$

In this case, it was found $C_1^{'} \approx 0$ for all testing temperatures. Average values of $C_3^{'}$ and $Q^{'}$ were again found, and this calculation yielded:

$$UTS = C'_0 + (C'_2\, te^{-\frac{24580}{RT_{ag}}})^{0.38} \qquad (4.14)$$

where UTS is in MPa, T and T_{ag} are in °C, and t_{ag} is in days,. The regression fits of equation 4.14 to the experimental data are shown in Figure 4.34. The parameters $C_0^{'}$ and $C_2^{'}$ were found to be dependent on the testing temperature (see Table 4.7 and Figure 4.35). The dependencies were well fit using:

$$C_0^{'} = -0.16T + 51.8 \qquad C_2^{'} = 1800 + 3.4e^{0.035T} \qquad T \leq 100\ °C \qquad (4.15)$$

$$C_0^{'} = -0.5T + 86.5 \qquad C_2^{'} = -53.7T + 8337 \qquad T \geq 100\ °C \qquad (4.16)$$

Substituing these expressions into equation (4.14) yields a complicated but unified model for the evolution the UTS with aging:

$$UTS = 51.8 - 0.16T + ((1800 + 3.4e^{0.035T}) t_{ag} e^{-\frac{24580}{RT_{ag}}})^{0.38} \qquad T \leq 100\ °C \qquad (4.17)$$

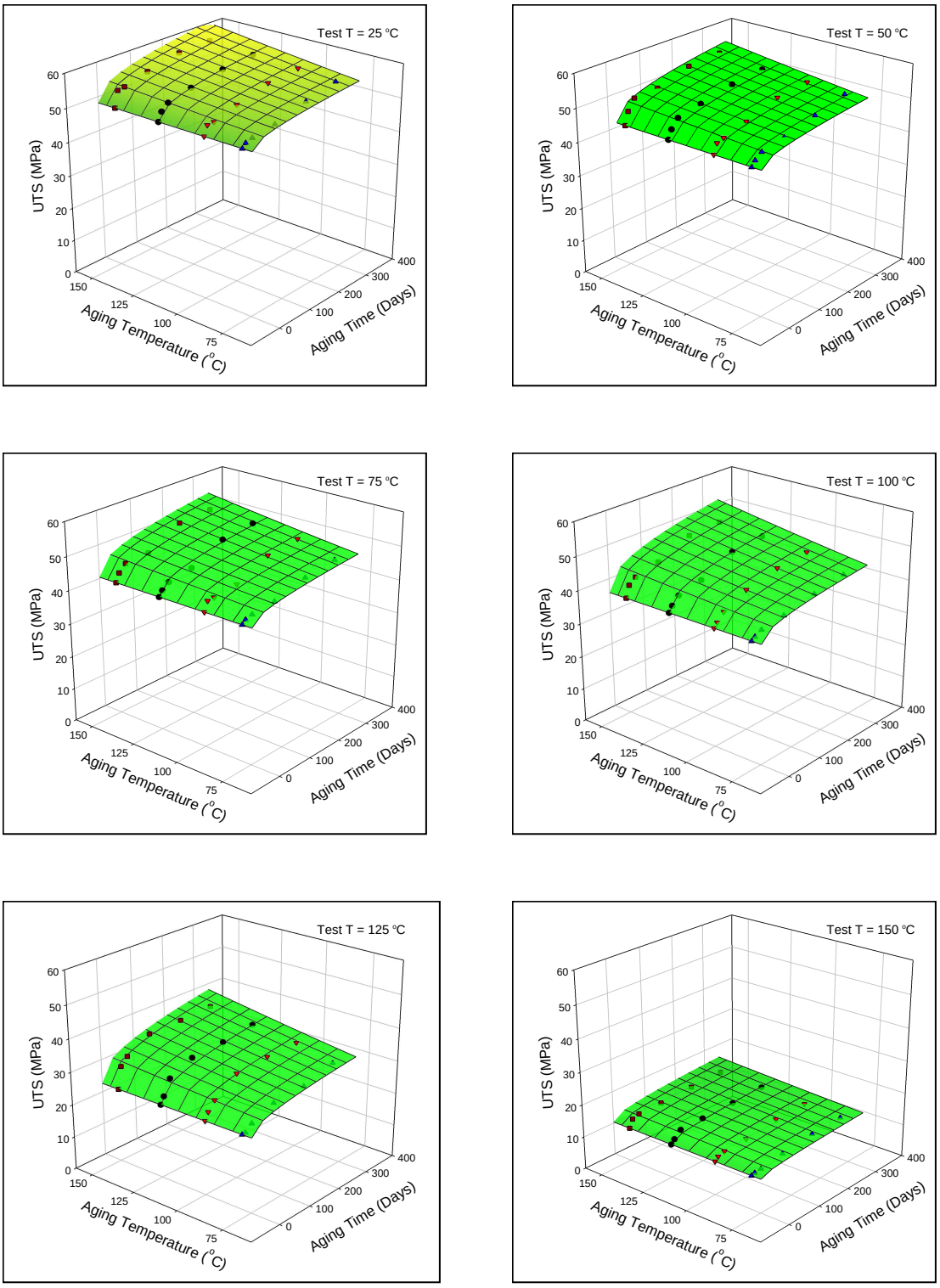

Figure 4.34 - Model Fitting for UTS vs. Aging Effects at All Testing Temperatures

Testing Temperature	25 °C	50 °C	75 °C	100 °C	125 °C	150 °C
C_0	48.19	43.03	40.42	35.77	22.65	10.35
C_1	1.5e-017	2.21e-017	3.8e-017	7.8e-017	9.2e-017	1.1e-016
C_2	1868.8	2010.8	2255.9	2921.7	1703.1	234.53

Table 4.7 - Parameter Values for the UTS empirical Model

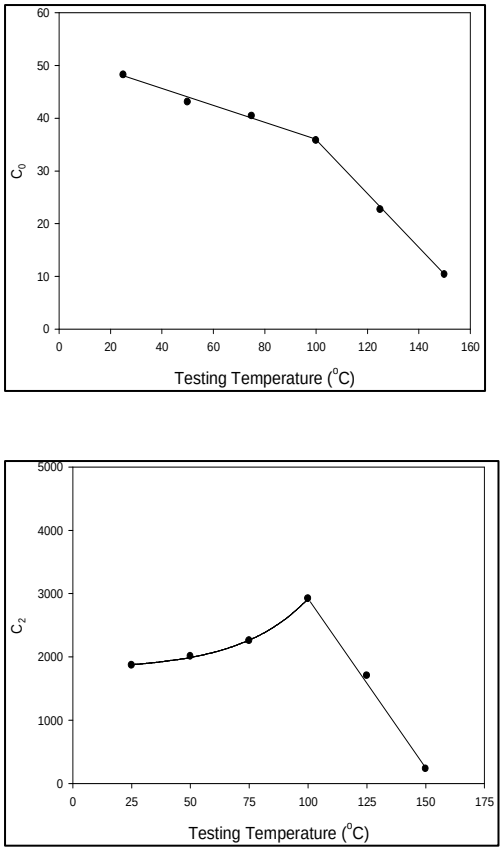

Figure 4.35 - Ultimate Tensile Strength Empirical Model Parameters vs. Testing Temperature

$$UTS = 86.5 - 0.5T + ((8337 - 53.7T_{ag})t_{ag}e^{-\frac{24580}{RT_{ag}}})^{0.38} \qquad T \geq 100\ °C \qquad (4.18)$$

where UTS is in MPa, T and T_{ag} are in °C, and t_{ag} is in days.

4.5 Summary and conclusions

In this chapter, the effect of isothermal aging on the stress-strain behavior of underfill was investigated. The underfill material microstructure was found to remain unchanged during the aging process. However, DSC measurements showed that the residual cure energy decreased during the isothermal aging process, even after the samples were cured at 150 °C for 30 minutes, as per the manufacturer's suggestion.

The results obtained revealed a clear enhancement of the underfill mechanical properties as a function of the aging temperature and aging time. Both the underfill effective elastic modulus (initial slope) and ultimate tensile strength (highest stress before failure) increased monotonically with the amount of isothermal aging or aging temperature, regardless of whether the aging temperature was below, at, or above the T_g of the material. With 300 days isothermal aging, the elastic modulus increased by up to 31% and the ultimate tensile strength increased by up to 45%. For the underfill evaluated, softening behavior was observed above a temperature of 100 °C, although the documented T_g is about 137 °C.

An empirical model with linear and exponential terms and four constant parameters was proposed to describe the evolution of the mechanical properties of underfill with aging time. Furthermore, two complicated empirical models were constructed to estimate the elastic modulus and UTS of the underfill as functions of aging temperature, aging time, and testing temperature. The models provided reasonably good estimates to the experimental data.

CHAPTER 5

ISOTHEMAL AGING EFFECTS ON THE CREEP BEHAVIORS

5.1 Introduction

Materials such as solders and polymers undergo time-dependent deformation under mechanical stress at elevated temperatures. Various creep mechanisms may dominate at different temperatures, and sometimes more than one mechanism takes place simultaneously in the same material [45]. In reality, all deformations are time dependent but the characteristic times for creep deformations are orders of magnitude larger than those for either elastic or plastic deformations [46].

Creep is commonly encountered in solder joints, underfills, and printed wiring board base materials in electronic packaging applications. Many electronic devices are exposed to elevated temperatures for long periods. Rheological phenomena may cause structural components to suffer from durability shortening and about 10% of failures result from creep processes and stress-relaxation effects [47].

Creep deformation mechanisms in polymers are very different from those in metals and ceramics because of their unique microstructures. Unlike most metals and ceramics with highly periodic crystalline structures, polymers are made of long molecules and consist of a chain of atoms or a three-dimensional cross-linked network bonded by covalent forces. Consequently, polymer mechanical properties differ markedly from those of metals and ceramics [46].

Polymeric materials are generally classified into three groups:

- Thermoplastics (crystalline and non crystalline)
- Thermosets
- Rubbers

Most of the polymers used in the electronic packaging application are either thermoplastics or thermosets. Thermosets have a primary three-dimensional cross-linked bonding network, while thermoplastics have only secondary bonding connections.

Polymer creep behaviors are dependent not only on time, temperature and stress, but also on microstructure. Polymer crystalline structures resist creep much more than amorphous structures, since the molecules in crystals have shorter bond distances, and consequently stronger intermolecular bonds. Thermosetting materials made up of primary cross-linked molecular networks resist creep more readily than thermoplastic composed of secondary bonded chains of molecules because the cross-linked connections limit the amount of creep slippage that can take place.

Creep tests are often used to characterize the viscoelastic time-dependent behavior of a polymer. In a creep test, a constant force is first applied quasi-statically to a uniaxial tensile specimen, and then creep occurs as a slow continuous deformation of the material under stress. Creep behaviors are thus time dependent strain deformations at constant uniaxial stress, and creep deformation is one of the major failure modes in electronic packaging. Figure 5.1 illustrates a typical creep curve for a polymer underfill, and Figure 5.2 shows the corresponding creep strain rate.

The creep curve begins with an elastic jump in strain as the load is applied. During the initial period of creep deformation (primary creep), there is a steep drop in the creep strain rate.

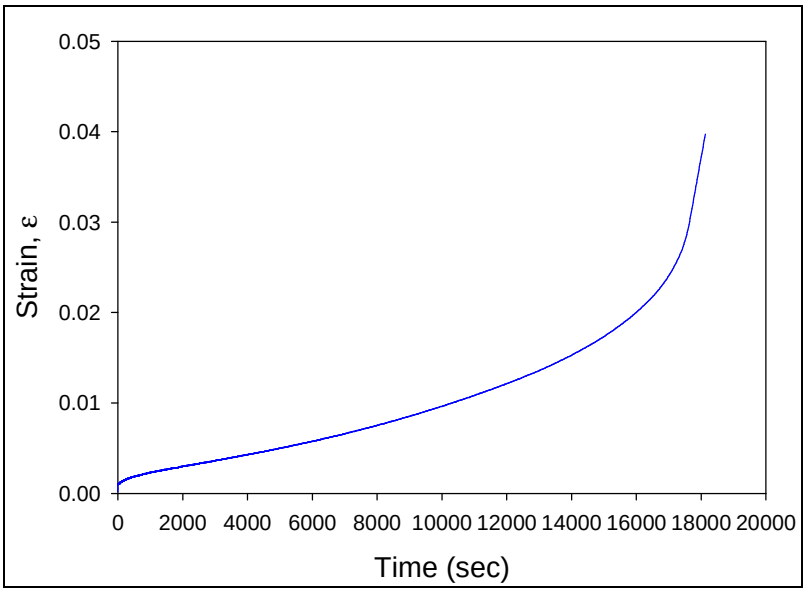

Figure 5.1 - Typical Creep Strain vs. Time Response

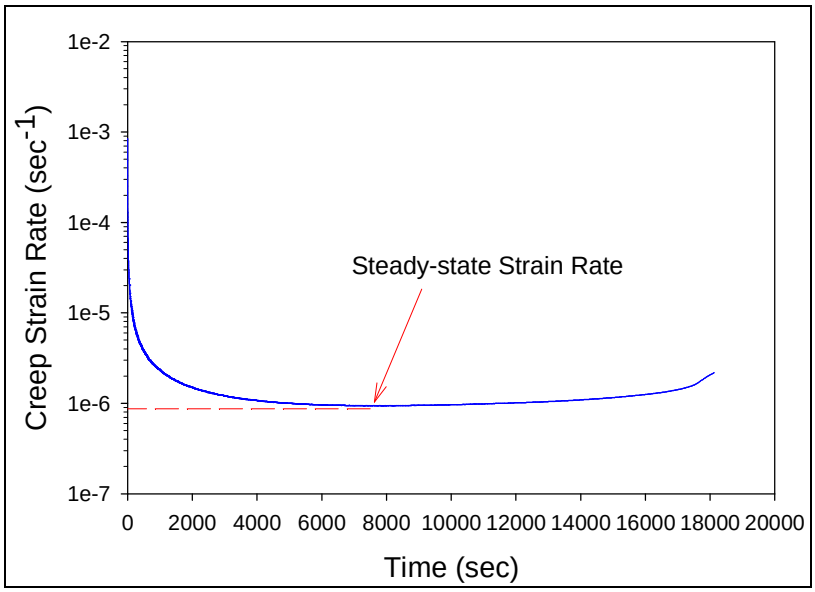

Figure 5.2 - Typical Creep Strain Rate vs. Time Response

This is followed by a period of nearly linear response (secondary creep), where an approximately constant creep rate is observed. The secondary creep rate is the slope of the creep curve in this relatively stable region (steady state region). The secondary creep rate represents the material creep resistance factor because most deformations occur in this region. The material continues to elongate until its creep deformations accumulate (tertiary creep) and failure occurs.

It is often not economic to run lengthy creep tests at elevated temperatures, and the long term creep properties are sometimes predicted by substituting temperature for time, i.e., by estimating the long term creep behavior from short term tests at a higher temperature with the same stress level. The theoretical basis for this substitution is to assume that there are no microstructural changes so that the time-temperature parameters can be estimated by extrapolating the results of short term creep tests [48, 49]. Similarly, certain relations provide time compression at the expense of higher temperature. These relations, discussed earlier in Section 1.7, are time temperature superposition (TTSP) and time stress superposition (TSSP) [23, 29, and 39].

Research on the effects of physical aging on the creep of polymers has been summarized in detail in a monograph by Struik [21]. His work focused primarily on glass-forming materials such as polymers and inorganic glasses, which are briefly annealed at a temperature above their T_g, and then rapidly cooled (quenched) to a lower temperature significantly below the T_g. After quenching, the material remains in a non-equilibrium thermodynamic state from which its physical properties (mechanical, thermodynamic, etc.) slowly evolve towards equilibrium. This process is often called physical aging, and the effects on the small strain (linear viscoelastic) creep response of polymers have been well documented. In general, polymers subjected to thermal aging after quenching become stiffer and more brittle, while their creep rate and

compliance gradually decrease as the aging progresses. For example, several recent studies have looked at physical aging effects in epoxy without fillers (Lee and McKenna [23], and Miyano, et al. [43]).

Reports in the extensive literature on physical aging of various polymers generally involve brief exposures to temperatures above the T_g, followed by an examination of the aging process at temperatures significantly below the T_g [21, 24, 43] The minimal exposures above the T_g are solely for the purpose of annealing or de-aging the samples. However, in many harsh environment applications of electronic packaging, the assemblies are subjected to temperatures at or above the T_g for extended periods. There are few studies on the effects of aging at such temperatures on the mechanical behavior of underfill materials. Those that have been performed, on polystyrene [24] and PEEK [44] noted unexpected types of behavior after cooling.

Elevated temperature aging also affects the adhesion and interfacial properties of underfills, and has been shown to be detrimental to electronic assemblies with underfill. For example, Liu, et al. [50] have shown that drop reliability is severely reduced in CSP assemblies with underfill subjected to dry aging at 125 °C prior to dropping.

5.2 Objectives and Test Program

In this study, the effects of isothermal aging on the creep behavior of a typical underfill (UF1) were examined for various aging temperatures, aging durations, testing temperatures, and stress levels. The evolution of the secondary creep rate with aging was also investigated, and an empirical model was developed to fit the observed variations. Using the specimen preparation procedure described in Section 2.3, samples were prepared and isothermally aged for up to 10 months at 80, 100, 125, and 150 °C. The samples were subjected to isothermal aging times of 1,

3, 10, 30, 100, 200, and 300 days, as shown in Table 5.1. Creep test were performed on aged and non-aged specimens at test temperatures of 80, 100 and 125 °C. The applied stresses were 10, 20, and 30 MPa for the testing temperatures of 80 and 100 °C, and stress levels of 10, 15, and 20 MPa were used for the 125 °C testing temperature. The chosen stress levels were approximately 25%, 50% and 75% of the ultimate strength of the underfill material at each testing temperature.

The utilized test matrix allowed for the exploration of the effects of aging temperature, aging time, testing temperature, and stress level on the creep behavior of the underfill material. Due to the long test times involved, only three specimens were tested for each set of test conditions (aging time, aging temperature, stress level, and test temperature).

5.3 Experimental Results and Discussion

During each creep test, the specimen was loaded at a strain rate 0.001 sec^{-1} until the desired stress level was reached, after which the load was held constant, and the strain vs. time response was recorded. Testing was performed for a duration of up to 6000 seconds. For each set of aging conditions, specimens were tested at three different temperatures (T = 80, 100 and 125 ^{o}C) and at three different stress levels at each temperature. Three samples were tested for each combination. Therefore, for each set of aging conditions, there were 27 samples tested. The raw data for each testing condition were averaged to generate a creep curve to represent the creep behavior for each testing condition.

Sample creep curves for non-aged specimens tested at 100 °C are presented in Figure 5.3. The specimens tested at the stress level of 10 MPa did not fail during the 6000 sec duration creep test. The specimens subjected to stress of 20 and 30 MPa failed without progressing to the tertiary range. From the series of experimental creep curves shown in Figure 5.3, a

Aging Temperature	0 Day	1 Day	3 Days	10 Days	30 Days	100 Days	200 Days	300 Days
80° C	*	*	*	*	*	*	*	*
100° C		*	*	*	*	*	*	*
125° C		*	*	*	*	*	*	*
150° C		*	*	*	*	*	*	*

Table 5.1 - Matrix of Aging Exposures for Creep Tests

corresponding set of isochronous stress-stain curves can be extracted as shown in Figure 5.4. These curves give the dependence of stress on strain at particular times. It is clear that the isochronous stress-strain curves are not straight lines, which shows that the epoxy material being studied is a nonlinear viscoelastic material, and that Boltzmann's linear superposition principle cannot be applied for the load range used in this investigation.

5.3.1 Stress Level and Test Temperature Effects and Comparison

The creep curve recorded for specimens aged at 100 °C are shown in Figures 5.5-5.8 for aging times of 0 and 1 day (Figure 5.5), 3 and 10 days (Figure 5.6), 30 and 100 days (Figure 5.7), and 200 and 300 days (Figure 5.8). For each aging duration, creep tests were performed at three testing temperatures: 80, 100, 125 °C.

The data in Figures 5.5-5.8 reveal that the specimens underwent large inelastic deformation with increasing stress level and testing temperature. With lower testing temperature and lower stress levels, some specimens did not break during the creep tests, with their creep curves extending out to the full 6000 seconds. However, some specimens failed very quickly at higher stress and testing temperatures, even though the load levels were lower than the ultimate tensile strength. The curves show only primary and secondary creep regions, and no tertiary creep behavior was observed before failure occurred. The creep curves for the non-aged specimens were treated here as the baseline response, to which the results for the aged specimens were compared.

The observed creep behaviors were dependent on the magnitude of both the stress and the testing temperature. The aging temperature and aging time also had a great impact on the epoxy creep behaviors, because a close examination of these results reveals that the specimens became

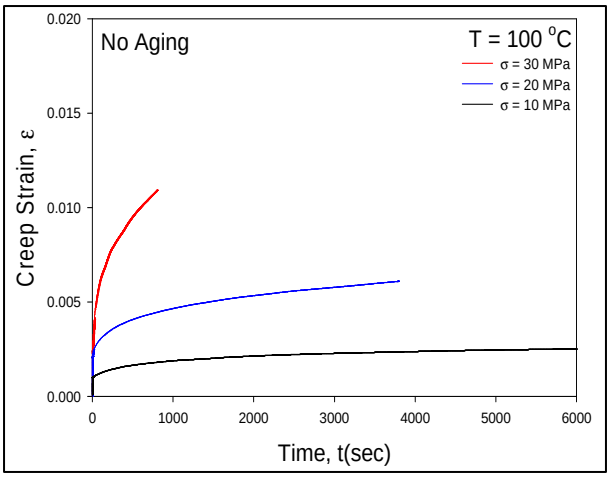

Figure 5.3 - Creep Curves for Non-Aged Specimens Tested at 100 °C

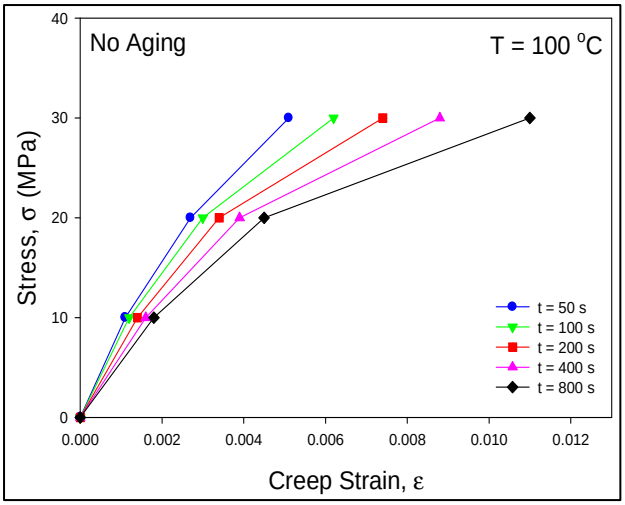

Figure 5.4 - Isochronous Stress-Strain Curves for Non-Aged Specimens Tested at 100 °C

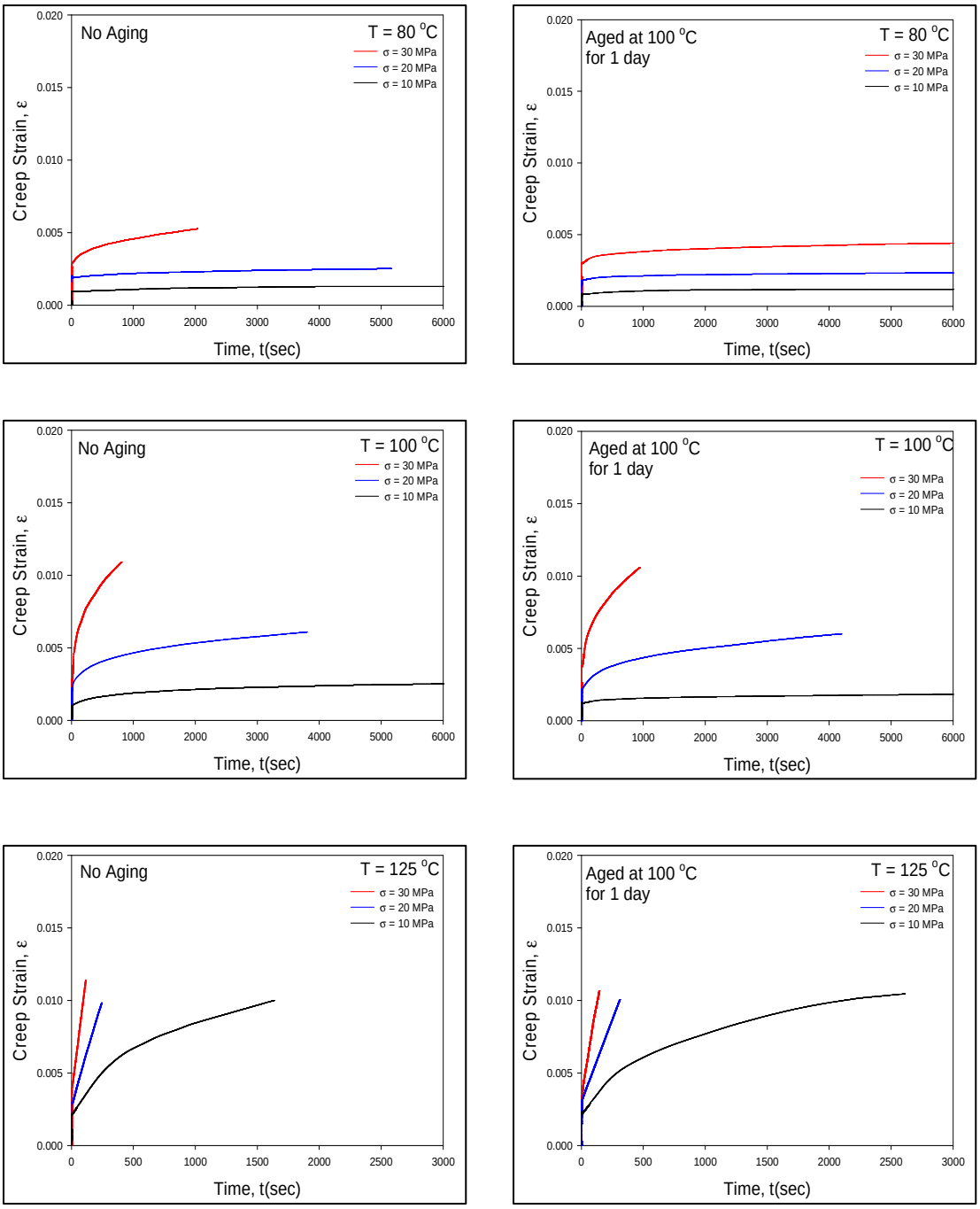

Figure 5.5 - Creep Curves for Various Stresses (Samples Aged at 100 °C for 0 and 1 Day, Tested at 80, 100, 125 °C)

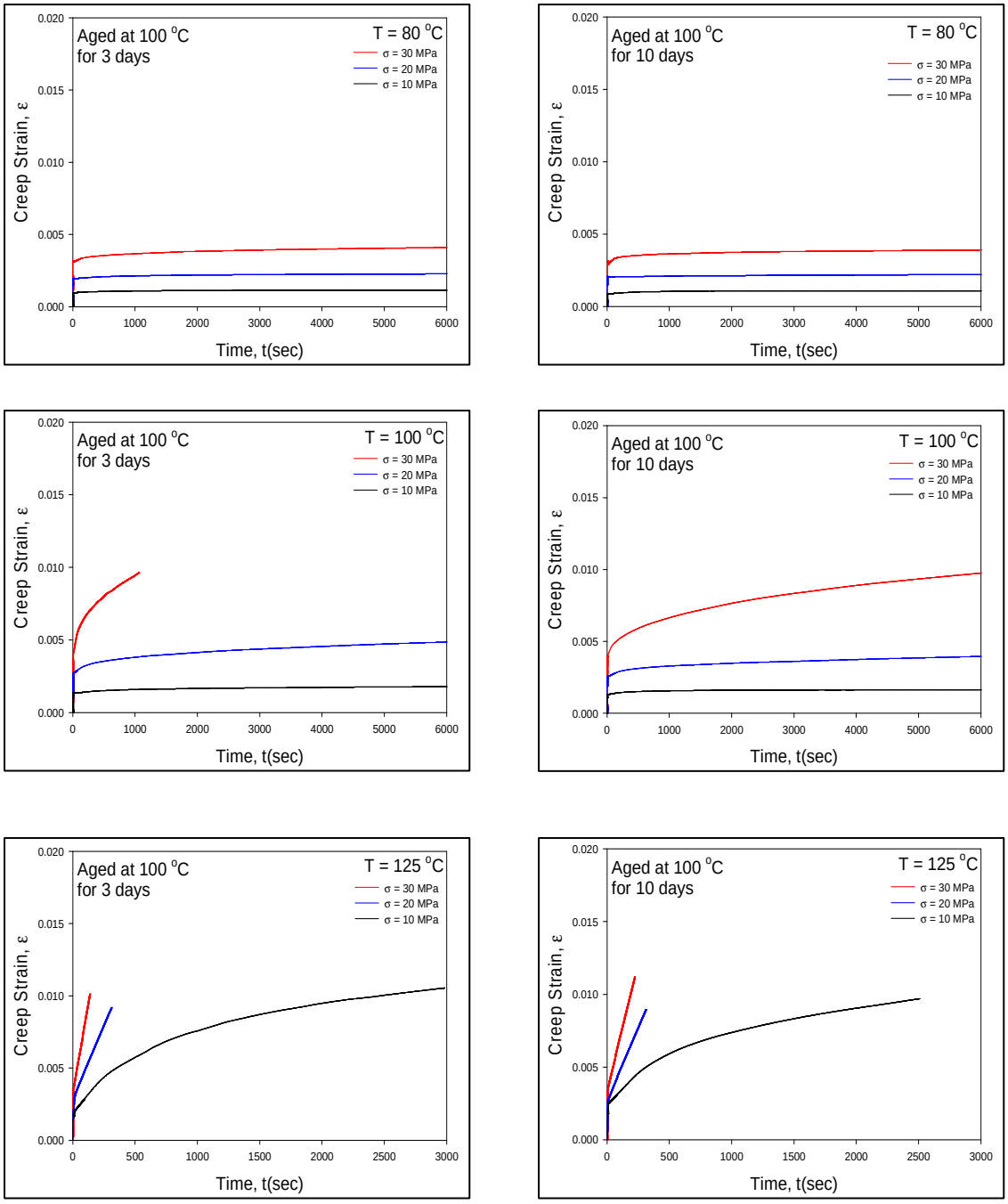

Figure 5.6 - Creep Curves for Various Stresses (Samples Aged at 100 °C for 3 and 10 Days, Tested at 80, 100, 125 °C)

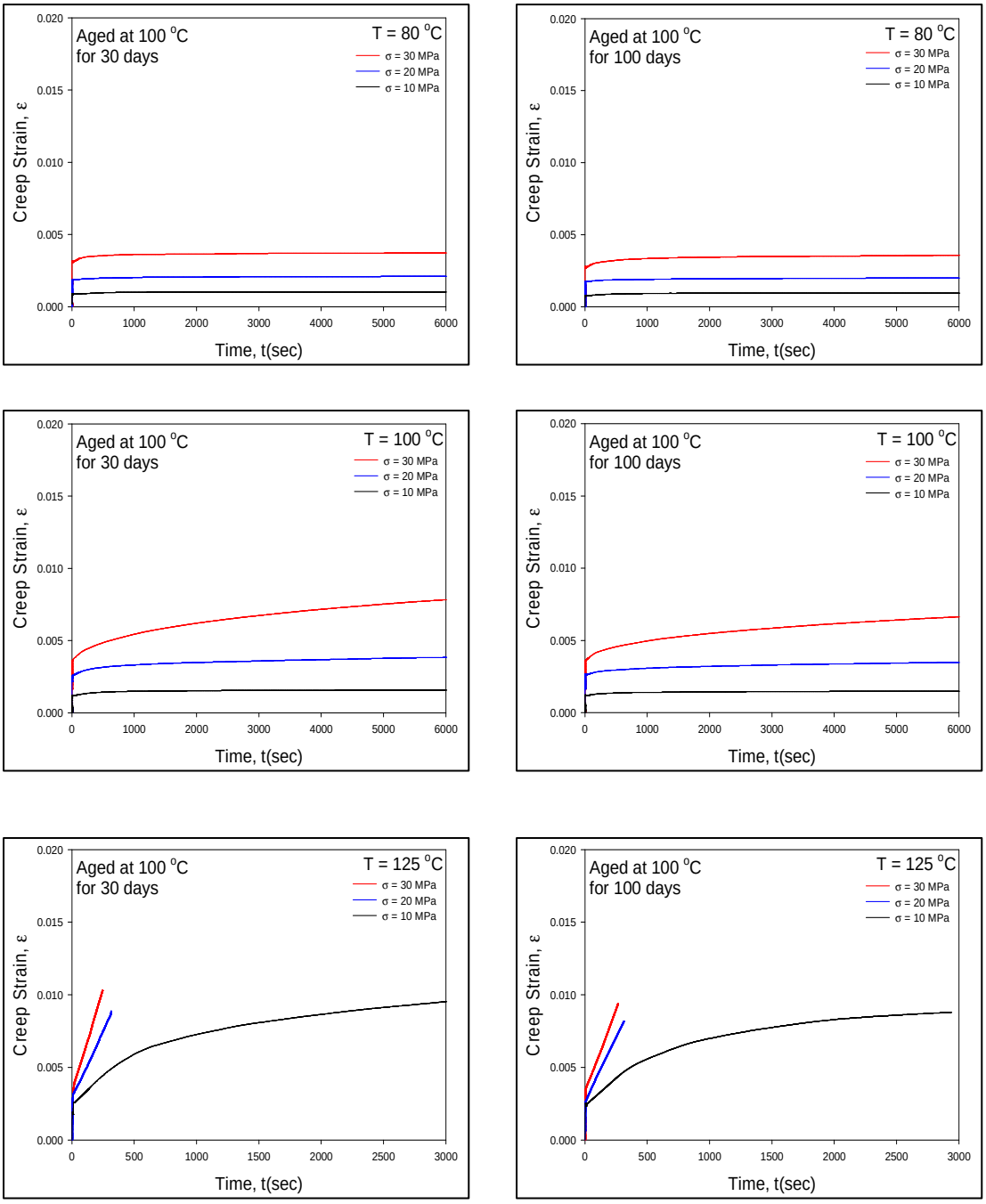

Figure 5.7 - Creep Curves for Various Stresses (Samples Aged at 100 °C for 30 and 100 Days, Tested at 80, 100, 125 °C)

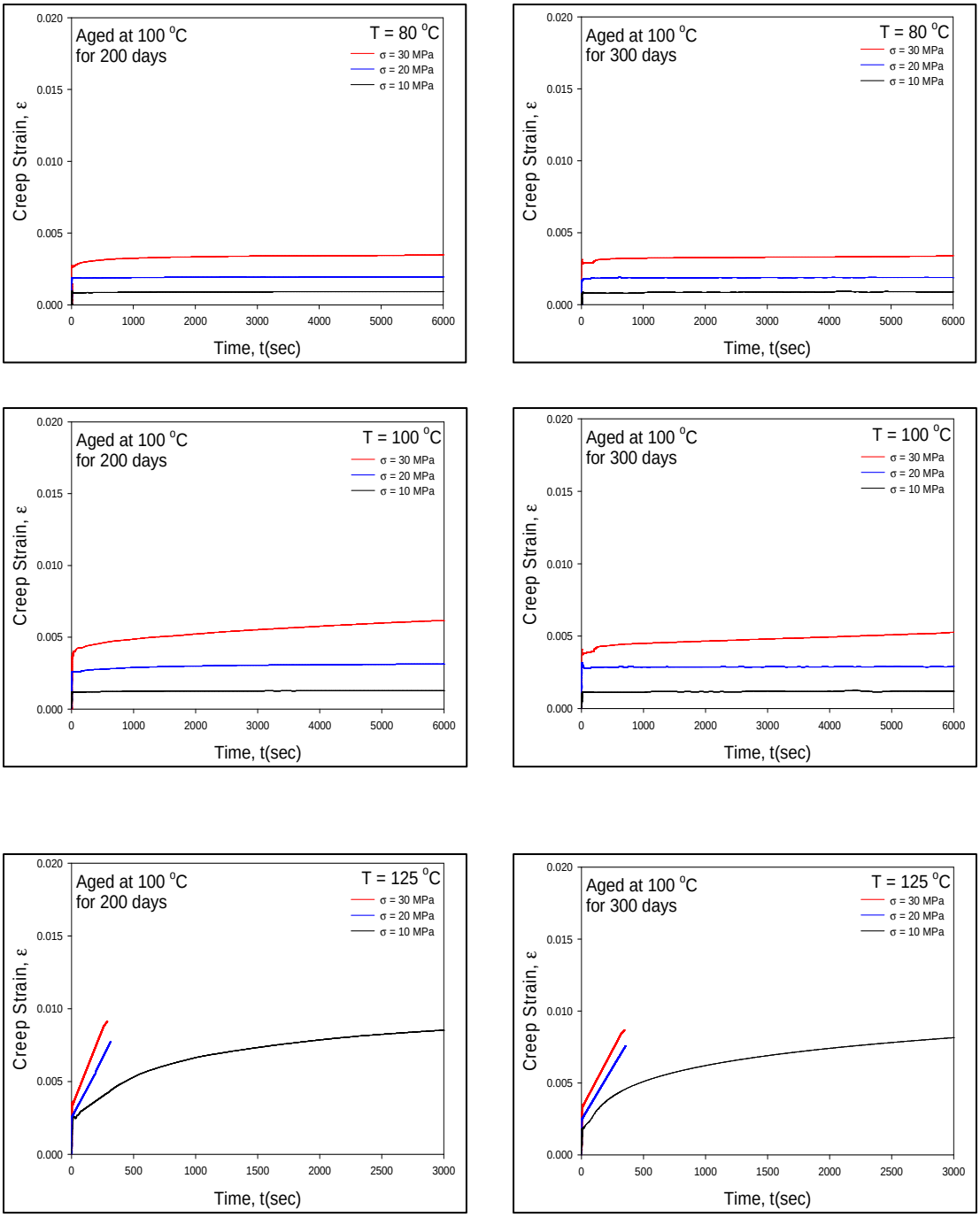

Figure 5.8 - Creep Curves for Various Stresses (Samples Aged at 100 °C for 200 and 300 Days, Tested at 80, 100, 125 °C)

stiffer and creep was reduced with increasing aging time and aging temperature.

5.3.2 Aging Time Effects and Comparison

To investigate the effect of isothermal aging time on the creep behavior, the curves with the same stress and test temperature were extracted from Figures 5.5-5.8, and combined. These results are shown in Figure 5.9 for testing at 80 and 100 °C, and in Figure 5.10 for testing at 125 °C. Looking at these graphs, it is clear that for a given test time, the creep strains were much lower for aged samples with longer aging times. It is also clear that the secondary creep strain rate decreased with longer aging times. As discussed in the next section, this reduction in creep rate can be up 100X.

Similar creep test results for the specimens aged at 80 °C, 125 °C and 150 °C are shown in the Appendix. All had similar trends for the effects of isothermal aging as the samples aged at 100 °C discussed above.

5.4 Empirical Model for the Evolution of the Secondary Creep Rate

For glassy polymers in ambient temperature environments, the most important mechanism governing their behavior is the glass to rubber relaxation mechanism. The time scale for this mechanism can be protracted and the complex performance of epoxy nanocomposites can only be understood by combining experimental studies with effective modeling. Therefore, simulation is an essential tool due to the constant demand for new materials for future engineering applications [51].

From the creep curves shown in Figures 5.5-5.10 above, the primary creep region exhibited a nonlinear strain vs. time relationship. However, the secondary creep region was the predominant response, and the secondary creep rate for each curve was determined. Figure 5.11

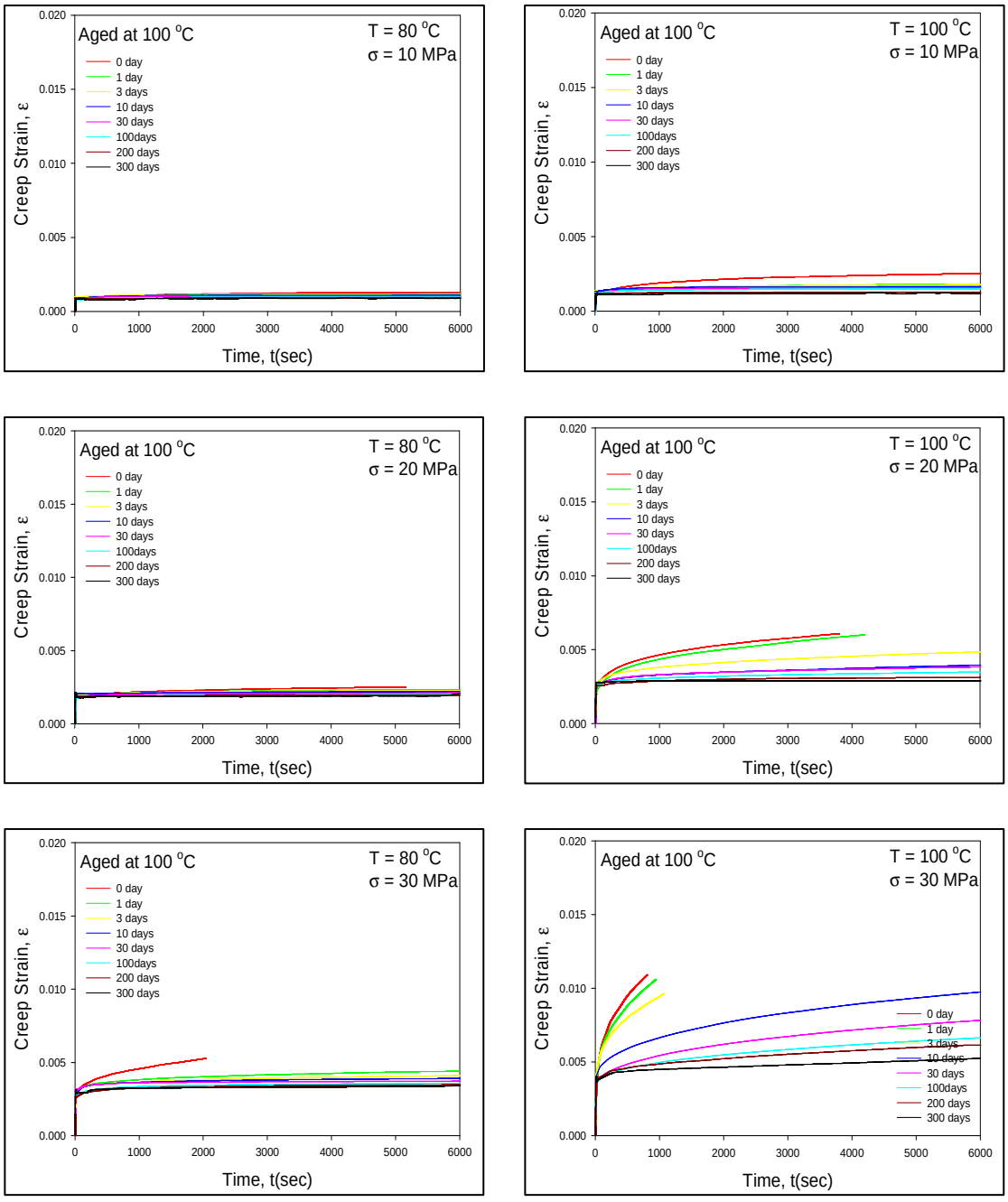

Figure 5.9 - Creep curves for Various Aging Times (Samples Aged at 100 °C, Tested at 80, 100 °C)

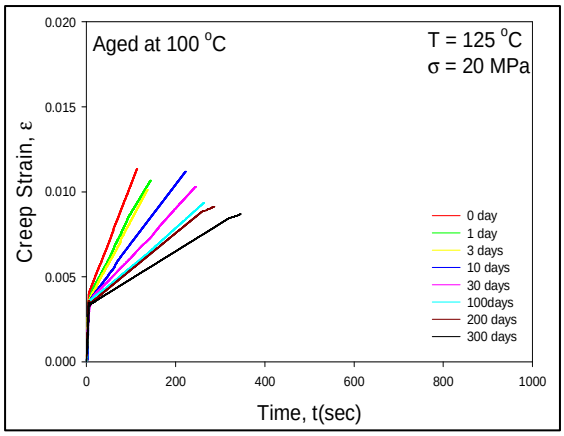

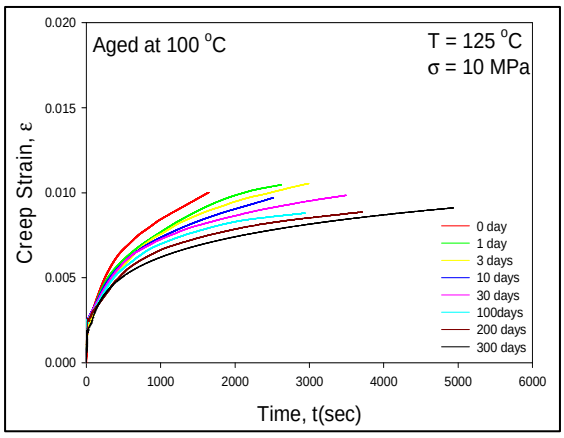

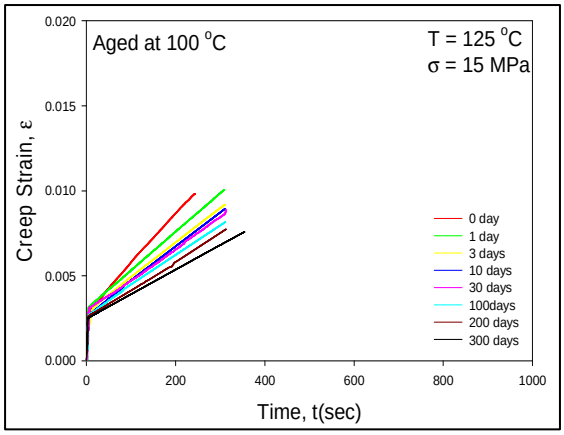

Figure 5.10 - Creep Curves for Various Aging Times (Samples Aged at 100 °C, Tested at 125 °C)

illustrates the variations of the secondary creep rate with aging time for specimens aged 100 °C prior to testing. Each graph is for a different testing temperature (80, 100, 125 °C) and each curve on a graph represents a unique value of applied stress. The vertical axis is on a log scale, and the curves connecting the experimental data points in Figure 5.11 are regression fits of the empirical relation:

$$\log \dot{\varepsilon} = C_0 + C_1 t + C_2 (1 - e^{-C_3 t}) \tag{5.1}$$

or

$$\dot{\varepsilon} = \exp^{C_0 + C_1 t + C_2 (1 - e^{-C_3 t})} \tag{5.2}$$

where C_0, C_1, C_2 and C_3 are fitting constants for each set of aging conditions, testing temperature, and applied stress. Constant C_0 is the intercept value on the vertical axis and represents the initial (non-aged) creep strain rate. Constant C_1 represents the slope at which the secondary creep rate changes for long term aging times, and constant C2 and C3 control the nonlinear transition for small aging times. Figure 5.12 combines all of the graphs in Figure5.11 into a single three-dimensional representation of the secondary creep rate variation for aging at 100 °C for various test temperatures, stress levels, and aging times. Similar results were obtained for the other three aging temperatures, as shown in Figure 5.13.

Figures 5.12 and 5.13 show that the majority of the changes in the secondary creep rate occurs during the first 50 days of isothermal exposure, and up to a 100X reduction in the creep rate was observed. These observations were true for the various aging temperatures, testing temperatures, and stress levels. The rates of change (C_1) for long aging times are summarized in Table 5.2 for all of the testing conditions. Comparing all these values reveals that they increase with test temperature (up to 3X increase), and decrease with stress level (up to 4X decrease).

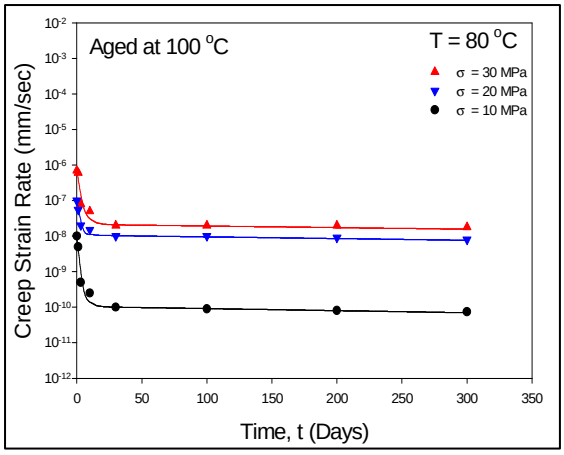

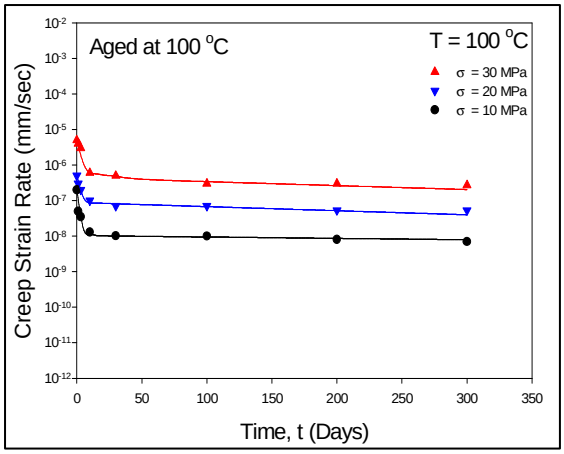

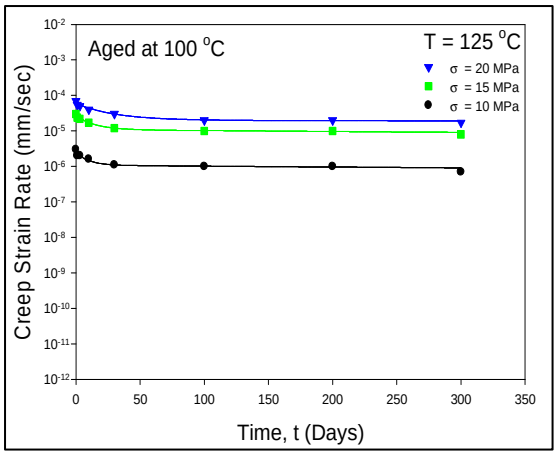

c. Tested at 125 °C

Figure 5.11 - Secondary Creep Rate vs. Aging Time (Samples Aged at 100 °C)

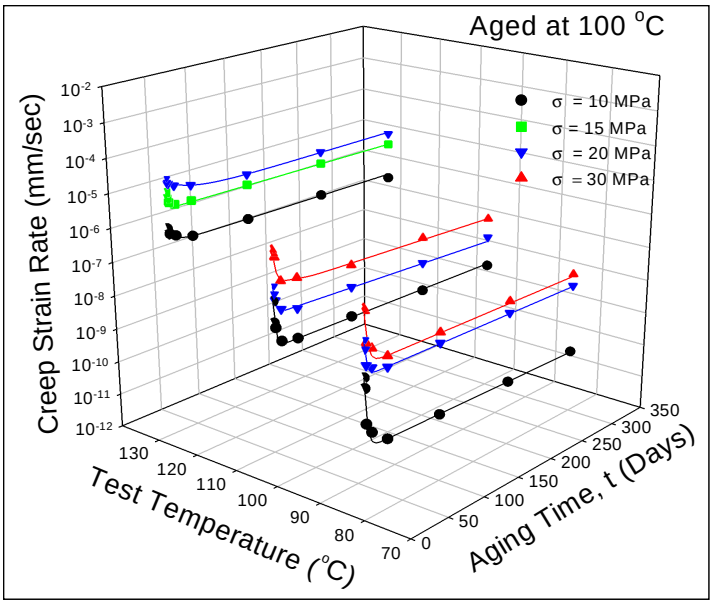

Figure 5.12 - Secondary Creep Rate vs. Aging Time (Samples Aged at 100 °C)

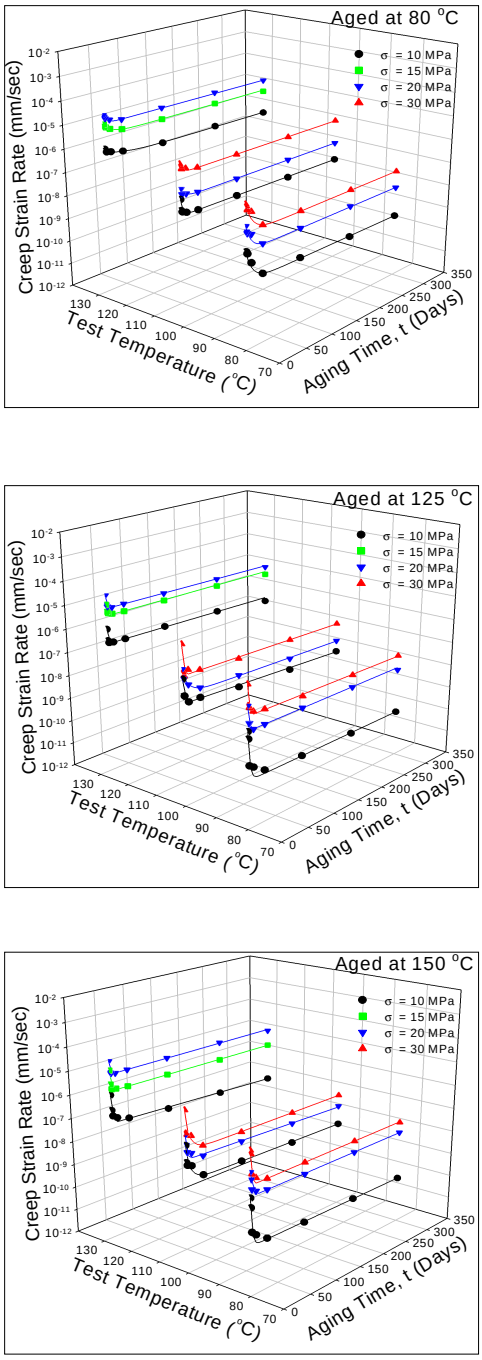

Figure 5.13 - Secondary Creep Rate vs. Aging Time (Samples Aged at 80, 125 and 150 °C)

Aging Temperature	Test Temperature	Slope (C1) of Variation of the Secondary Creep Strain Rate with Long Term Aging			
		10 (MPa)	15 (MPa)	20 (MPa)	30 (MPa)
80 °C	80 °C	-0.00054	X	-0.00036	-0.00012
	100 °C	-0.00073	X	-0.00043	-0.00037
	125 °C	-0.00086	-0.00072	-0.00065	X
100 °C	80 °C	-0.00113	X	-0.00086	-0.00037
	100 °C	-0.00146	X	-0.00111	-0.00072
	125 °C	-0.00161	-0.00127	-0.00089	X
125 °C	80 °C	-0.00160	X	-0.00130	-0.00100
	100 °C	-0.00250	X	-0.00150	-0.00140
	125 °C	-0.00270	-0.00190	-0.00160	X
150 °C	80 °C	-0.00100	X	-0.00030	-0.00026
	100 °C	-0.00130	X	-0.00110	-0.00042
	125 °C	-0.00250	-0.00120	-0.00140	X

Table 5.2 - The Slope of Secondary Creep Rate vs. Aging Time for Long Term Aging

This is likely because cross-links in the polymer matrix were weaker at higher temperatures near or above the T_g. Also, applying a higher initial holding force caused the cross-link network to change dramatically, reducing the remaining extension ability available. For test temperatures from 80 °C to 125 °C, the secondary creep rate changed by up to six orders of magnitude.

5.5 Empirical Model for the combined Effects of Aging Temperature, Aging Time, and Stress Level on the Secondary Creep Secondary Rate

In the previous section, a simple exponential relationship was proposed to describe the relationship of the secondary creep rate and aging time. In real flip chip packages, however, the temperature and stress level are essentially random. In addition to the aging effects, the secondary creep rate is a function of testing temperature, stress level, aging time, and aging temperature.

The creep models summarized in Table 2.6 all focused on using stress and testing temperature as the independent variables, and none included the effects of aging. In this section, the secondary creep rate experimental data are fitted into a single equation with multiple variables in an attempt to define a single empirical model that takes into account both aging effects and testing conditions:

$$\dot{\varepsilon} = F(T, \sigma, T_{ag}, t_{ag}) \tag{5.3}$$

where T is the testing temperature, σ is the stress level, T_{ag} is the aging temperature, and t_{ag} is the aging time.

Equation 5.3 is actually a very complicated function, with four independent variables. To address this issue, the aging effects (T_{ag}, and t_{ag}) will be considered first, followed by the testing conditions (σ and T). From Figures 5.12-5.13, the semi-log plots for the secondary creep rate

exhibit similar trends to those seen for the elastic modulus and ultimate tensile strength in chapter 4, differing only in the curve bending direction. This is probably because the material creeps less and less as it becomes stiffer and stronger with the aging process.

Because they are the semi logarithmic plots, it is proposed to model the secondary creep rate as:

$$\log \dot{\varepsilon} = C_0 + (C_1 + C_2 e^{-\frac{Q}{RT_{ag}}} t_{ag})^{-C_3} \tag{5.4}$$

where Q is the activation energy associated with the creep aging process. Following the same procedure described in the previous chapter, equation (5.4) was first fit to the secondary creep data under all aging conditions to determine single average values for Q (17800) and C_3 (0.4). The remaining parameters (C_0, C_1, and C_2) are taken to be functions of the appliled stress and testing temperature:

$$\log \dot{\varepsilon} = C_0(\sigma, T) + [C_1(\sigma, T) + C_2(\sigma, T) t_{ag} e^{-\frac{17800}{RT_{ag}}}]^{-0.4} \tag{5.5}$$

The best fits of the equation (5.5) to the creep strain rate test data are shown in Figures 5.14, 5.15 and 5.16 for aging at 80, 100, and 125 °C, respectively. The calculated dependence of parameters C_0, C_1 and C_2 on stress and temperature are shown in Figures 5.17 and 5.18. Due to the complicated dependencies, it was not attempted to establish the function forms for $C_0(\sigma, T)$, $C_1(\sigma, T)$, and $C_2(\sigma, T)$. However, it is clear from Figures 5.14-5.16 that equation (5.5) provides an accurate representation to the strain rate data.

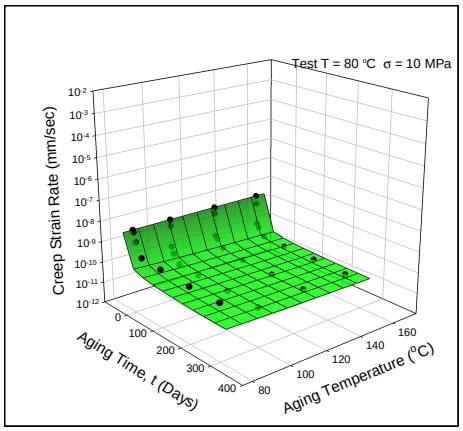

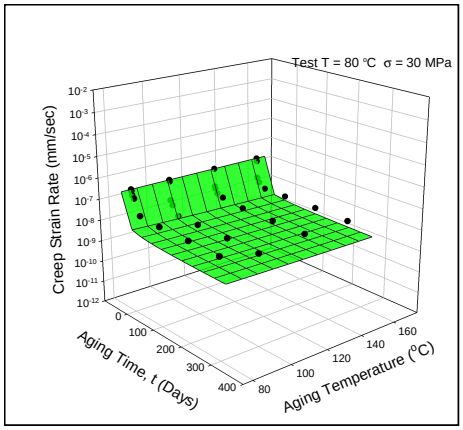

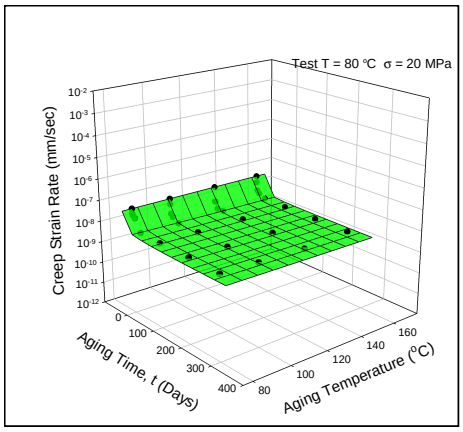

Figure 5.14 - Secondary Creep Rate vs. Aging Time (Samples Aged at 80 °C)

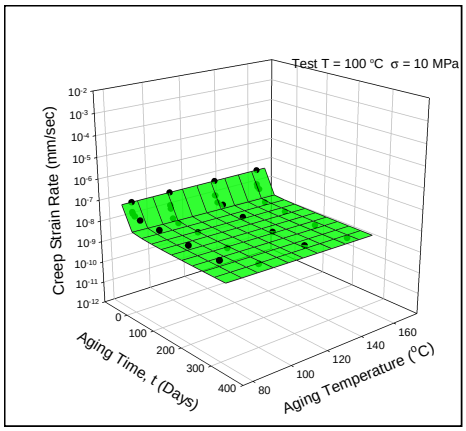

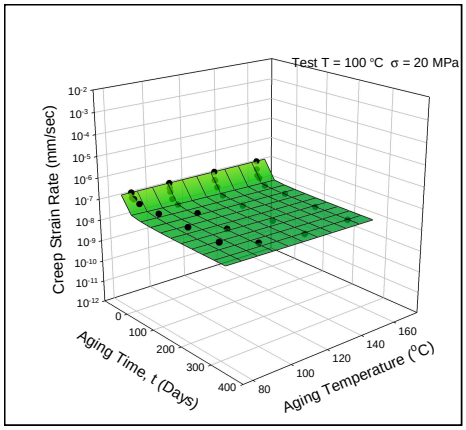

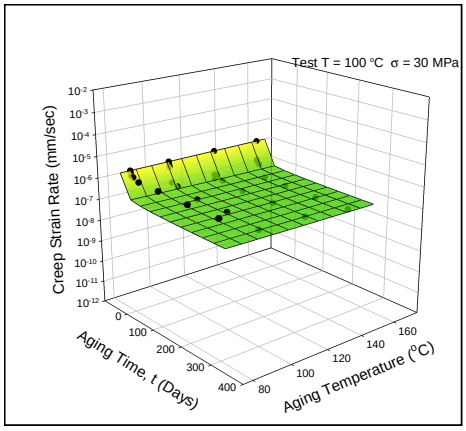

Figure 5.15 - Secondary Creep Rate vs. Aging Time (Samples Aged at 100 °C)

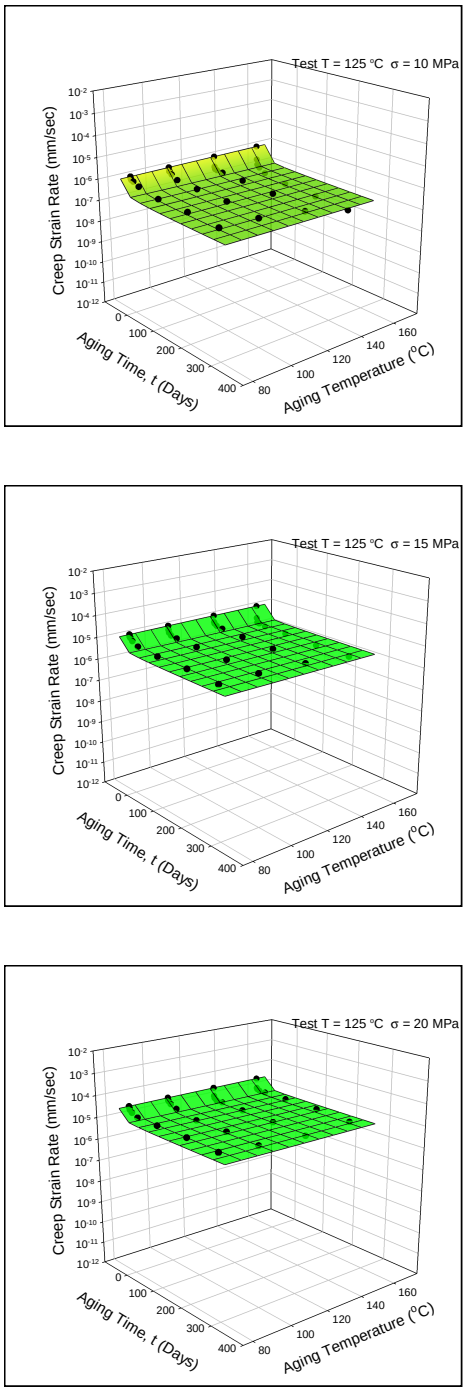

Figure 5.16 - Secondary Creep Rate vs. Aging Time (Samples Aged at 125 °C)

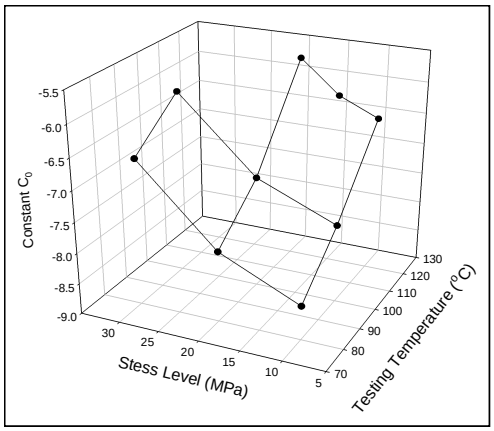

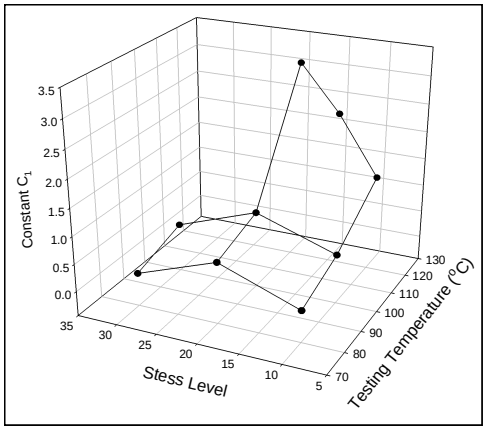

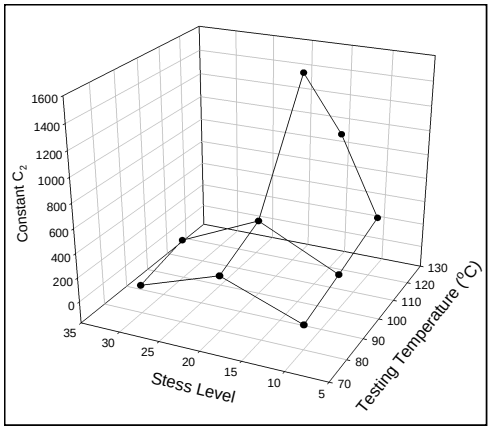

Figure 5.17 - Calculated Parameters C_0, C_1 and C_2 vs. Stress and Temperature

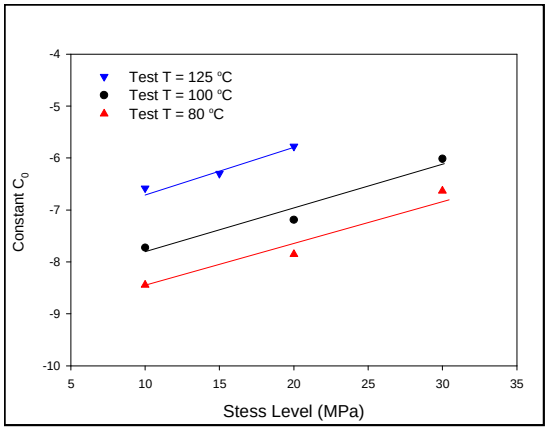

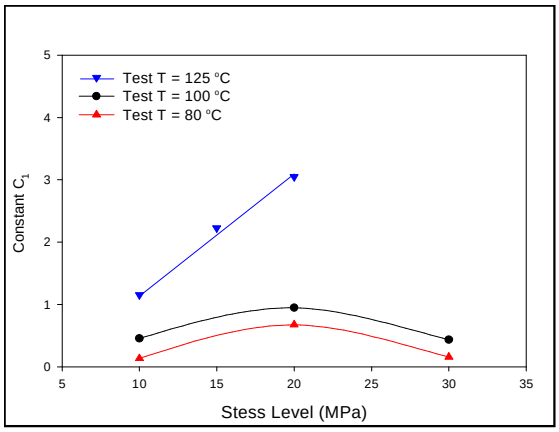

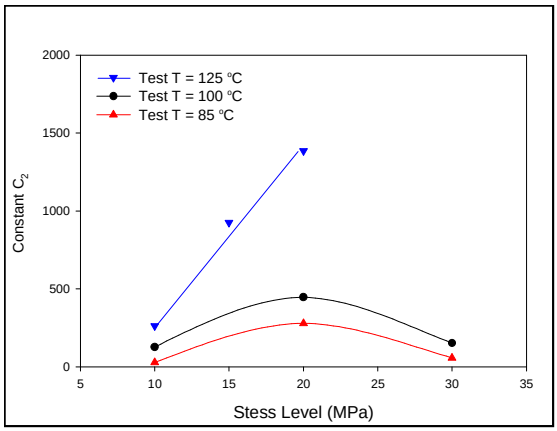

Figure 5.18 - Calculated Parameters C_0, C_1 and C_2 vs. Stress Level

5.6 Summary and Conclusions

In this chapter, a study was performed on the evolution of underfill creep behavior with isothermal aging. The recorded isochronous stress-strain curves showed that the underfill being studied was a nonlinear viscoelastic material. Thermal aging had a significant effect on the secondary creep rate, which decreased with both the aging temperature and the aging time. Up to a 100X reduction in the creep rate was observed, and the major changes occurred during the first 50 days of the isothermal aging. Also, the slope for the long term variation of the secondary creep rate changed by up to 3X with testing temperatures from 80 to 150 °C, and up to 4X with stress level changes. An empirical model was developed to describe the secondary creep rate as function of aging temperature, aging time, and stress level for a fixed testing temperature.

CHAPTER 6

CURE PROFILE EFFECTS ON THE MECHANICAL BEHAVIOR AND RELIABILITY OF FLIP CHIP ON LAMINATE ASSEMBLIES

6.1 Introduction

There has been extensive research into the properties and behaviors of epoxy materials because of their many important technical applications. Underfill manufacturers have generally focused on optimizing the curing conditions (cure time and temperature, moisture environment etc). This research has additional significance as epoxy resin cohesion obtained by the cross-linking reaction in the presence of hardeners is largely dependent on the curing conditions and the preconditioning that follows. Variations in underfill curing procedures induce different material properties and stress distributions in the assembly, thus affecting the properties and overall reliability of the packaging.

A standard epoxy formulation can absorb about 1-7 wt% moisture [52]. Other than that, a significant problem in the micro-packaging industry is the presence of moisture, which contributes to various failure mechanisms. Moisture can cause corrosion, popcorn failure, poly degradation, and hydro-stress in the packaging. The majority of contemporary underfill materials is epoxy based, and hence highly susceptible to moisture absorption as they are polar resins and thus readily interact with high polarity water molecules. Soles suggested that water enters the epoxy network through surface nanopores (5-6 Å) [53]. The weight gain by moisture

absorption under a normal lab environment is show in Figure 6.1 [54]. The moisture content reaches saturation state after 100 hours, with a weight gain of up to 0.23%.

Several research groups have investigated the effects of environmental exposures (isothermal aging with and without controlled humidity) on underfill response [29, 55-59]. These studies have primarily focused on the evolution/degradation of interfacial failure properties with duration of exposure. For example, Kuo, et al. [29] observed dramatic reductions in the interfacial (adhesion) strength of underfill and soldermask interfaces in lap shear specimens that had been exposed to a combination of humidity and temperature (60 °C and 95% RH for 168 hours) (Figure 6.2). The fracture strengths decreased by 33% in non-solder mask flip chips, whereas the fracture strengthen decreased by up to 50% for solder mask defined flip chips.

The focus of interfacial failure can be shifted from the upper to the lower FR4/solder mask as a result of the environmental preconditioning utilized. Kuo, et al. [29] also demonstrated changes in the constitutive behavior of their lap shear specimens after thermal/humidity aging by observing fracture surfaces for various displacement rates, preconditioning conditions and specimen types.

Studies by Ferguson and Qu [55, 56], revealed that exposures to various combinations of humidity and temperature (e.g. 85 °C and 85% RH for 168 hours) had only a negligible effect on the elastic modulus of their epoxy samples once the current conditions of the samples had been equilibrated by dry baking. However, the samples' interfacial toughness was shown to drop with duration and severity of environmental exposure, including exposure to 85 °C with no moisture (dry heat).

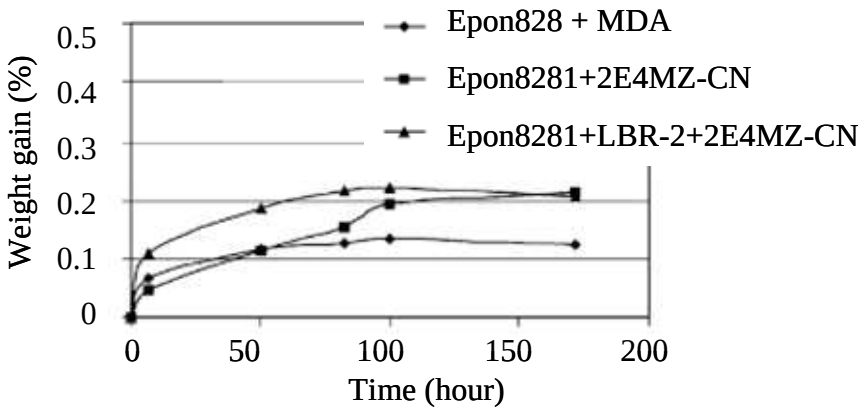

Figure 6.1 - Moisture Absorption of Underfill under Normal Lab Environment (Sample Thickness: 2 mm) [54]

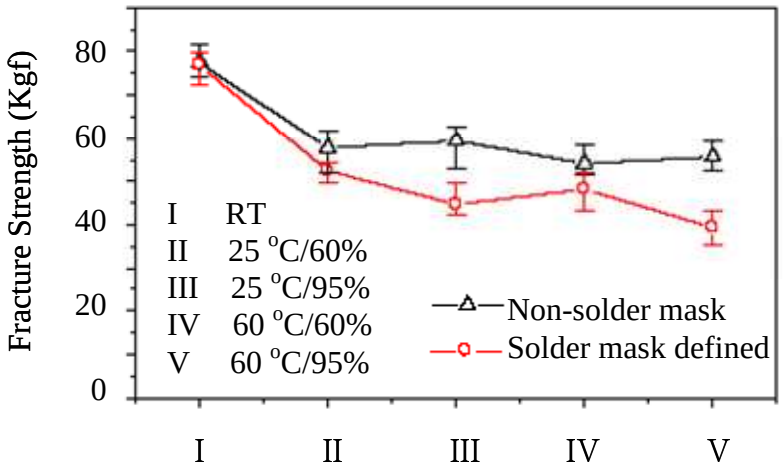

Figure 6.2 - Fracture Strength as a Function of Different Displacement Rate, Preconditioning Condition and Specimen Type [29]

Similar results were observed by Luo and Wong [12, 57], who found that thermal cycling had no effect on the inherent adhesion strength between the underfill and the passivation layer. The interfacial strength in special mechanical testing specimens was degraded with duration under thermal/humidity aging conditions of 85 °C and 85% RH (85/85). The adhesion strength became steady after 96 hrs of 85/85 aging, although the moisture absorption reached saturation after 20 hrs, as shown in Figures 6.3 and 6.4. The degradation of adhesion strength was ascribed mainly to a decrease in the underfill modulus, which was itself linked to the liquid accumulating on the interface. In another approach, Zhang and co-workers [59] measured crack opening displacements to characterize the changes in stress intensity and foundnterfacial cracking along the underfill and silicon chip passivation interface served as a function for both dry and moist condition aging at 85 °C. Finally, the author' group have measured the effects of various types of preconditioning (JEDEC and MSL3) and cure profiles on the stress-strain behaviors and mechanical properties of underfills, as well as the reliability of flip chip assemblies [58].

The influence of underfill aging on the performance of electronic assemblies has also been investigated by several groups [11, 60, 61]. Chaware, et al. [60] have shown that three weeks dry aging at 85 °C had little effect on the reliability of flip chip assemblies made with several different underfills. However, combined hydrothermal exposures at 85 °C and 85% RH had a significant effect on all the configurations examined: both underfill fillet cracking and passivation interface delaminations at the underfill were accelerated during thermal cycling testing. Okura, et al. [11] modeled the same configurations, and proposed that the new failure modes were created as a result of hydro-mechanical swelling. Wong and co-workers [61] studied failures occurring in flip chip assemblies during elevated temperature aging exposures,

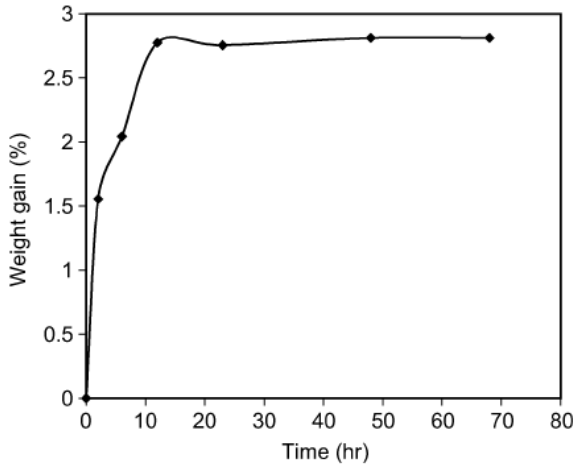

Figure 6.3 - Moisture Absorption of a 2 × 2 × 50 mm Long Orthogonal Bar of G25 Underfill during 85/85 Aging [57]

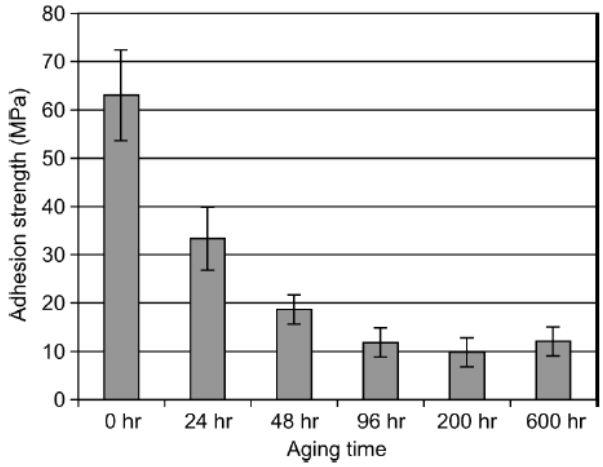

Figure 6.4 - Adhesion Strength of G25 on SiN vs. Aging Time [57]

and compared the results at different temperature levels. They suggested that stress corrosion and debonding at the under-fill-die interface was responsible for the observed exponential difference in the life at 85 °C/85% RH compared to that at 120 °C/100% RH aging. The underfill material curing temperature may well prove to be the simplest and most effective method to improve moisture resistance and autoclave performance.

Dimke [62] examined the effects of the underfill material's cure temperature on adhesion strength, and concluded that higher cure temperatures resulted in better adhesion. In this work, a 2.5 x 2.5 mm die with bumps was adhered to substrates with capillary flow underfills and shear tests were performed. A possible drawback in the method used for this study was that there was some fillet formation along the dispensing edge, so the die shear force measurements were not solely measuring the interfacial adhesion, but also contributions from the underfill fillet.

The size of the shift needed to align the individual experimental data for specific testing temperatures was generally described by the Williams-Landel-Ferry relationship (WLF): As discussed above, prior investigations have concentrated on the effects of thermal (dry) and isothermal aging on the failure properties of both underfills and assemblies with underfill. However, few studies have explored the effects of aging on the material constitutive behavior of underfills (e.g. stress-strain and creep behaviors).

6.2 Objectives

In this chapter, the effects of underfill cure temperature and JEDEC MSL preconditioning on underfill mechanical and strength properties, as well as flip chip assembly reliability, are explored. Baseline stress-strain curves, mechanical properties, and interfacial shear strengths of a capillary underfill were recorded for samples cured at 150 °C and 165 °C (30 minutes). In

addition, changes in the mechanical and strength properties resulting from MSL3 and MSL2 preconditioning were also evaluated. The MSL preconditioning of the underfill samples included the JEDEC specified humidity and temperature exposures, with three simulated reflows at 245 °C or 260 °C.

Thermal cycling life tests from -55 to 125 °C were also conducted on daisy chain flip chip assemblies incorporating the same underfill. The test matrix for the reliability test included both 150 °C and 165 °C curing profiles, and two levels of preconditioning (none, MSL3). Finally, the failure mechanisms in the flip chip assemblies were studied using CSAM, x-ray and SEM analyses.

6.3 Experimental Procedures

The commercially available underfill utilized in this work was the silica filled epoxy UF1 described in earlier chapters. The underfill mechanical/shear test specimens and the underfilled flip chip assemblies were prepared with two different curing profiles consisting of a 30 minute isothermal exposure at either 150 °C or 165 °C in a box oven.

After curing, but before testing, various groups of samples were preconditioned to several different JEDEC standard, MSL and humidity levels, with the case of no preconditioning serving as the control group. The preconditioning exposures consisted of a timed exposure at fixed temperature and humidity, followed by a three solder joint reflow temperature profile. Table 6.1 summarizes the notations and conditions applied for the various sample preconditioning exposures used in the work reported here.

For each of the two curing temperatures, groups of test specimens were subjected to no preconditioning, humidity, or MSL3+245 with three time exposures. The reflow process

Preconditioning Nomenclature	Environmental Exposure	Reflow Profile Exposures
None	None	None
Humidity	30 °C and 60% RH for 192 hours	None
MSL2+245	85 °C and 60% RH for 168 hours	245 °C Peak 3 Exposures
MSL2+260	85 °C and 60% RH for 168 hours	260 °C Peak 3 Exposures
MSL3+245	30 °C and 60% RH for 192 hours	245 °C Peak 3 Exposures
MSL3+260	30 °C and 60% RH for 192 hours	260 °C Peak 3 Exposures

Table 6.1 - Sample Preconditioning Exposures

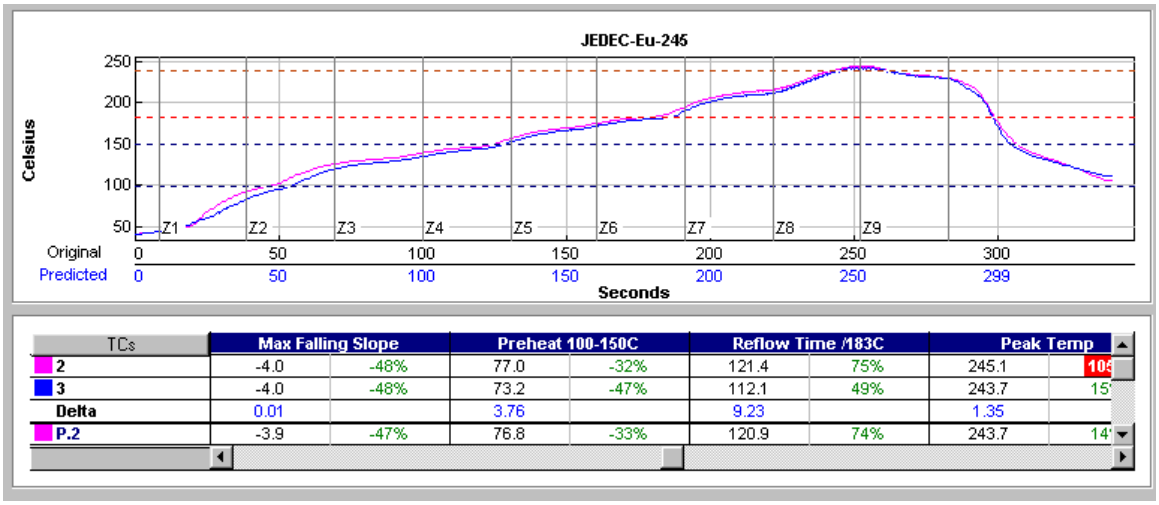

Figure 6.5 - The MSL3 + 245 Reflow Process Temperature Profile

temperature profile is shown in Figure 6.5. Stress-strain tests were then performed with samples from the various specimen sets with several different temperature settings: -55, -25, 0, +25, +85, +125, and +150 °C. For each set of test conditions (sample curing temperature, sample preconditioning, and test temperature), six stress-strain tests were performed.

6.4 Experimental Shear Strength Measurements

Interfacial de-adhesion occurs on the interface between two contacting materials, and the interfacial strength depends on the chemical and mechanical properties of the interfaces. Shear strength is characterized in terms of the interface fracture toughness, which is the maximum mechanical work transferred across the interface before the separation. In electronic packaging, interface failures can occur at either the die or the substrate, and delaminations are a common failure mode.

Adhesion is difficult to measure in general, and especially problematic on samples that simulate real manufacturing environments, which must take into account potential problems due to process contamination, flux residue, reflow temperature, and so on. However, a good understanding of the fundamental process involved for materials and interfaces, in this case interfacial shear strength adhesion tests, can still be useful. The measured shear strength at the die/underfill interface of a typical underfill flip chip is a combination of shear force and the energy required to break the fillet. Consequently, shear strength is the energy required to rupture the chemical bonds formed in die passivation and at the underfill interface. Chemical bonds with the fillets may be formed at the edge of the die during the underfilling process. Therefore, care should be taken to eliminate the contribution from the fillets if possible.

The method utilized in this work for shear force application is illustrated in Figure 6.6. The height of the underfill material was about 4μs after the solder ball joints collapsed. Force was applied to the side of the chip, and was transmitted to a cylindrically shaped underfill region adhered to both the die passivation layer and the topside of the PCB. The solder balls were not attached or reflowed to the printed circuit board, but instead used to provide a fixed stand-off distance of approximately 125 μm.

To assemble these samples, a bare FR4 laminate strip without soldermask and with planar dimensions of 100 x 25 mm was first dehydrated for 24 hours at 125 °C before assembly. The FR4 strip was then placed on the stage (unheated) of a CAM/ALOT 3700 dispensing system. Ten underfill dots were dispensed, each of which had a diameter of approximately 2 mm. A bumped test chip (5 x 5 mm with 88 I/O) was centered and placed on top of each underfill dot using an automatic pick and place machine with a placement force of 2.94 N. The underfill dots in the shear force testing specimen were then cured in box oven for 30 minutes under either the 150 °C or 165 °C curing profile. Several test coupons were assembled with each curing temperature. For the 165 °C cure cycle, some samples were also exposed to each of the five preconditioning exposures listed in Table 1.

The die shear tests were performed using a Dage 2400 System with a loading head speed of 50.8 μm/sec and the force range of 1 N. A microscope was used to align the die edge, which had to be parallel to the shear blade to ensure the applied force was uniform along the die edge.

The assembled test coupons are shown in Figure 6.7, which shows the samples both before and after die attaching. The 5 x 5mm dies were attached to the PCB by a single drop of underfill material. Two primary failure modes were observed: adhesive failure at the interface

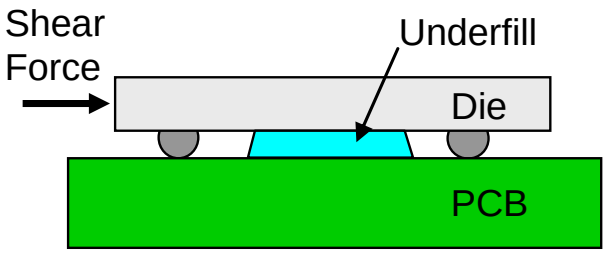

Figure 6.6 - Schematic of the Underfill Adhesion Shear Test

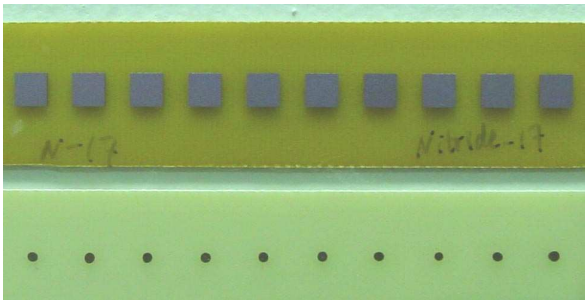

Figure 6.7 - Assembled Shear Test Coupons Before and After Die Attaching

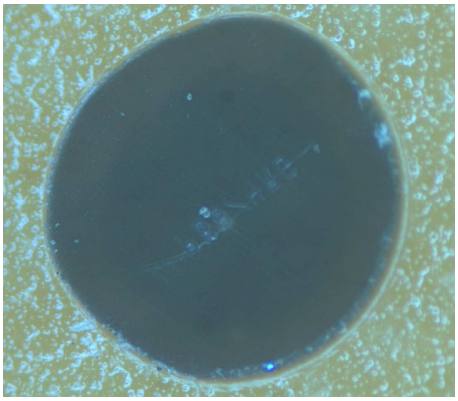

Figure 6.8 - Cured Underfill Dot After Shear Test

between die passivation and underfill or adhesive failure interface between the PCB and underfill. Figure 6.8 shows the dot remaining of a typical underfill after die passivation and underfill interfacial failure. The original spherical shape of the underfill dot was distorted after the shear test.

6.5 Thermal Cycling Reliability Tests

Fatigue failures occur with the initiation of a microscopic crack and at much lower stress due to accumulation damage when subjected to the thermal cycling process. The crack can continue to propagate steadily steady until the initial crack becomes unstable under cyclic stresses. Fatigue failure is one of the most commonly encountered problems in the electronic packaging design industry. However, packaging reliability can be improved by better understanding the crack propagation mechanism.

Thermal cycling reliability tests were performed over a range from -55 to +125 °C in a single compartment environmental chamber. The PB8 daisy chain test chips used for this experiment had dimensions of 5 x 5 mm and featured a single row of 88 perimeter 63Sn-37Pb eutectic solder bumps on an 8 mil (200 μm) pitch. Each test board contained 10 test chips, and individual daisy chains were monitored during thermal cycling.. The in-plane dimensions of the test boards were 135.9 x 88.9 x 1.25 mm, and they were fabricated using FR-406 laminates with copper traces and an electroless Nickel immersion Gold finish. The test boards were assembled on the SMT Line at Auburn University.

Prior to placement, the test chip solder balls were dipped into Kester TSF 6522 tacky, no-clean solder flux with a 20-30 μm shim thickness. The dies were then aligned and placed on the test substrates using a high speed pick and place machine with a placement force of 2.94 N.

Reflow was performed in a Nitrogen atmosphere in a Heller EXL1800 reflow oven using a reflow profile with a peak temperature of 220 °C. The underfill was dispensed using a 25 gauge needle onto a heated substrate. The stage temperature was 105 °C, leading to an actual substrate temperature of approximately 95-100 °C. A corner dot dispense pattern was used, and the underfill was cured in a box oven for 30 minutes using either a 150 °C or 165 °C cure profile. Before reliability testing was conducted, some of the boards cured under different temperatures were also subjected to MSL3+245 preconditioning. A photograph of a fully populated test board is shown in Figure 6.9, while a photograph of a typical die mounting site is shown in Figure 6.10.

C-mode scanning acoustic microscopy (CSAM) and x-ray analyses were performed on all test boards after assembly. These procedures were done in order to inspect for manufacturing defects and underfill delaminations. The assembled parts were then subjected to thermal cycling. Monitoring the various daisy chain networks was performed throughout the cycling process using a high accuracy digital multimeter coupled with a high performance Labview controlled switching system. The resistance of each daisy chain was recorded during thermal cycling, and opening was treated as assembly failure.

The failure data were statistically analyzed using two parameter Weibull models. The standard parameters used for these models are the Weibull Slope β, and the Characteristic Life η, which is the number of cycles required to cause failure of 63.2% of the samples from a particular leg of the test matrix. From these values, a particular configuration in the test matrix, the cumulative failures (percent) after any number of thermal cycles can be calculated. Failure analyses of cycled test boards were conducted using CSAM, x-ray, and scanning electron microscopy (SEM) of cross-sectioned parts.

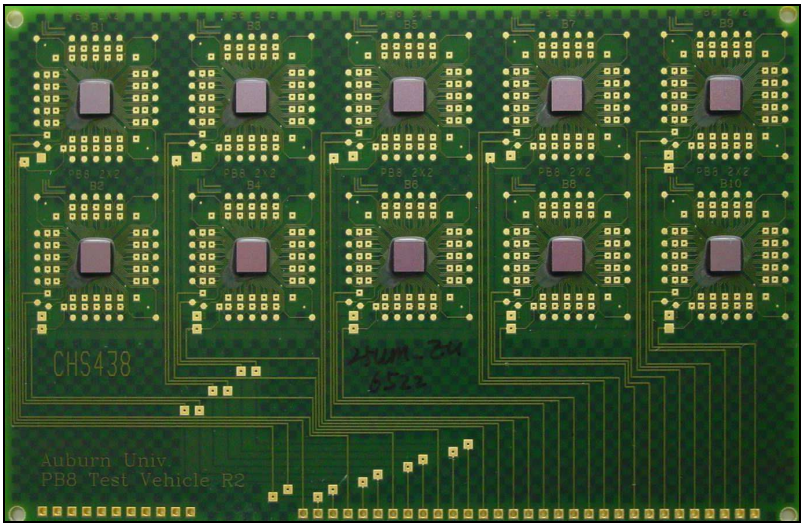

Figure 6.9 - Flip Chip Thermal Cycling Test Board

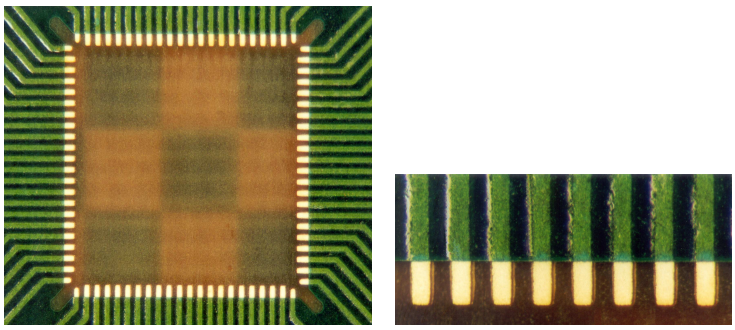

(a) (b)

Figure 6.10 - (a) Die Site (b) Finger Design for I/O

6.6 Experimental Results

6.6.1 Mechanical Testing of Underfill Material

The average temperature dependent stress-strain curves for the specimens cured at 150 °C and 165 °C (no preconditioning) are shown in Figure 6.11. The range of the maximum strain of the average curve for each temperature was found by averaging the failure strains from each of the six tests used in the regression fit for that temperature. Figure 6.12 shows direct comparisons of the corresponding stress-strain curves at T = -55, +25, +85, +125, and + 150 °C for these two curing conditions.

In Figure 6.12, the solid lines are for the specimens cured at 165 °C and the dashed lines are the specimens cured at 150 °C. It can be observed qualitatively that the stress-strain curves are shifted towards the left and upward by increasing the curing temperature under the same test temperature, which means that the effective modulus increases when reached via the higher 165 °C curing temperature. This trend can also be applied to the UTS.

These observations are confirmed by the plots in Figure 6.13, where the E and UTS values are plotted as a function of testing temperature. When the testing temperature is above 100 °C, there are only slight differences in the mechanical properties of underfills formed with the two curing temperatures. In this case the test temperatures are close to or above the glass transition temperature (T_g). From these phenomena, the glass transition region can be determined by rapid degradation of the mechanical properties, even though the exact T_g temperature cannot be determined by the tensile test. However, for T lower than room temperature, the differences are significant. At T = -55 °C, the material property UTS is

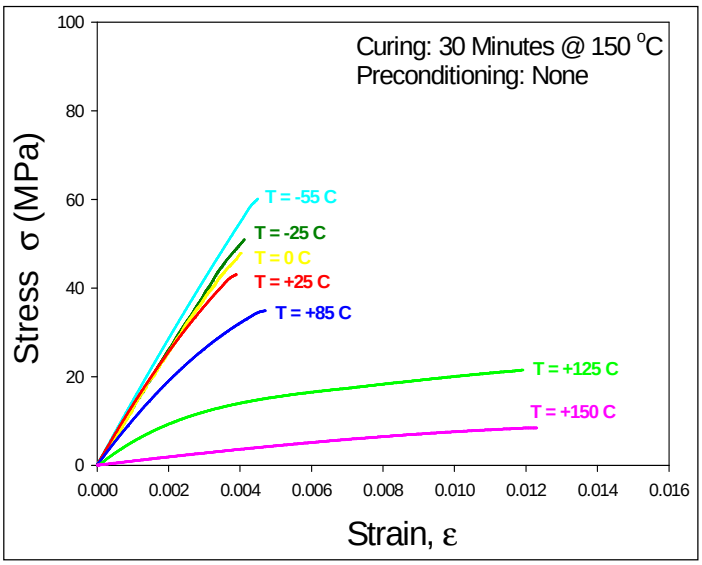

(a) Curing at 150 °C

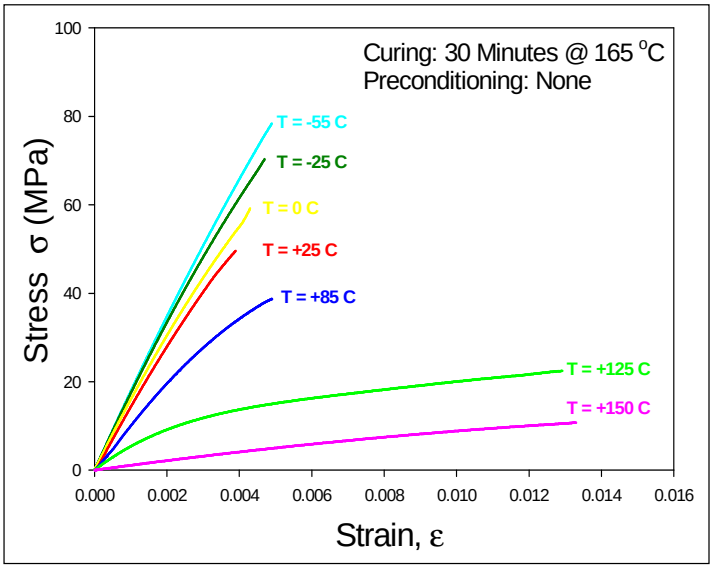

(b) Curing at 165 °C

Figure 6.11 - Underfill Stress-Strain Curves for Curing at 150 °C and 165 °C (No Preconditioning)

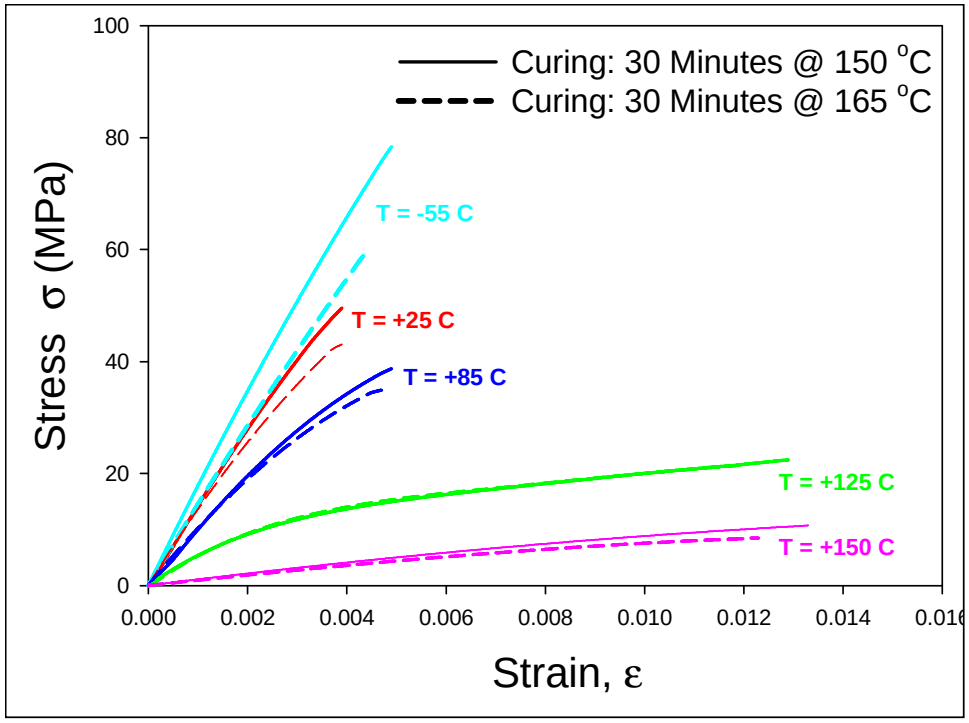

Figure 6.12 - Comparison of Stress-Strain Curves for Curing at 150 °C and 165 °C (No Preconditioning)

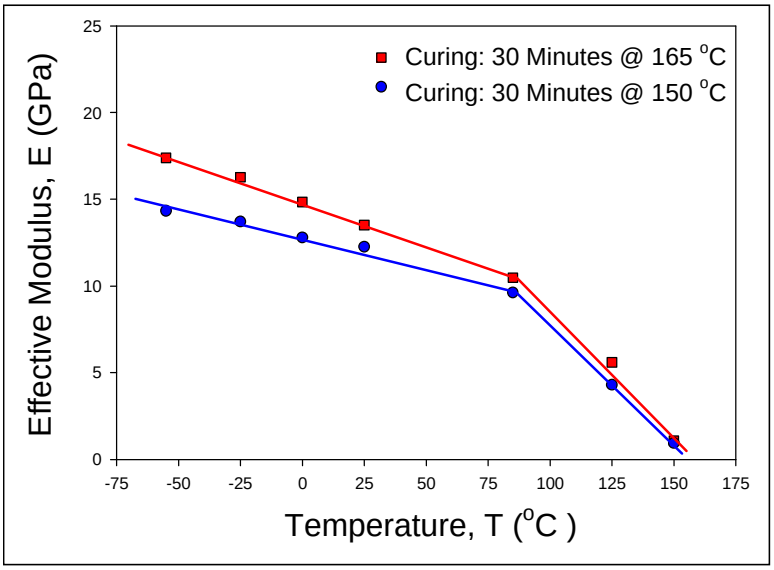

(a) Effective Modulus vs. Temperature

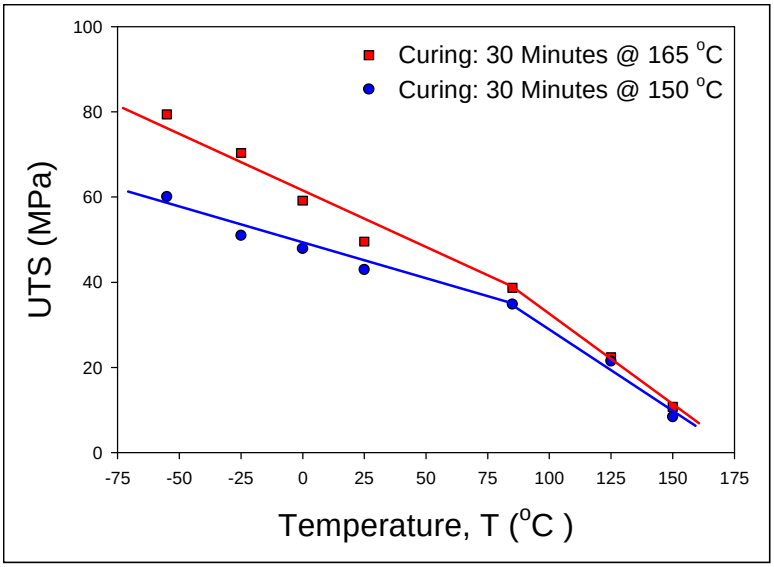

(b) Ultimate Tensile Strength vs. Temperature

Figure 6.13 - Mechanical Properties Comparisons for Underfill with Two Cure Conditions (No Preconditioning)

approximately 30% higher compared to underfill cured at 165 °C, with an elastic modulus about 25% higher. These increases are due to the higher density of epoxy cross-linking obtained during the higher temperature cure procedure. The degree of cross-linking increases with the extent of cure for the partially cured epoxy resin.

Regarding the effect of moisture, the average temperature dependent stress-strain curves for the specimens cured at 150 °C and 165 °C, and then subjected to MSL3+245 preconditioning are shown in Figure 6.14. The corresponding curves for the un-preconditioning case are also included for the purpose of comparison.

Similarly, MSL preconditioning significantly raised the UTS at temperatures below 100 °C, while little or no change was observed in the effective elastic modulus E at any temperature. Plots directly illustrating the effects of the MSL preconditioning on the E and UTS as a function of temperature are shown in Figure 6.15. At T = -55 °C, the UTS was approximately 32% higher after the moisture MSL3+245 per-conditioning for specimens cured at 150 °C, whereas UTS was about 25% higher after the moisture per-conditioning for specimens cured at 165 °C. It is interesting to see this phenomenon because normally the moisture degrades the material properties but this is not the case for this type of underfill material.

Figure 6.16 summarizes the pre-conditioning effects on mechanical properties, elastic modulus and ultimate tensile strength for underfill materials cured at 150 °C. From the bar plots, the elastic modulus dropped as a result of humidity pre-conditioning (30 °C and 60% RH for 192 hours), then increased after the reflow process (MSL3+245), although all these changes were small, at less than 5%. The ultimate tensile strengths increased monotonically with humidity and MSL3+245 pre-conditioning, and these changes are profound, with an increase of about 30%.

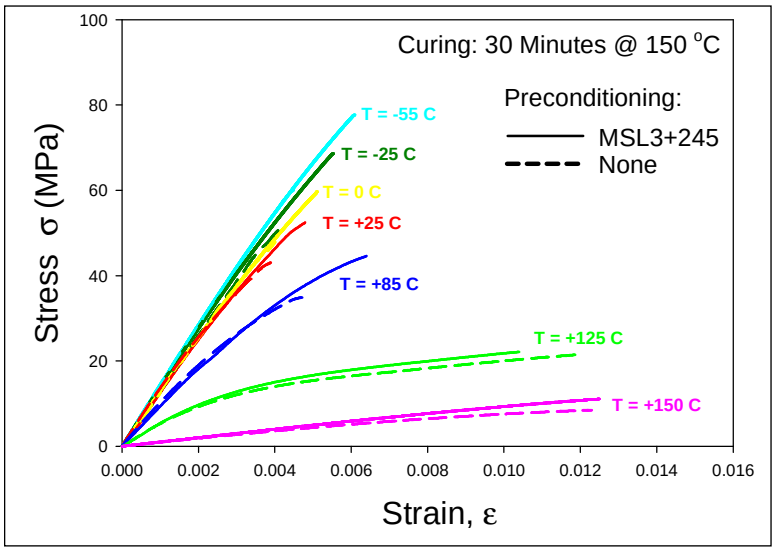

(a) Curing at 150 °C

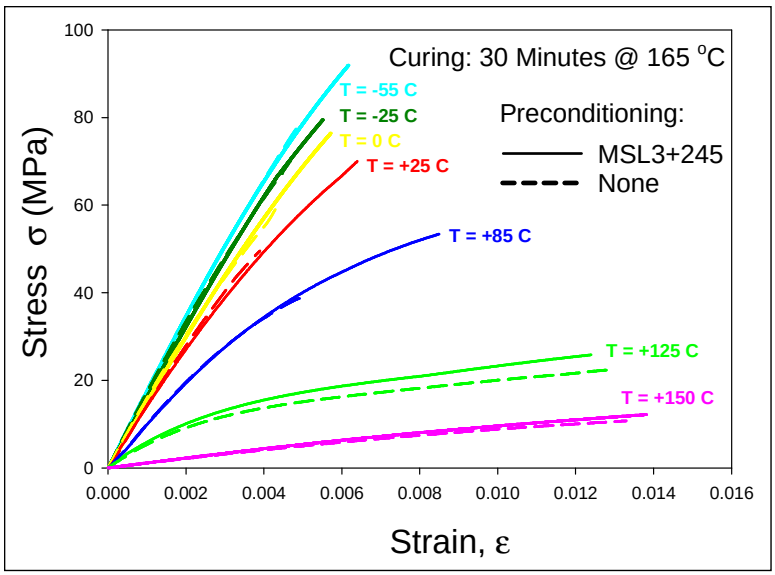

(b) Curing at 165 °C

Figure 6.14 - Underfill Stress-Strain Curves for Curing at 150 °C and 165 °C (MSL3+245 and No Preconditioning)

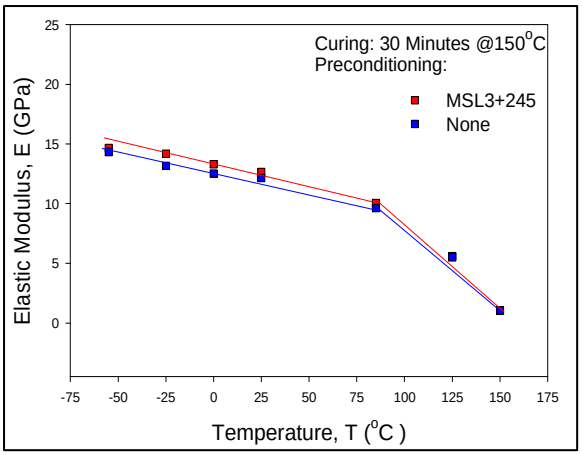

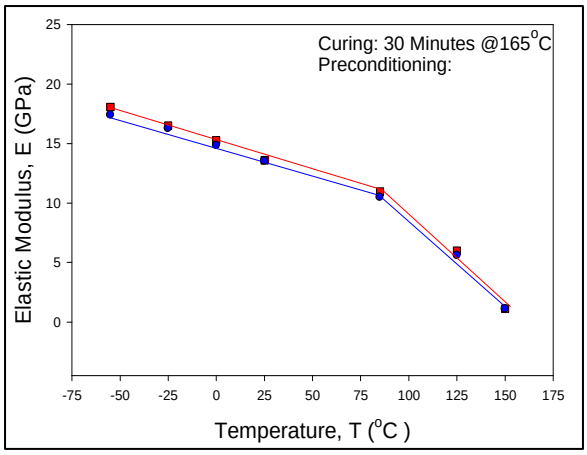

(a) Effective Modulus vs. Temperature

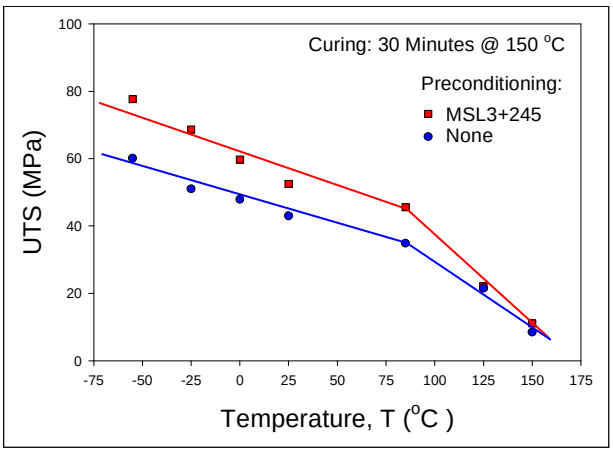

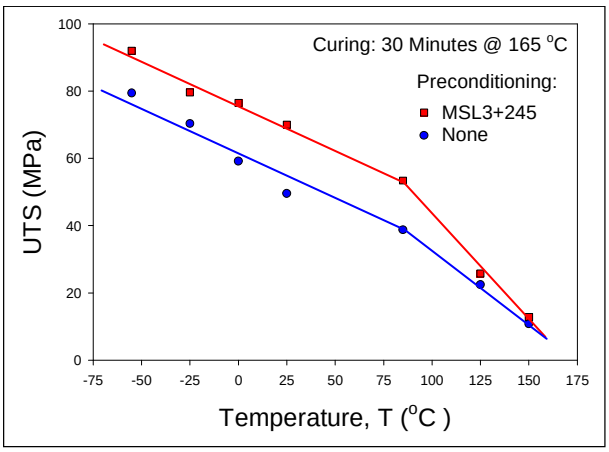

(b) UTS vs. Temperature

Figure 6.15 - Mechanical Properties vs. Temperature for Samples with and without MSL3+245 Preconditioning

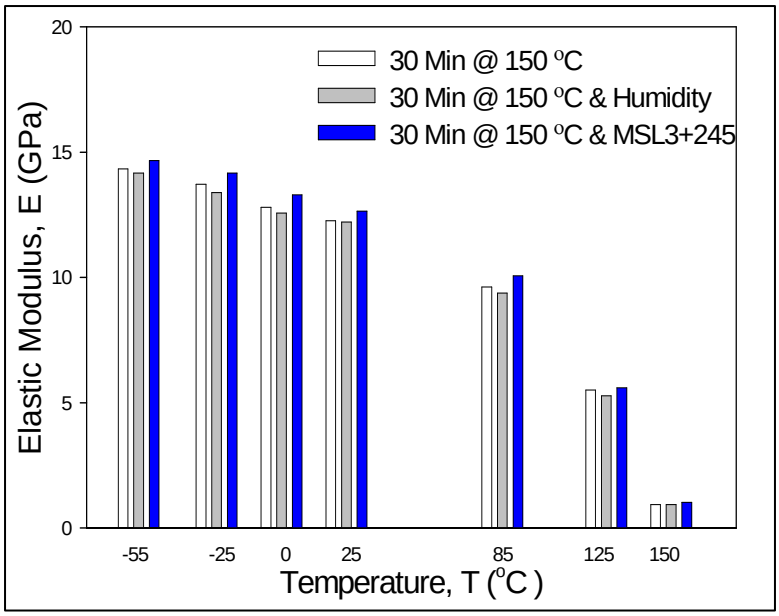

(a) Effective Modulus vs. Pre-conditioning Procedures

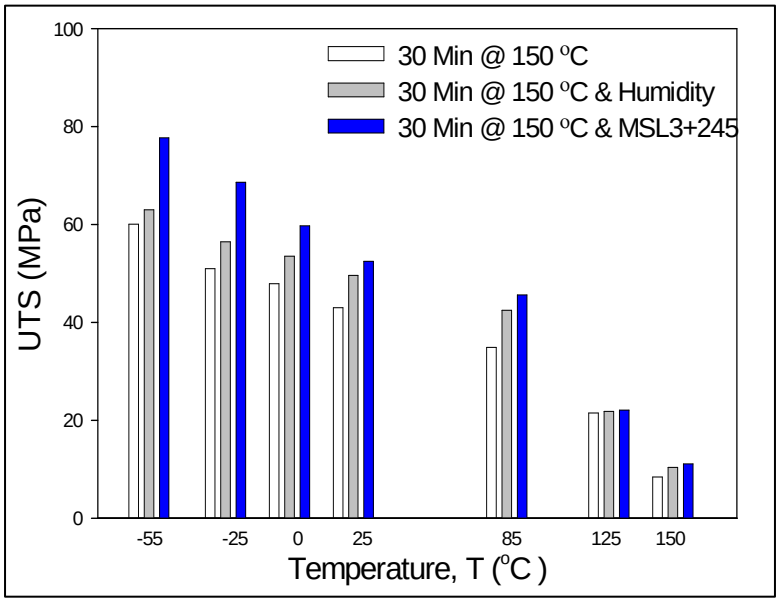

(b) UTS vs. Pre-conditioning Procedures

Figure 6.16 - Mechanical Properties vs. Temperature for Samples with the Different Preconditioning

Based on these findings, we can conclude that the samples cured at 165 °C exhibited significantly increased effective elastic modulus and ultimate tensile strength. Moreover, MSL3 preconditioning had only a minor effect on the effective elastic modulus, but significantly improved the ultimate tensile strength. The results of the interfacial shear strength tests demonstrated slight variations between strength with preconditioning, but significant shifts in the location of the shear failures to the underfill-substrate interface for the 165 °C cured samples.

6.6.2 Shear Strength

The average measured shear strengths for samples prepared with the two cure conditions (no preconditioning) are shown in Figure 6.17. Interfacial adhesive failures were observed at both the underfill to die passivation and underfill to PCB interfaces. The percentages of the samples failing at the die passivation interface are also indicated. With the higher cure temperature of 165 °C, it was observed that the shear strength dropped slightly. However, the higher cure temperature also led to 45% fewer failures at the underfill to die passivation interface; instead, the failures tended to shift toward the underfill to PCB interface when using the higher cure temperature. Therefore, one might conclude that using a higher cure temperature enhances the adhesion at the underfill to die passivation interface.

The effects of MSL preconditioning on the shear strength were also studied for the cure temperature of 165 °C. Figure 6.18 illustrates the average measured shear strengths for samples subjected to the five different preconditioning exposures listed in Table 6.1. Once more, the failure modes consisted of interfacial adhesive failures at both the underfill to die passivation and underfill to PCB interfaces. Both MSL2 preconditioning exposures (MSL2+245 and MSL2+260) reduced the shear strength but increased the percentage of samples failing at the

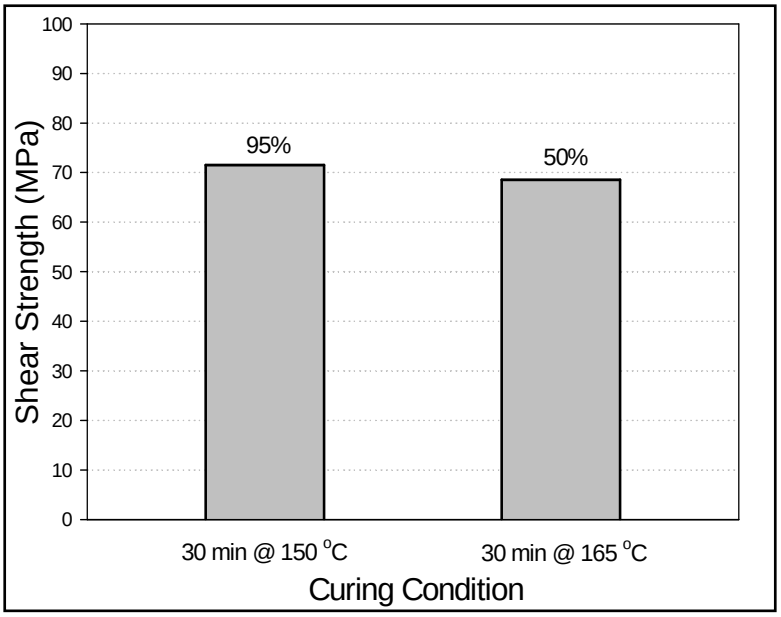

Figure 6.17 - Average Shear Strength vs. Cure Temperature (The Percentage Indicates the Portion of the Failures Occurring at the Underfill to Die Passivation Interface)

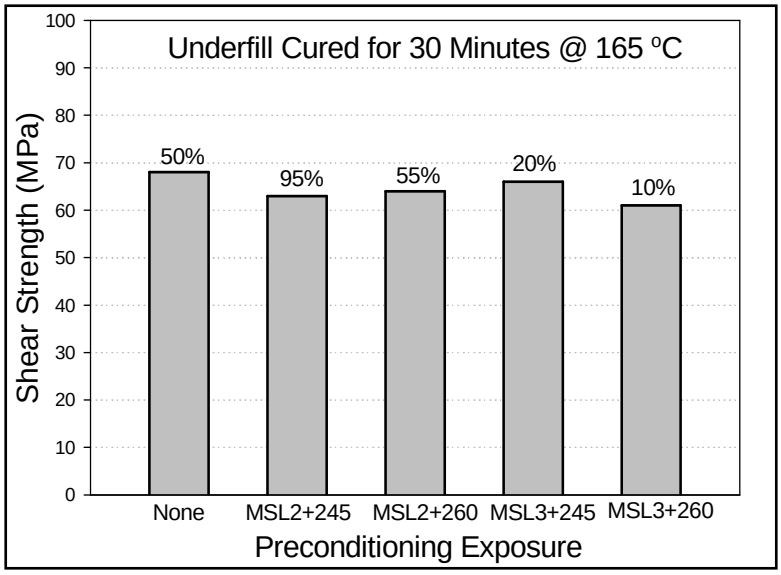

Figure 6.18 - Average Shear Strength vs. Preconditioning (The Percentage Indicates the Portion of the Failures Occurring at the Underfill to Die Passivation Interface)

underfill to die passivation interface. Thus, MSL2 preconditioning was generally detrimental to the adhesion of the underfill. For the two MSL3 preconditioning exposures, the strength levels dropped slightly. However, the failure location then shifted to the underfill to PCB interface, which suggests that the adhesion to the die passivation interface actually increased.

6.6.3 Thermal Cycling Reliability Tests

The thermal cycling test matrix consisted of four different underfill curing and preconditioning configurations:

- Curing at 150 °C, No Preconditioning
- Curing at 165 °C, No Preconditioning
- Curing at 150 °C, MSL3+245 Preconditioning
- Curing at 165 °C, MSL3+245 Preconditioning

Three test boards were assembled for each configuration, and 28-30 functional daisy chain dies with no delaminations were available before preconditioning and thermal cycle test. After preconditioning at MSL3+245 but before thermal cycling, delaminations at the underfill to die passivation interface were discovered in some of the samples cured at 150 °C, while no delaminations were presented in the MSL preconditioned samples cured at a cure temperature of 165 °C. No solder joint failures occurred in any of the test chips during assembly preconditioning.

Of the 30 test chips in the set cured at 150 °C and with MSL+245 preconditioning, 4/30 experienced full delaminations and 15/30 showed slight delaminations after preconditioning. Thus, approximately 65% of the samples in this test contained delaminations before thermal cycling. These initial interfacial flaws obviously placed this testing group at a severe

disadvantage from the reliability standpoint. Figure 6.19 depicts the CSAM images showing delaminations in the preconditioned samples cured at 150 °C.

The Weibull failure plots (electrical opens) for the four test configurations are shown in Figure 6.20. The calculated Weibull slope, characteristic life (cycles to 63.2% failure) and one percent life ($N_{1\%}$, cycles to 1% failure) are tabulated in Table 6.2. As expected, the samples cured at 150 °C with MSL3+245 preconditioning performed poorly due to the initial delaminations present.

The data clearly indicate that the samples assembled at a cure temperature of 165 °C were significantly more reliable than those cured at a temperature of 150 °C. The MSL3+245 preconditioning also appeared to increase the reliability of the samples cured at 165 °C. Other factors that contributed to enhancing sample reliability included the increase in UTS (see Figure 6.16) with preconditioning, as well as the change in location of the interfacial shear failures when the samples were preconditioned (see Figure 6.18).

6.6.4 Microstructures

SEM photos of the cross-sectioned solder joints after thermal cycling are shown in Figures 6.21(a) and 19(b) for the cases of underfill curing at 150 °C with no preconditioning and with MSL3+245 preconditioning, respectively. Complete solder joint cracking is seen in the no preconditioning case, while extreme underfill to die interfacial cracks and complete solder joint cracking are observed for the MSL3+245 preconditioning sample.

Analogous SEM photos for the 165 °C cured samples are also shown in Figure 6.22. Limited solder joint cracking was observed for both cases of preconditioning, even after more than 6500 thermal cycles.

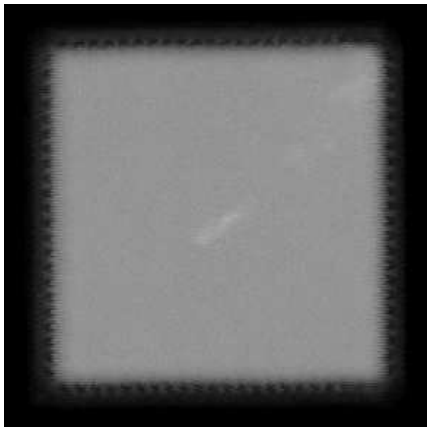

(a) No Delaminations

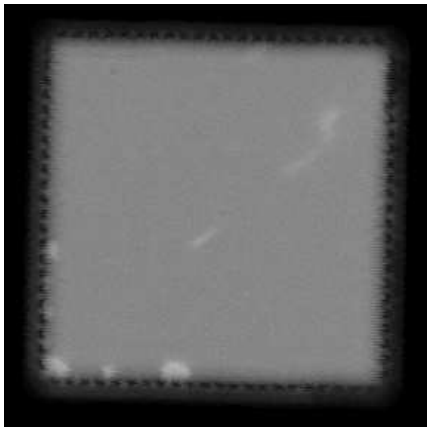

(b) Slight Delaminations

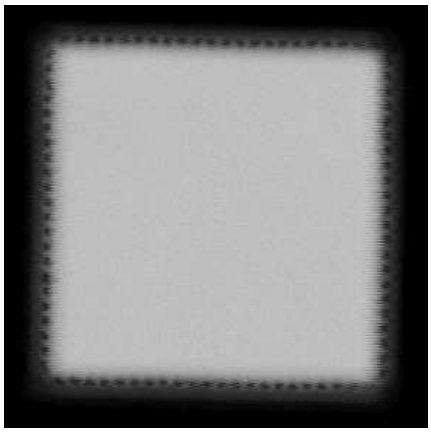

(c) Fully Delaminated

Figure 6.19 - CSAM Images of Samples Cured at 150 °C After MSL3+245 Preconditioning

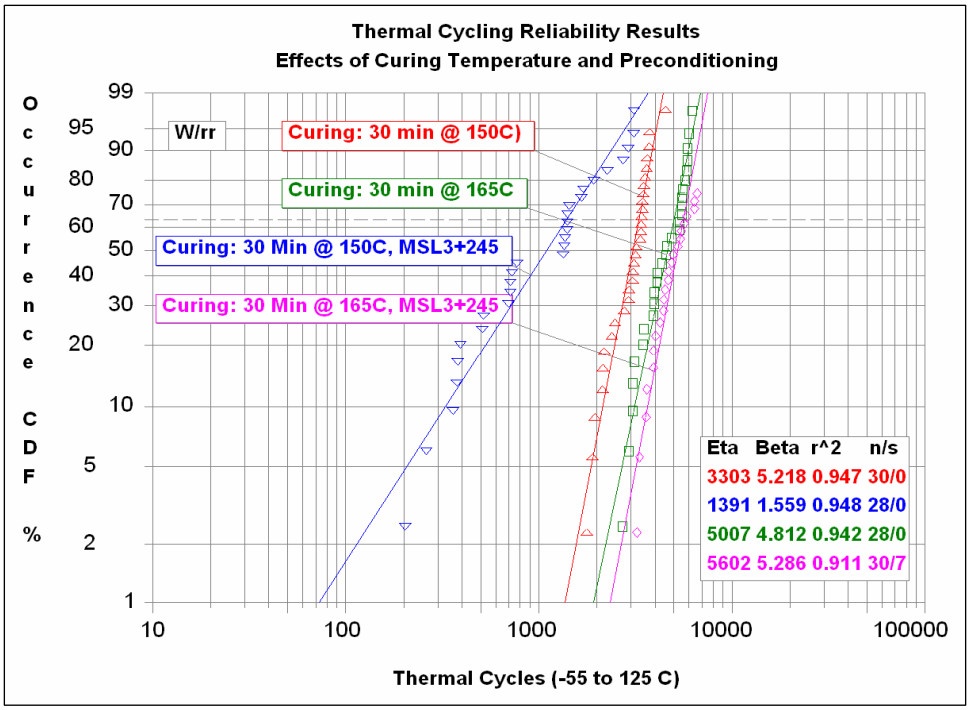

Figure 6.20 - Weibull Failure Plots for Thermal Cycling of the Flip Chip Test Assemblies

Configuration	Weibull Slope, β	Characteristic Life, η (cycles)	$N_{1\%}$ (Cycles)
150 °C, None	5.218	3303	1368
165 °C, None	4.812	5007	1925
150 °C, MSL3+245	1.559	1391	73
165 °C, MSL3+245	5.286	5602	2346

Table 6.2 - Calculated Weibull Parameters

(a)

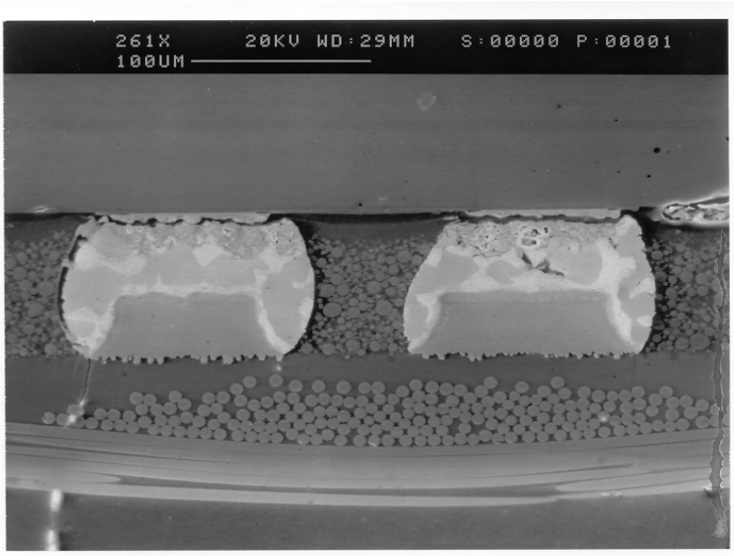

(b)

Figure 6.21 - Cross-Sectioned Solder Joints in the Samples Cured at 150 °C, (a) 7500 Cycles, No Preconditioning; (b) 7300 cycles, MSL3+245 Preconditioning

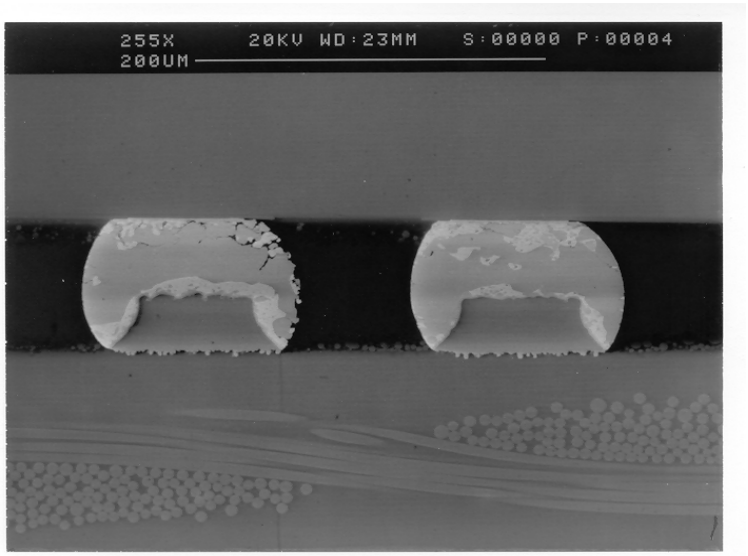

(a)

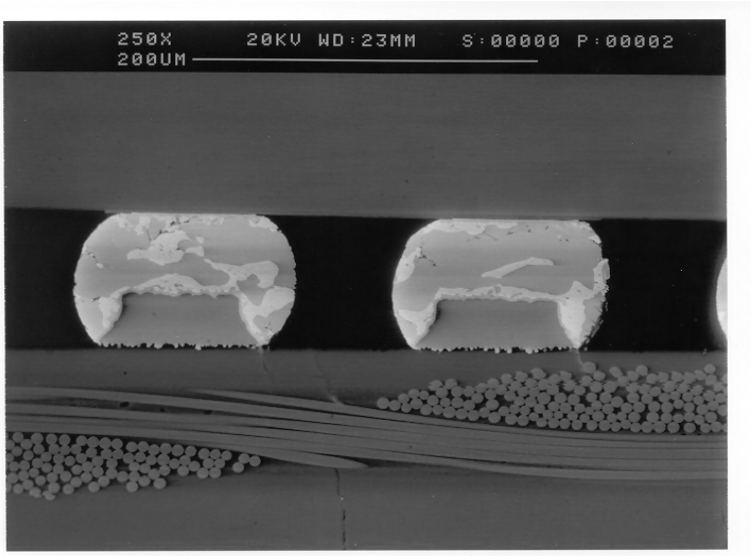

(b)

Figure 6.22 - Cross-Sectioned Solder Joints in the Samples Cured at 165 °C, (a) 6800 Cycles, No Preconditioning; (b) 6500 cycles, MSL3+245 Preconditioning

6.7 Summary and Conclusions

The results presented in this chapter clearly indicate that the advantages that accrued from subjecting the specimens to a higher cure temperature included improved mechanical properties, superior thermal cycling fatigue life, and enhanced resistance to detrimental effects from moisture exposure and solder reflow.

The effects of curing profile and MSL preconditioning on the mechanical and failure properties of underfills, and the reliability performance of underfill flip chip assemblies were investigated. The higher cure temperature of 165 °C led to a significant increase in the values of the effective elastic modulus and also the ultimate tensile strength of the underfill material.

Although MSL3 preconditioning had only a minor effect on the effective elastic modulus, it significantly improved the ultimate tensile strength. The results of the interfacial shear strength tests also demonstrated only slight variations of strength with preconditioning, but the location of the shear failures was shifted significantly to the underfill-substrate interface for the 165 °C cured samples.

Moreover, the MSL3+245 preconditioning exposure was found to generate delaminations in the samples cured at 150 °C, but no delaminations in the samples cured at 165 °C. During thermal cycling, the reliabilities of the 150 °C cured samples were also found to be low relative to the analogous 165 °C samples. This trend was supported by failure analysis, which utilized both cross-sectioning and SEM microscopy. Overall, the use of the higher temperature cure cycle produced better underfill properties and improved the performance of flip chip assembly in all cases.

CHAPTER 7

SUMMARY AND CONCLUSIONS

7.1 Literature Review for the Flip Chip Technology and Underfill Materials

The technology for electronic packaging and underfill materials was reviewed extensively for this dissertation based on the three currently used underfill flow processes. Underfill technology is often considered the major breakthrough in electronics that made possible flip chip technology. A discussion of the composition of underfill material was included, as well as an explanation of the mechanisms governing variations in the mechanical properties due to different underfill materials and thermal aging effects. Although many constitutive models are available to describe the underfill material tensile properties and creep behaviors, there are no reports of models that take into account aging parameters. In order to improve the reliability of packaging applications, models that include these parameters are necessary for use in FEA simulations.

7.2 Unique Specimen Preparation Procedure

In this research, a unique specimen preparation procedure was successfully developed to produce uniform underfill material specimens. Under this procedure, uniaxial tensile specimens with the desired thickness can be made into testing coupons with large length-width ratios. These specimens were made using Teflon coating plates to avoid potential problems due to

sample contamination with mold releasing agents, so the specimens could be made and cured similarly to the methods used industrially for electronic packaging. Therefore, the results obtained from specimens made by this method should be easily transferrable to industrial applications.

7.3 Strain Rate Effects

Tensile test with three strain rates were investigated for underfill materials. Both effective elastic modulus and ultimate tensile strength decreased monotonically with testing temperature and lower displacement strain rate. The material mechanical properties were strongly dependent on temperature, strain rates, and T_g. The material showed the largest elongation at 125 °C, with relatively high bonding strength.

With the newly developed constitutive models, the mechanical properties of underfill material were predicted for all testing conditions by applying variables of strain rate and temperature.

7.4 Isothermal Aging Effects on the Underfill Tensile Properties

Specimens were isothermally aged at four different temperatures for periods from 10 days to 300 days, and then subjected to tensile testing. Aging effects on the tensile properties were also studied for the elastic modulus and ultimate tensile strength. After various durations of isothermal aging, the underfill illustrated softening behaviors at temperatures exceeding 100 °C, although the documented T_g was about 137 °C.

The underfill mechanical properties were enhanced as a function of the aging temperature and aging time. Similarly, aged specimens were subjected to creep tests. Both the effective elastic modulus (initial slope) and ultimate tensile strength (highest stress before failure)

increased monotonically with isothermal aging or aging temperature, regardless of whether the aging temperature was below, at, or above the T_g of the material.

With the isothermal aging, the underfill material mechanical properties became linear with aging time. Both linear and exponential empirical models with four constant parameters were proposed to describe the mechanical property behaviors, and the slope of the linear portion for long term aging could be obtained easily. Furthermore, constitutive models were constructed in order to estimate material mechanical properties as functions of aging temperature, aging time and testing temperature. Reasonable agreement was found between the predictions generated by these models and the experimentally observed data.

7.5 Isothermal Aging Effects on the Underfill Creep Behaviors

Underfill material creep behavior is a kinetics phenomenon associated with the aging process. Isochronous creep curves indicated that the epoxy is a viscoelastic material with medium nonlinearity, and the Boltzmann's linear superposition principle could not be applied for the load range used in this study.

The results of the creep tests revealed that the underfill epoxy behaviors were more sensitive to the test temperature than the loading force, although inelastic strain was exhibited with both increasing load and increasing temperature.

For a given time, the creep strains were much lower for the aged samples compared to non-aged samples. Thermal aging had a significant effect on the secondary creep rate, which decreased with both the aging temperature and the aging time. A reduction of up to 100X in the creep rate was observed, and significant changes occurred during the first 50 days of the isothermal aging. Also, the slope for the long term secondary creep rate increased 3X with test

temperatures from 80 to 150 °C, but degradation increased up to four-fold with stress, down to 25% to 75% of the material's original ultimate tensile strength. More sophisticated constitutive models were proposed in this study to describe the long term secondary creep rate under different aging temperatures and time, along with various testing temperature and stress levels.

7.6 Moisture Effects and Reliability Tests

The effects of moisture and different curing profiles on various material mechanical properties and package reliability were also included in this investigation. The higher of the two curing temperatures tested was found to offer a number of advantages, namely improved mechanical properties, superior thermal cycling fatigue life, and enhanced resistance to detrimental effects from moisture exposure and solder reflow.

With higher curing temperature (165 °C), the effective elastic modulus and ultimate tensile strength of the underfill material also increased significantly. In addition, MSL3 preconditioning had no profound effect on the effective elastic modulus, but significantly improved the ultimate tensile strength.

Interfacial shear strength tests demonstrated slight variations in strength with preconditioning, but an interesting finding was the accompanying shift in the location of the shear failures for samples cured at 165 °C.

The MSL3+245 preconditioning exposures were discovered to result in delaminations in many of the samples cured at 150 °C. However, no delaminations were found in the samples cured at 165 °C. During thermal cycling, specimens cured at 150 °C were found to be less reliable those cured at 165 °C. This trend was supported by failure analysis performed using cross-sectioning and SEM microscopy. Overall, the higher curing cycle led to better underfill

properties and enhanced flip chip assembly performance in all cases.

These mechanical property results, obtained from strain rate tests, tensile tests, and creep tests, could be input into the underfill mechanical properties database, and the constitutive model could be used in FEA simulations to evaluate the reliability of an electronic package at various temperature conditions.

REFERENCES

1. Gilleo, K., Blumel, D., "Great Underfill Race," Proceedings of International Symposium on Microelectronics, pp.701-706, San Diego, CA, 1998.

2. Prasad, R. P., Surface Mount Technology: Principles and Practices, Van Nostrand Reinhold, 1988.

3. Pao, J. H., Pao, Y. H., Solder Joint Reliability of BGA, CSP, Flip Chip and Fine Pitch SMT Assemblies, McGraw-Hill Professional, 1st Edition, 1996.

4. Rao, Y., Shi, S. H., Wong, C. P., "Simple Evaluation Methodology of Young's Modulus-Temperature Relationship for the Underfill Encapsulants," Proceedings of the Electronic Components and Technology Conference, pp. 784-789, San Diego, CA, 1999.

5. Brinson, H. F., Brinson, L.C., Polymer Engineering Science and Viscoelasticity an Introduction, Springer Science and Business Media, LLC, 1st Edition, 2008.

6. Wong, C. P., Luo, S., Zhang, Z., "Flip the Chip", Science, Vol. 290, pp. 2269, 2000.

7. Suryanarayana, D., Wu, T. Y., Varcoe, J. A., "Encapsulants Used in Flip-chip Packages," Proceedings of the 43rd Electronic Components and Technology Conference, IEEE, pp. 193-198, Orlando, FL, 1993.

8. Liu, Y. L., Lead-Free Assembly and Reliability of Chip Scale Packages and 01005 Components, Ph.D. Dissertation, Auburn University, Auburn, AL, 2006.

9. Colella, M., Evaluation, Optimization, and Reliability of No-Flow Underfill Process, Ph.D Dissertation, Georgia Institute of Technology, Atlanta, GA, 2004.

10. Feustal, F., Wiese, S., Meusal, E., "Time Dependent Material Modeling for Finite Element Analyses of Flip Chips," Proceedings of the 50th Electronic Components and Technology Conference, IEEE, pp. 1458-1553, Las Vegas, NV, 2000.

11. Okura, J. H., Dasgupta, A., "Hygro-Mechanical Durability of Underfilled Flip-Chip-on-Board (FCOB) Interconnects," Journal of Electronic Packaging, Transactions of the ASME, Vol. 124(3), pp. 184-187, 2002.

12. Luo, S., Wong, C. P., "Study on Influence of Environment on Adhesion Performance of Underfill for Flip Chip Application," in 2000 Int'l Symposium on Electronic Materials and Packaging, IEEE, pp. 243-250, Boston, MA, 2000.

13. Brinson, L. C., Gates, T. S., "Effects of Physical Aging on Long Term Creep of Polymers and Polymer Matrix Composites," International Journal of Solids and Structures, Vol. 32(6-7), pp. 827-846, 1995.

14. Blumel, D. K., "The Ultimate Flip Chip – Integrated Flux/Underfill," http://tinyurl.com/y8gadmo.

15. Qu, J. M., Wong, C. P., "Effective Elastic Modulus of Underfill Material for Flip-Chip Applications," Transactions on Components and Packaging Technologies, IEEE, Vol. 25(1), pp. 53-55, 2002.

16. Ferguson, T., Qu, J. M., "Moisture Absorption Analysis of Interfacial Fracture Test Specimens Composed of No-Flow Underfill Materials," Journal of Electronic Packaging, Transactions of the ASME, Vol. 125(1), pp. 24-30, 2003.

17. Bae, J. W., Kim, W., "Advanced Underfill for High Thermal Reliability," Journal of Applied Polymer Science, Vol. 83(12), pp. 2617-2624, 2002.

18. Vleeshouwers, S., Jamieson, A. M., Simha, R., "Effect of Physical Aging on Tensile Stress Relaxation and Tensile Creep of Cured EPON 828/Epoxy Adhesives in the Linear Viscoelastic Region," Polymer Engineering and Science, Vol. 29(10), pp. 662-670, 1989.

19. Struik, L. C. E., Physical Aging in Amorphous Polymers and other Materials, Elsevier Scientific Publishing Company, Oxford, NY, 1978.

20. Frigione, M., Naddeo, C., Acierno, D., "Cold-curing Epoxy Resins: Aging and Environmental effects. II - Mechanical Properties," Journal of Polymer Engineering, Vol. 21(4), pp. 349-367, 2001.

21. Struik, L. C. E., "Physical Aging in Plastics and Other Glassy Materials," Polymer Engineering and Science, Vol. 17(3), pp. 165-173, 1977.

22. McManus, A. J., Thomas, K. A., "Characterization of a Faster Resorbing Polymer After Real Time Aging," Journal of Biomedical Materials Research Part B: Applied Biomaterials, Vol. 78B(2), pp. 358-363, 2006.

23. Lee, A., McKenna, G., "Anomalous Aging in Two-phase Systems: Creep and Stress Relaxation Differences in Rubber-Toughened Epoxies," Journal of Polymer Science Part B: Polymer Physics, Vol. 35(8), pp. 1167-1174, 1997.

24. Beckmann, J., McKenna, G., "Physical Aging Kinetics of Syndiotactic Polystyrene as Determined From Creep Behavior," Polymer Engineering & Science, Vol. 37(9), pp. 1459-1468, 1997.

25. Lakes, R. S., Viscoelasticity Solids, CRC Press LLC, 1999.

26. Qian, Z. F., Wang, J., Yang, J., "Visco-Elastic-Plastic Properties and Constitutive Modeling of Underfills," Transactions on Components and Packaging Technologies, IEEE, Vol. 22(2), pp. 152-157, 1999.

27. Rao, Y., Shi, S. H., Wong, C. P., "Improved Methodology for Determining Temperature Dependent Moduli of Underfill Encapsulants," Transactions on Components and Packaging Technologies, IEEE, Vol. 23(3), pp. 434-439, 2000.

28. Shi, X. Q., Wang, Z. P., "Investigation of Effect of Temperature and Strain Rate on Mechanical Properties of Underfill Material by Use of Microtensile Specimens," Polymer Testing, Vol. 21(6), pp. 725-733, 2002.

29. Kuo, C. T., Yip, M. C., Chiang, K. N., "Time and Temperature-Dependent Mechanical Behavior of Underfill Materials in Electronic Packaging Application," Microelectronics Reliability, Vol. 44(4), pp. 627-638, 2004.

30. Islam, M. S., Suhling, J. C., Lall, P., "Measurement of the Temperature Dependent Constitutive Behavior of Underfill Encapsulants," Transactions on Components and Packaging Technology, IEEE, Vol. 28(3), pp. 467-476, 2005.

31. Hertzberg, R. W., Deformation and Fracture Mechanics of Engineering Materials, 4th Edition, John Wiley & Sons Inc, 4th Edition, 1995.

32. Findley, W. N., Lai, J. S., Onaran, K., Creep and Relaxation of Nonlinear Viscoelastic Materials, Dover Publications, INC., New York, 1989

33. Findley, W. N., Khosla, G., "An Equation for Tension Creep of Three Unfilled Thermoplastics," SPE Journal, Vol. 12, pp. 20-25, 1956.

34. Eyring, H., "Viscosity, Plasticity, and Diffusion as Examples of Absolute Reaction Rates," The Journal of Chemical Physics, Vol. 4(4), pp. 283-291, 1936.

35. Garofalo, F., Fundamentals of Creep and Creep-Rupture in Metals, McMillan Company, 1965.

36. Wang, T. H., Lai, Y. S., Wu, J. D., "Effect of Underfill Thermomechanical Properties on Thermal Cycling Fatigue Reliability of Flip-Chip Ball Grid Array," Journal of Electronic Packaging, Vol. 126(4), pp. 560-564, 2004.

37. Zhang, X. R., Shi, X. Q., "On the Moduli of Viscoelastic Materials," Proceedings of 2002 Electronics Packaging Technology Conference, IEEE, pp. 318-332, Singapore, 2002.

38. Islam, M.S., Suhling, J. C., "Measurements and Modeling of the Temperature Dependent Material Behavior of Underfill Encapsulants," Proceedings of the 53rd Electronic Components and Technology Conference, pp. 1636-1643, New Orleans, LA, 2003.

39. Shi, X. Q., Zhou, W., "Effect of Temperature and Strain Rate on Mechanical Properties of 63Sn/37Pb Solder Alloy," Journal of Electronic Packaging, Transactions of the ASME, Vol. 121(3), pp. 179-185, 1999.

40. Qian, Z., Ren, W., Liu, S., "A Damage Coupling Framework of Unified Viscoplasticity for the Fatigue of Solder Alloys," Journal of Electronic Packaging, Vol. 121(3), pp. 162-168, 1999.

41. Ernst, L. J., Yang, D. G., Kiasat, M. S., "Mechanical Modeling and Characterization of the Curing Process of Underfill Materials," Journal of Electronic Packaging, Transactions of the ASME, Vol. 124(2), pp. 97-105, 2002.

42. Pang, J. H. L., Xiong, B. S., Che, F. X., "Modeling Stress Strain Curves for Lead-Free 95.5Sn-3.8Ag-0.7Cu Solder," Proceedings of 2004 Thermal and Mechanical Simulation and Experiments in Microelectronics and Microsystems, EuroSimE, pp. 449-453, Paris, France, 2004.

43. Miyano, Y., Nakada, M., Kasamori, M., and Muki, R., "Effect of Physical Aging on the Creep Deformation of an Epoxy Resin," Mechanics of Time-Dependent Materials, Vol. 4(1), pp. 9-20, 2000.

44. Marand, H., Velikov, V., Prabhu, V., Srinivas, S., Christian, S., "On the Physical Aging of Semicrystalline Polymers Below and Above T_g," Polymeric Materials Science and Engineering, Vol. 76, pp. 259-261, 1997.

45. Dasgupta, A., Pecht, M., "Material Failure Mechanisms and Damage Models," Reliability, IEEE Transactions on, Vol. 40(5), pp. 531-536, 1991.

46. Li, J., Dasgupta, A., "Failure-Mechanism Models for Creep and Creep Rupture," IEEE Transactions on Reliability, Vol. 42(3), pp. 339-353, 1993.

47. Woishnis, W. A., Wright, D. C., Select Plastics to Avoid Product Failure: Advance Master Processes, Vol. 39-40, 1994.

48. Larson, F. R., Miller, J., "A Time-Temperature Relationship for Rupture and Creep-Stress," Transactions ASME, Vol. 74, pp. 765-771, 1952.

49. LeMay, I., "Developments in Parametric Methods for Handling Creep and Creep-Rupture Data," Journal of Engineering Materials and Technology, Vol. 101, pp. 326-330, 1979.

50. Liu, Y. L., Tian, G. Y., Johnson, R. W., "Lead-Free Chip Scale Packages: Assembly and Drop Test Reliability," Transactions on Electronics Packaging Manufacturing, IEEE, Vol. 29(1), pp. 1-9, 2006.

51. Yang, J. L., Zhang, Z., "On the Characterization of Tensile Creeps Resistance of Polyamide 66 Nanocomposites. Part II: Modeling and Prediction of Long-Term Performance," Polymer, Vol. 47(19), pp. 6745-6758, 2006.

52. Soles, C., Yee, A., "A Discussion of the Molecular Mechanisms of Moisture Transport in Epoxy Resins," Polymer. Science 38 (Part B: Polymer Physics), pp. 792-802, 2000.

53. Soles, C., Chang, T., Gidley, D., Yee, A., "Contributions of the Nanovoid Structure to the Kinetics of Moisture Transport in Epoxy Resins," Polymer Science 38 (Part B: Polymer Physics), pp. 776-791, 2000.

54. Luo, S., Wong C. P., "Moisture Absorption in Uncured Underfill Materials," Transactions on Components and Packaging Technologies, IEEE, Vol. 27(2), pp. 345-351, 2004.

55. Ferguson, T. P., Qu, J, M., "Moisture and Temperature Effects on the Reliability of Interfacial Adhesion of a Polymer/metal Interface," Electronic Component and Technology Conference, IEEE, pp. 1752-1758, 2004.

56. Ferguson, T. P., Qu, J., "Elastic Modulus Variation Due to Moisture Absorption and Permanent Changes upon Redrying in an Epoxy Based Underfill," Transactions on Components and Packaging Technologies, IEEE, Vol. 29(1), pp. 105-111, 2006.

57. Luo, S., Wong, C. P., "Influence of Temperature and Humidity on Adhesion of Underfills for Flip Chip Packaging," Transactions on Components and Packaging Technologies, IEEE, Vol. 28(1), pp. 88-94, 2005.

58. Tian, G. Y., Lin, C., Suhling, J. C., Johnson, R. W., "The Effects of Cure Profile Upon the Properties and Thermo-Mechanical Reliability of Flip Chip Underfills," Proceedings of 2006 SMTA International, IEEE, pp. 515-523, Chicago, IL, 2006.

59. Zhang, Y. L., Shi, X. Q., Zhou, W., "Effect of Hygrothermal Aging on Interfacial Reliability of Flip Chip on Board (FCOB) Assembly," Proceedings of the 6th Electronics Packaging Technology Conference, IEEE, pp. 404-409, Shenzhen, China, 2004.

60. Chaware, R., Vichare, N., Borgesen, P., Blass, D., Srihari, K., "Accelerated Testing of Flip Chip Underfills and the Effect of Moisture and Temperature on the Aging of Underfills," Proceedings of 2004 Surface Mount Technology Association International, pp. 374-380, Oahu, HI, 2004.

61. Wong, E. H., R. Rajoo, R., Lim, T. B., "Swelling and Time-Dependent Subcritical Debonding of Underfill during Temperature-Humidity Aging of Flip Chip Packages," Transactions on Components and Packaging Technologies, IEEE, Vol. 28(4), pp. 862-868, 2005.

62. Dimke, M., "Adhesion of Flip-chip Underfills to Various Die Passivations before and after Accelerated Environmental Exposure," Proceedings of SMTA Pan Pacific Conference, pp. 71-75, Kauai, HI, 2001.

APPENDIX

Additional Creep Data for Specimens Aged at 80, 125, and 150 °C

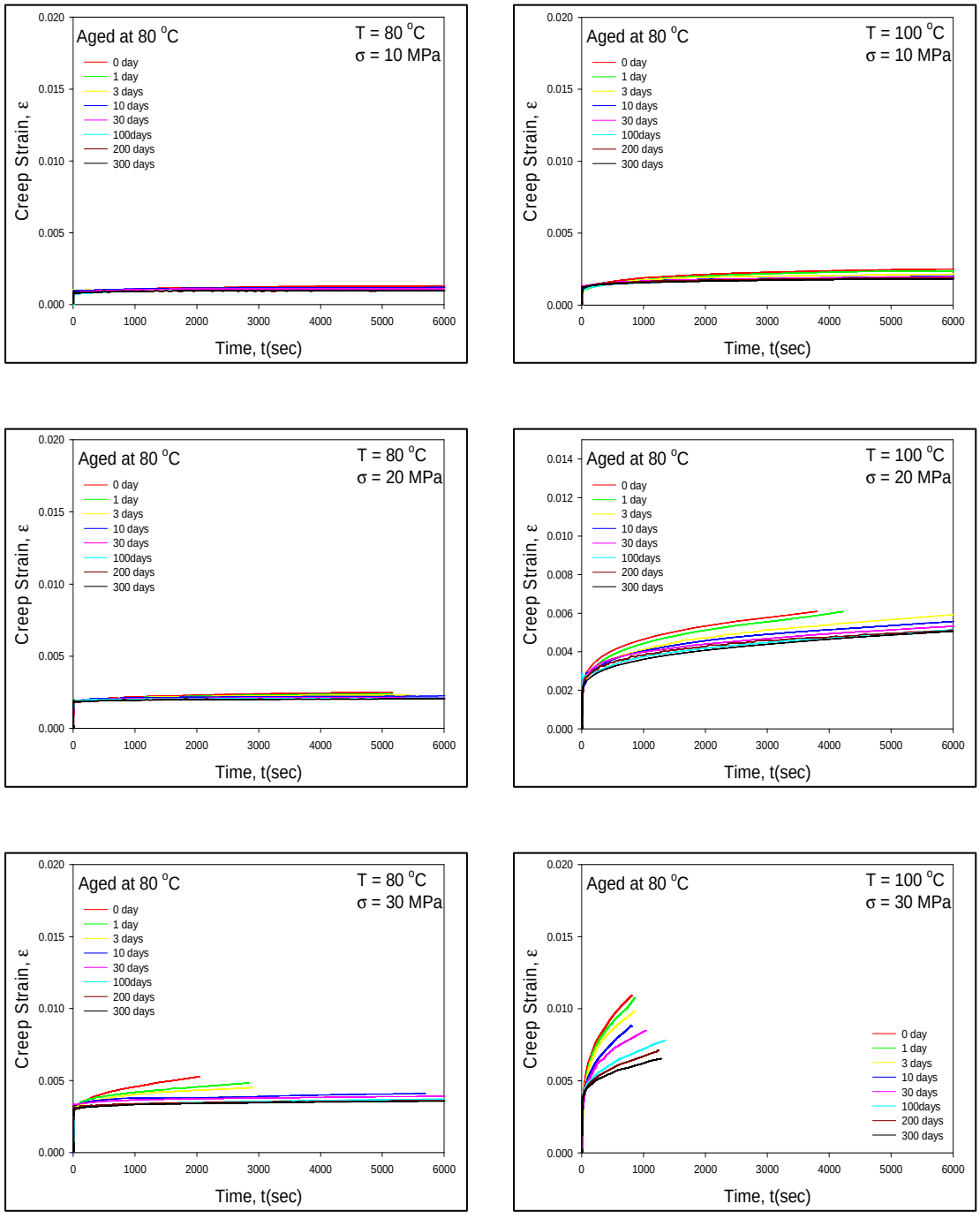

Figure A-1 - Creep Curves for Various Aging Times (Samples Aged at 80 °C, Tested at 80, 100 °C)

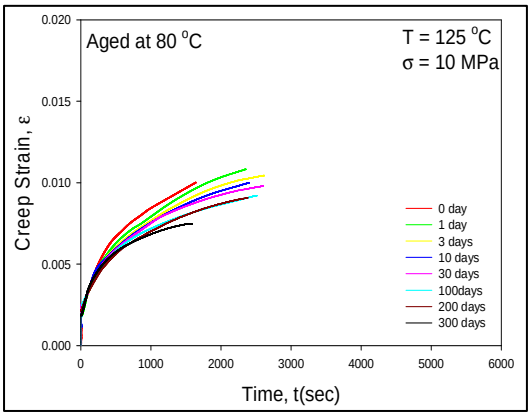

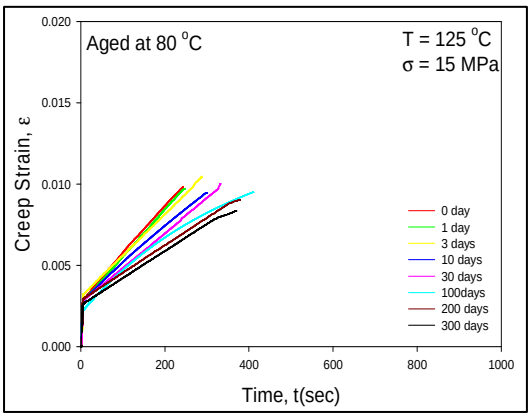

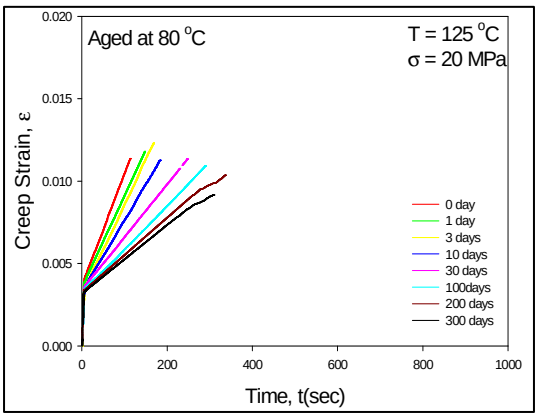

Figure A-2 - Creep Curves for Various Aging Times (Samples Aged at 80 °C, Tested at 125 °C)

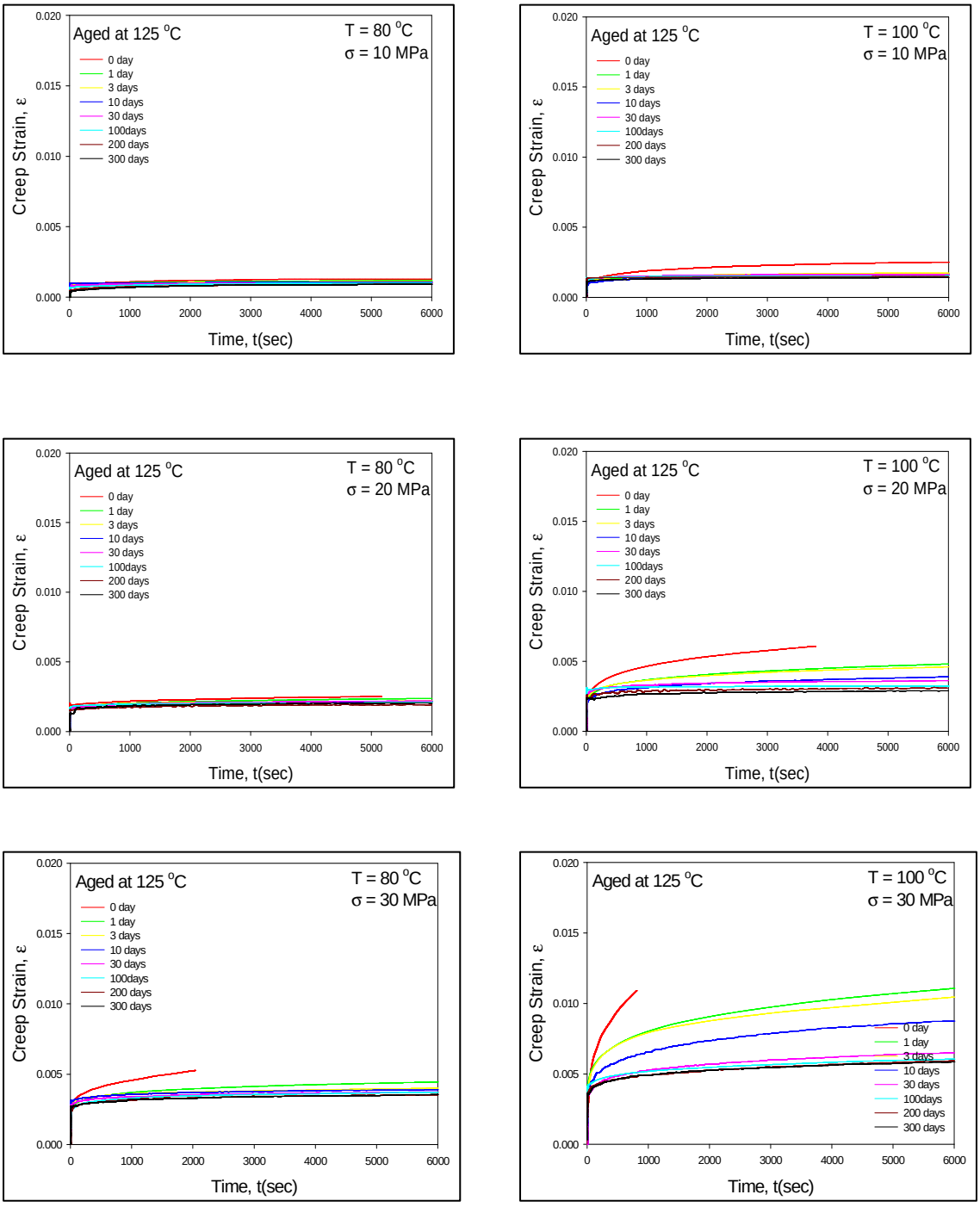

Figure A-3 - Creep Curves for Various Aging Times (Samples Aged at 125 °C, Tested at 80, 100 °C)

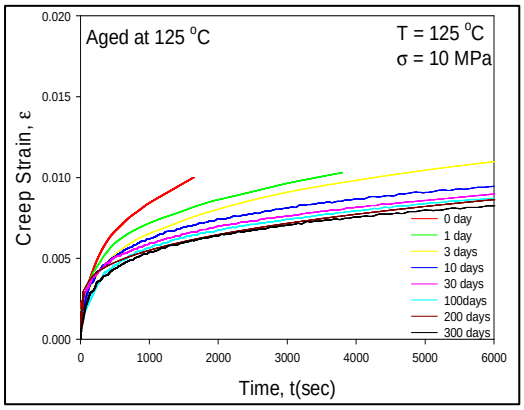

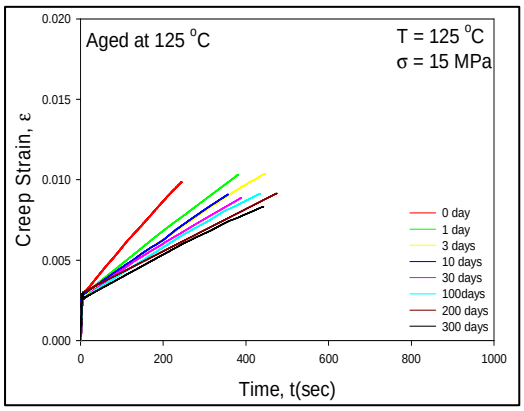

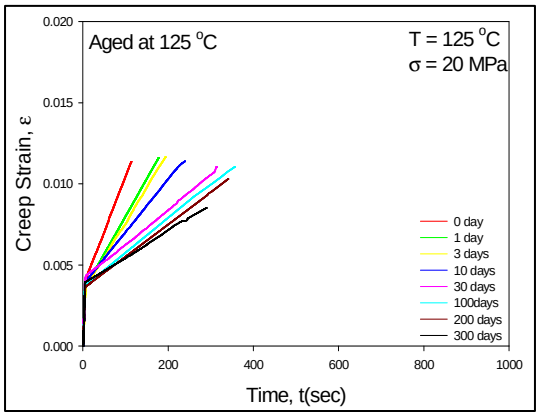

Figure A-4 - Creep Curves for Various Aging Times (Samples Aged at 125 °C, Tested at 125 °C)

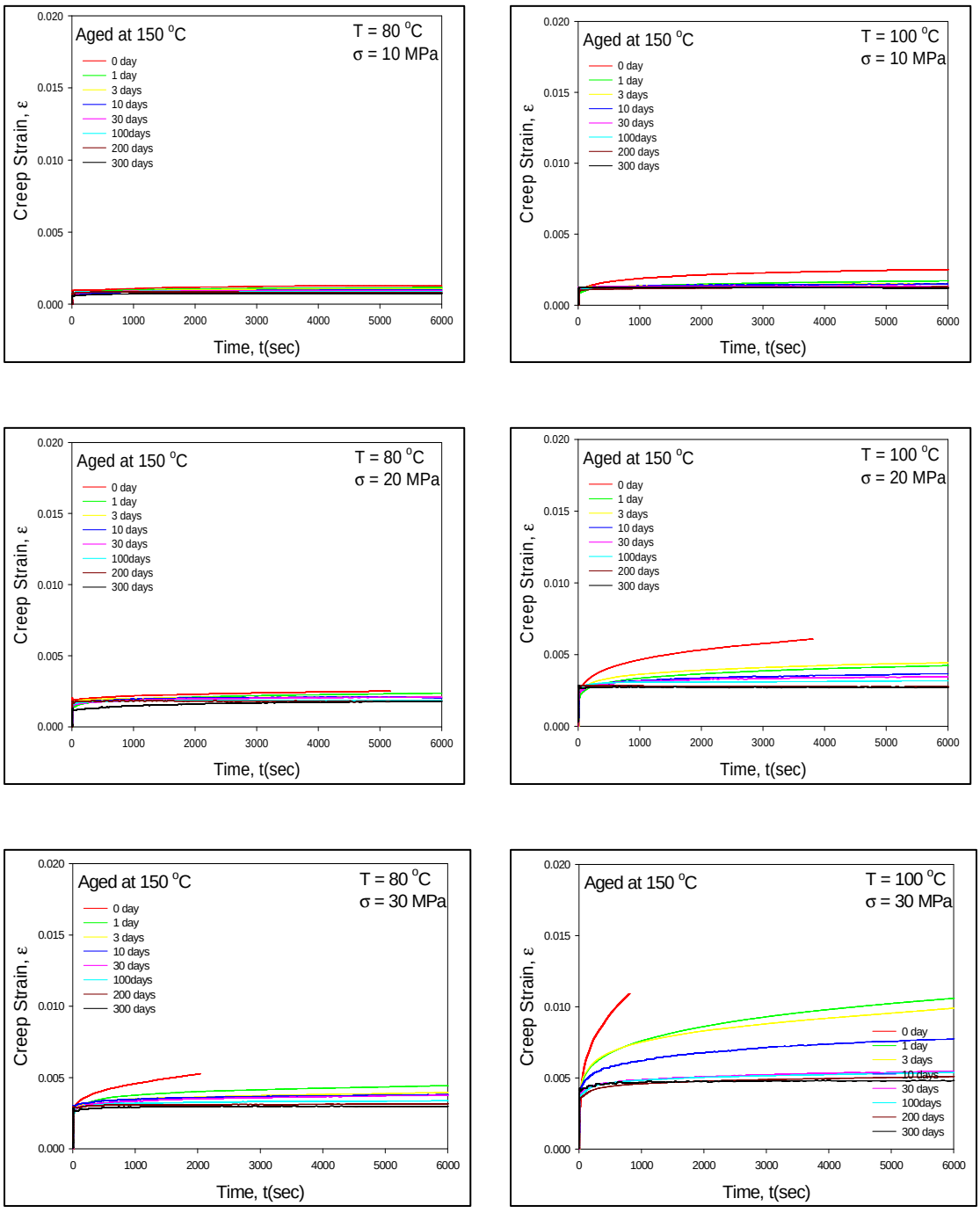

Figure A-5 - Creep Curves for Various Aging Times (Samples Aged at 150 °C, Tested at 80, 100 °C)

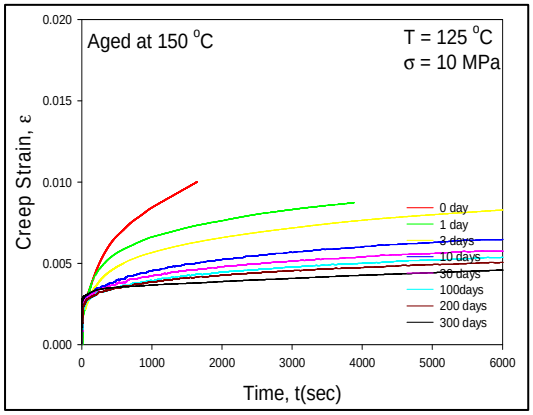

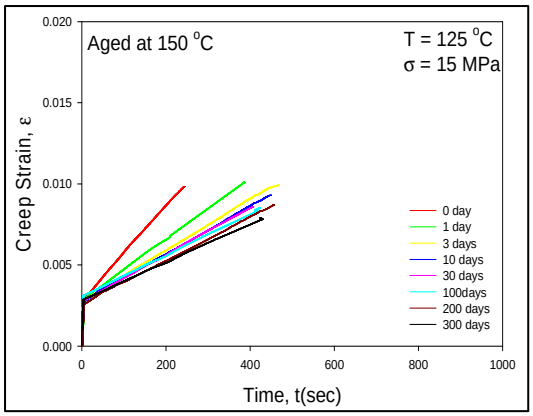

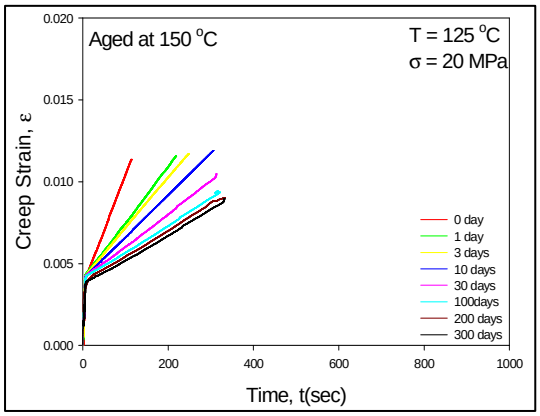

Figure A-6 - Creep Curves for Various Aging Times (Samples Aged at 150 °C, Tested at 150 °C)